AD_____

Award Number: DAMD17-94-J-4292

TITLE: Improved Mammographic Technique for Breast Cancer Diagnosis

PRINCIPAL INVESTIGATOR: Heang-Ping Chan, Ph.D.

CONTRACTING ORGANIZATION: University of Michigan
Ann Arbor, Michigan 48103-1274

REPORT DATE: August 1999

TYPE OF REPORT: Final

PREPARED FOR: U.S. Army Medical Research and Materiel Command
Fort Detrick, Maryland 21702-5012

DISTRIBUTION STATEMENT: Approved for public release;

The views, opinions and/or findings contained in this report are those of the author(s) and should not be construed as an official Department of the Army position, policy or decision unless so designated by other documentation.

REPORT DOCUMENTATION PAGE

Form Approved
OMB No. 074-0188

1. AGENCY USE ONLY (Leave blank)	2. REPORT DATE	3. REPORT TYPE AND DATES COVERED
	August 1999	Final (11 Jul 94 - 10 Jul 99)

4. TITLE AND SUBTITLE
Improved Mammographic Technique for Breast Cancer Diagnosis

5. FUNDING NUMBERS
DAMD17-94-J-4292

6. AUTHOR(S)
Heang-Ping Chan, Ph.D.

7. PERFORMING ORGANIZATION NAME(S) AND ADDRESS(ES)
University of Michigan
Ann Arbor, Michigan 48109

E-MAIL:
chanhp@umich.edu

8. PERFORMING ORGANIZATION REPORT NUMBER

9. SPONSORING / MONITORING AGENCY NAME(S) AND ADDRESS(ES)
U.S. Army Medical Research and Materiel Command
Fort Detrick, Maryland 21702-5012

10. SPONSORING / MONITORING AGENCY REPORT NUMBER

11. SUPPLEMENTARY NOTES

12a. DISTRIBUTION / AVAILABILITY STATEMENT
Approved for public release; Distribution Unlimited

12b. DISTRIBUTION CODE

13. ABSTRACT ***(Maximum 200 Words)***

During the entire project period, we have completed the following tasks: (1) Develop computerized breast border detection and classification scheme. (2) Develop and evaluate exposure equalization filters. (3) Monte Carlo modeling of mammographic imaging systems and optimization of imaging techniques. (4) Design and build breast-tissue-equivalent phantoms for x-ray and ultrasound imaging. (5) Evaluate effects of equalization on image quality. (6) Develop a novel combined x-ray equalization and ultrasound imaging system for improved evaluation of dense breasts and mammographic lesions. (7) Design and build a compressible tank and a special compression paddle for combined imaging. (8) Evaluate tissue-equivalent fluids for x-ray equalization and ultrasound coupling. (9) Perform phantom study to evaluate the feasibility of combined imaging. (10) Develop breast density segmentation program for automated localization of dense tissue regions on digitized mammograms. (11) Design and build a prototype motorized ultrasound scanning device for the combined imaging system. These studies are consistent with the goals of our proposed project. Our new approach of using a compressible tank containing tissue-equivalent fluid for x-ray equalization in a prone mammography system provides truly patient-specific equalization for breasts of any size and shape, and for any mammographic view. Our studies indicate that x-ray equalization can improve visibility of breast lesions on mammograms. We also demonstrated that the feasibility of developing a combined x-ray and ultrasound imaging system for improved breast imaging. The capability of allowing ultrasound scanning in the same geometry as mammography has the promise to improve breast cancer detection and diagnosis in dense breasts.

14. SUBJECT TERMS
Breast cancer, Mammography, exposure equalization, dynamic range compression, breast cancer detection

15. NUMBER OF PAGES
75

16. PRICE CODE

17. SECURITY CLASSIFICATION OF REPORT	18. SECURITY CLASSIFICATION OF THIS PAGE	19. SECURITY CLASSIFICATION OF ABSTRACT	20. LIMITATION OF ABSTRACT
Unclassified	Unclassified	Unclassified	Unlimited

NSN 7540-01-280-5500

Standard Form 298 (Rev. 2-89)
Prescribed by ANSI Std. Z39-18
298-102

FOREWORD

Opinions, interpretations, conclusions and recommendations are those of the author and are not necessarily endorsed by the U.S. Army.

___ Where copyrighted material is quoted, permission has been obtained to use such material.

X_ Where material from documents designated for limited distribution is quoted, permission has been obtained to use the material.

X_ Citations of commercial organizations and trade names in this report do not constitute an official Department of Army endorsement or approval of the products or services of these organizations.

N/A In conducting research using animals, the investigator(s) adhered to the "Guide for the Care and Use of Laboratory Animals," prepared by the Committee on Care and use of Laboratory Animals of the Institute of Laboratory Resources, national Research Council (NIH Publication No. 86-23, Revised 1985).

X For the protection of human subjects, the investigator(s) adhered to policies of applicable Federal Law 45 CFR 46.

N/A In conducting research utilizing recombinant DNA technology, the investigator(s) adhered to current guidelines promulgated by the National Institutes of Health.

N/A In the conduct of research utilizing recombinant DNA, the investigator(s) adhered to the NIH Guidelines for Research Involving Recombinant DNA Molecules.

N/A In the conduct of research involving hazardous organisms, the investigator(s) adhered to the CDC-NIH Guide for Biosafety in Microbiological and Biomedical Laboratories.

Chan Heang Ping 9/9/99.

PI - Signature Date

(4) Table of Contents

(1) Front Cover 1
(2) Standard Form (SF) 298, REPORT DOCUMENTATION PAGE 2
(3) FOREWARD 3
(4) Table of Contents 4
(5) Introduction 5
(6) Body 6
  (A) Automated classification of breast shape from digitized mammograms 6
  (B) Filter design and simulation study of effect of x-ray equalization 7
  (C) Monte Carlo simulation of mammographic system 8
  (D) New approach to x-ray equalization 9
  (E) Development of a prototype compressible tank for equalization with a prone mammography system 10
  (F) New approach of w-ray equalization in combination with ultrasound imaging 10
  (G) Investigation of x-ray and ultrasound tissue-equivalent fluids 11
  (H) Investigation of plastics for the compression paddle 15
  (I) Combined x-ray/ultrasound imaging-Preliminary study 16
  (J) Automated segmentation of dense tissue region on mammograms 17
  (K) Ultrasound scanning device 18
  (L) Illustrations 19
(7) Key Research Accomplishments 26
(8) Reportable Outcomes 27
(9) Conclusion 28
(10) References 29
(11) Appendix 31
(12) Personnel supported by the research grant 32

(5) Introduction

Breast cancer is one of the leading causes of death among women. There is considerable evidence that early diagnosis and treatment significantly improve the chance of survival for patients with breast cancer [Baker, 1982]. At present, x-ray mammography is the only diagnostic procedure with a proven capability for detecting early-stage, clinically occult breast cancers [Baker, 1982]. Although mammography has a high sensitivity for detection of breast cancer when compared to other diagnostic procedures, studies indicate that radiologists identify only 70 to 90% of the lesions present [Haug, 1987; Baines, 1986]. The miss rate is particularly high in dense breasts [D'Agincourt, 1993; Wallis, 1991]

One of the difficulties in interpretation of mammograms by radiologists is caused by the limited latitude and contrast sensitivity of mammographic screen/film systems. Mammographic abnormalities related to early breast cancers include clustered microcalcifications, spiculated and irregular masses, areas of parenchymal distortion, and skin thickening [Sickles, 1986]. These abnormalities are often subtle and low contrast. Therefore, low energy radiation and high contrast screen/film systems are recommended for mammographic imaging in order to increase the contrast between the lesion and the background tissue. Despite the use of vigorous compression during examinations, the low-energy x-ray beam results in a wide dynamic range (the ratio of the maximum to the minimum x-ray exposure at the detector) for the radiation penetrating the breast. This range can be greater than 100. On the other hand, high-contrast film provides a narrow latitude which is about 10 for a typical mammographic system [Bunch, 1987] As a result, thick and glandular regions of the breast are often imaged at the toe of the sigmoid-shaped sensitometric curve of the screen/film system; whereas thin peripheral regions are imaged at the shoulder. The contrast and signal-to-noise ratio (SNR) of mammographic features are greatly reduced in these regions due to decreased film gradient and increased noise. The contrast sensitivity of the human visual system also drops rapidly as the film density increases [Baxter, 1982; Snyder, 1985]. Kopans [D'Agincourt, 1993] found that 70% of breast cancers in women with dense breasts are in the periphery of the mammary parenchyma adjacent to the subcutaneous fat or retromammary fat. The poor image quality in the peripheral region thus imposes a serious limitation on the sensitivity of cancer detection in breasts with dense fibroglandular tissue.

We proposed a practical and cost-effective exposure equalization method for reducing the dynamic range of the x-ray image. The shapes of compressed breasts of the patient population will be analyzed and classified into a finite number of groups. A shaped filter for attenuating x-rays in the peripheral region of the breasts will be fabricated for each group. For a given patient, the breast shape during compression will be classified into one of these groups and the filter for the selected group will be used for this patient. With this technique, the dynamic range of the x-ray intensities incident on the recording system will be reduced and the entire image can be recorded in the high contrast region of the film. The improved image quality can be achieved without additional radiation dose to the patient. Furthermore, a very high-contrast mammographic technique may be developed in combination with exposure equalization to further improve the signal-to-noise ratio (SNR) of the subtle lesions. We expect that the optimized technique will significantly improve the detectability of cancers in mixed and dense breasts and increase the efficacy of mammography as a screening and diagnostic tool for breast cancers.

In the course of the research, we designed a new approach to the implementation of an x-ray equalization filter for mammography, as we discussed in the previous annual reports. In this new approach, the patient breast will be immersed in a compressible tank containing a tissue-equivalent fluid that is compressed together with the breast during x-ray exposure. The fluid will fill any space between the breast, the cassette holder and the compression paddle. Therefore, this approach has the advantages that the filter is truly patient specific and tissue equivalent for any mammographic view.

In the current year, we have investigated another new idea that may further improve breast cancer diagnosis. In this new approach, x-ray and ultrasound imaging are combined in one exam so that the patient breast is imaged in exactly the same geometry by the two modalities. This allows a suspicious mass seen on an x-ray mammogram be examined immediately by ultrasound for the differentiation of solid masses from cysts. Moreover, an underpenetrated dense fibroglandular area on the mammogram can be further examined by ultrasound immediately to determine if there are any hidden masses. Our x-ray equalization system facilitates combined x-ray and ultrasound imaging because the x-ray equalizing tissue-equivalent fluid can also serve as the coupling medium for ultrasound imaging. We have further investigated possible fluids that can be tissue-equivalent for both x-ray and ultrasound and compression paddle materials that allow x-ray and ultrasound transmission. Some promising fluids and compression paddle material have been identified. Phantom experiments have been performed to evaluate the x-ray and ultrasound images with the compressible tank under the prone x-ray table. The studies indicate the feasibility of a combined x-ray and ultrasound system and the potential to improve breast imaging for cancer detection. Detailed descriptions of the studies are included in the Body of this report.

(6) Body

In this final report, we summarize the studies performed in the entire funding period (7/11/94-7/10/99) and the significant results obtained under the support of this grant. Some of the details have been reported in the previous years.

(A) Automated Classification of Breast Shape from Digitized Mammogram

In our original approach to the development of an x-ray equalization system, we proposed to design a set of near-patient-specific filters and automatically select an appropriate filter for a given breast. We therefore developed a computerized method to classify compressed breast shapes into a finite number of classes. The shape of a compressed breast is determined from the breast border detected in a digitized mammogram. Breast shape classification and filter design are based on these detected breast borders.

(a) Automated edge detection

We have reported previously on the fully automated model-guided breast border detection program developed by A. R. Morton as his Master Thesis project [Morton, 1995]. Briefly, the unexposed area and labels are first eliminated from a digitized mammogram; the breast border is then searched within the area of the film exposed by x-rays. Our algorithm uses

a two-pass approach. In the first pass, a simple edge detection routine using the first and second derivatives locates the approximate edge coordinates for each line. These coordinates are used as a tracking path for the accurate edge detection routine. In the second pass, the program uses local statistics to determine an adaptive threshold criterion and find the exact edge location within a range of pixels centered on the approximate edge. The search starts from about the nipple of the breast image and tracks in both directions. For subsequent edge points, the edge tracking routine uses previously found edge points to adjust the search direction and the approximate location of the breast border.

This model-guided search method reduces the likelihood that the edge tracking routine will be misled by noisy background fluctuations. The edge tracking routine can accurately detect the breast borders in over 90% of the 1000 images digitized for the breast shape analysis. A comparison study of the detected breast borders with a manually traced 'true' breast border was performed to quantify the accuracy of the edge detection algorithm. The breast border tracking method and results were presented [Morton, 1996] and discussed in our publication [Goodsitt, 1998].

(b) Breast Shape Classification

We have reported in detail the breast shape classification study in the previous years. Briefly, we digitized approximately 500 mammograms in craniocaudal (CC) view and another 500 mammograms in medialateral view (MLO) view. The breast borders were tracked by the automated program and fitted with a third-order polynomial in the form $y = ax^2 + bx^3$. The fitted parameters a and b were then used as features and classified into a small number of classes by a clustering algorithm. We developed two statistics, the overall mean root-mean-square (RMS) distance error and a figure-of-merit that was inversely proportional to the mean-square error and the number of clusters, to evaluate the goodness of classification and compared the relative merits of classification into different number of classes. Based on these indices of goodness, we optimized the breast shape classification scheme. It was found that breast shapes in each view could be classified into 3 to 4 classes. This finding supports the hypothesis of our proposed approach, namely, only a small number of external filters are needed for an external equalization system to provide near-patient-specific x-ray equalization. The breast shape classification methods and the results of the study have been published [Goodsitt, 1998].

(B) Filter Design and Simulation Study of Effect of X-Ray Equalization

(a) Filter Design

We have developed a computerized method to generate a three-dimensional (3D) model for each equalization filter. The 3D model provides the 2D projected shape and the appropriate thickness profile of an average filter for a given breast shape class. The 3D model will be useful for controlling a computerized milling machine to build the actual filters. The details of the filter design method were described in our previous report. In brief, after breast shape classification, we designed a filter for each breast shape class. We first analyzed the optical density profiles along the breast border for each breast image in the class. The relative exposure profiles were derived from the optical density profiles by use of the sensitometric curve of the screen-film system. An average exposure profile was then used for calculation of the thickness profile of the

filter for a chosen material. Materials of different x-ray attenuation properties were studied and some prototype filters were built. The effects of the filters on equalization of the breast image were evaluated with experiments using breast phantoms. It was found that the filters can provide effective equalization and improvement in the visibility of mammographic features. However, some misalignment artifacts were also observed on the phantom images. The filter design and the results of the phantom studies were discussed in detail in our publication [Keshavmurthy, 1999]

(b) Simulation study

In order to evaluate the effects of equalization and filter alignment on mammographic images, we designed a computer simulation study using a ray-tracing method. A mammogram without equalization was used as the input. The mammogram was digitized and its optical density was determined at each pixel by using the calibration curve of the digitizer. The optical density was converted to relative x-ray exposure via the sensitometric curve of the screen-film system. When a filter was inserted between the breast and the x-ray focal spot, the change in the exposure at a given pixel location was determined by the x-ray attenuation of the filter. The filtered exposure was converted back to optical density, resulting in a filtered mammogram. We designed a figure-of-merit to evaluate the potential artifacts at the breast periphery caused by filter misalignment. An observer performance study was also conducted in which an experienced radiologist rated the quality of the equalized mammograms. It was found that the majority of the mammograms were improved by equalization without artifacts. Less than 6% of the equalized CC view images and less than 19% of the equalized MLO images contain some noticeable artifacts. The simulation studies therefore indicate that, with automated breast shape classification, filter selection, and alignment, it is feasible to implement the external x-ray beam equalization technique in a mammography system, which will only require minimal additional operator intervention. A filter designed for a given breast shape class can match fairly well to patient breasts in that class. Some mismatch artifacts can be observed locally, but they do not disturb the visibility of the structures in the breast image. For a given breast shape class, if additional filters of different thicknesses are built, e.g., three thicknesses for thick, medium, and thin breasts, respectively, matching of OD at the periphery will be improved. The findings of this simulation study was recently published [Keshavmurthy, 1999].

(C) Monte Carlo simulation of mammographic system

(a) Detector evaluation

We have discussed the Monte Carlo simulation studies in the previous reports. Briefly, we used Monte Carlo methods to evaluate the mean glandular dose and the detector response in a mammographic imaging system. The MCNP Monte Carlo code from Los Alamos National laboratory was used for this purpose. The image contrast and noise properties of the detectors were evaluated for the task of imaging a 200 micron microcalcification in a 5-cm-thick breast of average 50% adipose/50% glandular tissue composition. The entire imaging process was simulated including the use of a mammography imaging geometry, measured x-ray spectra from a Mo target, Mo filter x-ray tube [Jennings] at tube voltages ranging from 24 kVp to 38 kVp, and a moving grid with a 5:1 grid ratio and grid frequency of 31 lines/cm. Primary contrast was computed analytically and reabsorption of K-characteristic x-rays was included in the detector. Scatter fraction both with and without the grid, the quantum noise, and mean glandular dose were predicted with the Monte Carlo simulation. Both direct detectors (e.g. a-Se, CdZnTe, and

PbI_2) and indirect detectors (screens such as CsI and Gd_2O_2S backed by flat panel active matrix detectors) were included in the study.

Test cases were also simulated to verify the accuracy of our model. We found that the mean glandular doses computed with our model were within 1 to 4% of those computed by Wu et al. [Wu, 1991]. The scatter fractions were within 10% of those we measured experimentally and those measured by Rezentes et al [Rezentes, 1998]. Finally, the primary contrasts were within 4% of those computed by Dance et al [Dance, 1992].

A figure of merit (FoM), defined as the ratio of the square of the contrast-to-noise-ratio (CNR) divided by the mean glandular dose, was derived to compare the detectors. This FoM was evaluated as a function of tube voltage for the various detectors under the conditions both with and without the grid. It was found that the maximum FoM occurs between 28 and 30 kVp, regardless of the detector or use of the grid. For the particular detector thicknesses studied, and only considering quantum noise, the ranking of the detectors from best to worst according to their FoM's is: Gd_2O_2S, PbI_2, a-Se, CdZnTe, and CsI. It is expected that this ranking will depend on the thickness of the detector material. The Monte Carlo simulation studies will provide guidance for spectrum selection when imaging breasts of various thicknesses and compositions with the different detectors. These results were presented at the 1997 RSNA meeting [Keshavmurthy, 1997].

(c) Mean glandular dose for magnification mammography

One of the important indicators of the dose efficiency of a mammographic imaging system is the mean glandular dose (MGD). With our Monte Carlo modeling of a mammographic system, we can calculate the MGD per unit incident exposure of a given technique. Detailed tables of MGD per unit incident exposure for contact techniques under different imaging conditions are available in the literature [Wu, 1991]. To provide similar data for magnification mammography, we performed Monte Carlo simulation for a range of x-ray tube voltages, breast thicknesses, and breast compositions. The dose for the magnification technique was compared to that for the contact technique. The tabulated MGD per incident exposure data will be useful for dose estimation and for the optimization of imaging techniques in magnification geometry. The method and results of this Monte Carlo simulation study have been published [Liu, 1995].

(D) New Approach to X-Ray Equalization

As detailed in our previous reports, while we were working on our original external filter equalization method, we conceived of a new x-ray equalization technique. This new technique offered the advantages of being more patient specific and being immune to the possible filter misalignment image artifacts that we noted in our external filter simulation studies described above. Our new approach was to image the breast while it is immersed in an x-ray exposure equalizing liquid in a compressible tank using a prone mammography x-ray system. The liquid will be compressed with the breast and will uniformly fill all gaps. It will therefore "fit" all breasts regardless of their shapes and sizes, and regardless of the mammographic view. With the approval of the USAMRMC, we purchased a used Fischer biopsy table/prone mammography system so that we could develop and test this new approach to x-ray equalization.

(E) Development of a Prototype Compressible Tank for Equalization with a Prone Mammography System

As reported last year, we have designed and built a prototype compressible tank with the assistance from a group of mechanical engineering student at the University of Michigan. The tank was fit on the x-ray supporting arm of the Fischer prone mammography system and can be rotated to different angles with the x-ray tube. Therefore, equalization can be provided at any mammographic views. The detailed design and a picture of the compressible tank were included in last year's report.

We made some minor modifications to the tank this year. The attachment between the compression paddle and the x-ray/ultrasound transmission window was rebuilt to improve the seal. The arm that attaches the compression paddle to the compression mechanism of the prone table was also rebuilt to improve the travel distance of the paddle. The new arm allows compression for very thin to very thick breast in the tank. The seal between the compression paddle and the tank was also improved to reduce the chance of leakage. With the improvement of the tank, we were able to perform a preliminary study to test the combined x-ray equalization and ultrasound scanning process for a breast phantom using the tissue-equivalent fluid described below.

(F) New Approach of X-Ray Equalization in Combination with Ultrasound Imaging

During the development of the new device for implementing our liquid bolus method for equalizing the x-ray exposure in mammography, we noted that such a device might be modified to also permit ultrasound imaging of the breast in the mammographic imaging geometry. This device could help resolve a fairly problem of not knowing for certain whether a given breast lesion found with ultrasound corresponds with a mammographically identified abnormality [Conway, 1991]. This uncertainty results from the fact that the ultrasound examinations are conventionally performed free-hand, under different patient positioning and imaging geometry from those in mammography. In discussing possible applications of a combined x-ray and ultrasound breast imager, our radiologists informed us that - such a device would be extremely useful as a problem-solving tool for patients with fibrocystic disease whose mammograms show multiple masses. These mammograms are commonly difficult to interpret. Even though free-hand ultrasound is used in these patients for additional evaluation, the differences in positioning between the two modalities often result in uncertainty concerning 1) the correlations between the masses observed with the two modalities and 2) whether each mammographic mass was identified with free-hand ultrasound. The additional ultrasound information obtained in the mammography geometry would permit the radiologist to more accurately assess the findings in the mammogram. The radiologists also suggested that the device could be very useful as a screening tool for earlier detection of cancer in subjects who are at high risk for breast cancer and have dense breasts. Also, it could be beneficial for evaluating patients with non-palpable, developing densities, a problem often encountered in estrogen therapy patients.

Based on this information, we decided to modify our device to permit combined x-ray and ultrasound imaging of the breast. As a long-term goal, the combined imaging procedure will be fully automated. An x-ray mammogram in a given view will be taken and recorded with a digital detector. A computerized segmentation program will instantly analyze the mammogram

and localize suspicious masses or dense tissue regions. A computer-controlled x-y translator will then automatically move the ultrasound scanner head to the suspicious lesion or the dense region. Ultrasound scanning of the region will then be performed in the same geometry as the mammogram and the lesions correlated with the mammographic findings.

Within the current project period, we conducted preliminary studies to evaluate the feasibility of this approach. The procedure was performed manually using a breast phantom and the modified prototype device.

The principal modifications involved developing a compression paddle that could be used for both x-ray and ultrasound imaging, and developing a breast immersion fluid that would both produce the desired x-ray equalization and act as an ultrasound transmission medium. A primary goal of our design was that it should not result in degradation of either the x-ray or the ultrasound images. Our literature searches showed that previously devised methods such as the upright imaging system of Richter et al [Richter, 1997] suffered from this problem.

(G) Investigation of X-Ray and Ultrasound Tissue-Equivalent Fluids

(a) Ultrasound speed measurements

One of the most important elements required for the combined x-ray/ultrasound imaging device is the identification of an x-ray equalizing and ultrasound coupling fluid. Initially, we assumed that the ideal fluid medium would have the same x-ray attenuation and speed of sound characteristics as average breast tissue and have minimal ultrasound attenuation. Constantinou described two liquids that satisfied the x-ray attenuation criterion. One is a mixture of water (32.43% by weight), propanol (27.03%) and butanediol (40.54%).[Constantinou, 1982] The other is a mixture of water (29.72%), n-propanol (49.55%) and glycerol (20.72%). [Constantinou, 1998]. Since the breast has been simulated by BR-12 material which is 50% water/50%fat equivalent [Hammerstein, 1979], a 50% fat/50% water emulsion would also meet the x-ray attenuation criterion. After much investigation a commercially available emulsion with these characteristics was found. It is Microlipid, which is sold by MeadJohnson (Evansville, Indiana). Microlipid is a special dietary supplement, which is used in oral and tube feedings. Its main ingredients are safflower oil and water.

To verify the x-ray attenuation properties of these liquids they were used to fill a plastic vessel containing a phantom (CIRS Model 11A) that simulates a 4.5-cm-thick 50% adipose/50% glandular tissue breast. The liquid surrounded the phantom and was filled to a level coinciding with the top of the phantom. X-ray mammograms were produced, and the optical densities in the liquid region and center of phantom region were compared. All of the liquids produced optical densities just beyond the breast periphery that were comparable with the optical density near the center (within 0.18 OD), as desired.

The ultrasound properties of the liquids were measured experimentally in our laboratory using a substitution technique. A large water tank was employed in which the transducer and a planar reflector with known amplitude reflection coefficient were carefully aligned to insure the ultrasound beam was normal to the reflector. A test vessel consisting of a cylinder with Saran transmission windows was placed between the transducer and reflector and its surface was aligned perpendicular to the incident beam. The acoustic spectra and reception time of the echo returning to the transducer were compared for the condition when the test vessel was filled with water and when the test vessel was filled with each liquid of interest. Speed and attenuation values were measured for two transducers having center frequencies of 5 and 10 MHz. The

frequency ranges for these transducers were 2-7 MHz and 6.5-13 MHz, respectively. The speed of sound and attenuation results are listed in Table 1, below.

Table 1. Measured Speed of Sound and Attenuation Properties of Potential Liquid Bolus Materials

Liquid	Speed of Sound in m/sec		Attenuation coefficient in dB/cm/MHz	
	(2 – 7 MHz)	(6.5-13 MHz)	(2 – 7 MHz)	(6.5-13 MHz)
Microlipid	1465	1483	1.03	1.03
Glycerol mixture	1422	1488	0.44	0.73
Butanediol mixture	1522	1588	0.24	0.42

These values are to be compared with an average speed of sound of 1490 m/sec (range: 1430-1560 m/sec) [Scherzinger, 1989] and an average attenuation of 0.75 dB/cm/MHz$^{1.5}$ [Foster, 1979] with a range of about 9.5-12.6 dB/cm at 7 MHz [McDaniel, 1977] for normal breast tissue. One concern with a difference in speed of sound is refraction at oblique incidence. However, all of the speeds of sound of the liquids are within 7% of the speed in breast tissue, and even in the worst case the resulting refraction would be minor or negligible (e.g., using Snell's law a beam passing through the Butanediol mixture that is incident on the breast at 30 degrees would be refracted to 28 degrees (sin 28°/sin 30 ° = 1490/1588)). Minimum attenuation is desired, and the liquid that best meets this specification is the Butanediol mixture. It should be noted that at 10 MHz, all of the liquids are less attenuating than average normal breast tissue (10.3, 7.3, and 4.2 dB/cm for the Microlipid, Glycerol and Butanediol mixtures, respectively vs. 23.7 dB/cm = (0.75 x $10^{1.5}$) for average normal breast tissue.)

The primary disadvantages of both the glycerol and the Butanediol mixtures are the strong fumes they emit which may not be acceptable to patients. The Microlipid liquid is very similar to cream and does not emit fumes. It would be much better tolerated by patients; however, it has a relatively high acoustic attenuation, which could compromise ultrasound image quality at the extreme periphery of the breast. Also, it is white in color rather than clear like the other two mixtures. The white color may make it more difficult to see and therefore position the breast in the scan window and to determine the presence of possible artifact-generating air bubbles.

Other liquids have recently been analyzed. Their selection was based on the Dynamic Range and Contrast Study described below:

(b) Dynamic Range and Contrast Study

A primary advantage of using the liquid medium adjacent to the breast is that it reduces the dynamic range requirements for the x-ray detector. Such equalization is especially useful for screen-film detectors, which are characterized by a non-linear response that results in reduced contrast at high and low exposures. It is also useful for digital detectors because it facilitates the acquisition of the entire image at an optimal signal-to-noise ratio which cannot be accomplished with postprocessing techniques such as those proposed by Byng et al [Byng, 1997] and Bick et al [Bick, 1996]. As demonstrated by Lam and Chan [Lam, 1990] the liquid medium will reduce the amount of scattered radiation striking the detector at the peripheral region, which should improve image contrast. It will however increase beam hardening in this region, which will reduce image contrast. Taking all factors into account, there is an overall gain in image contrast. We performed a computer simulation study to quantify the effects of the liquid bolus material on dynamic range and contrast. Details of this study are contained in our 1998 Annual Report.

In summary, our study showed that bolus materials such as fat, and adipose tissue would be the best choice. These materials will reduce the dynamic range requirements for detection and display while producing only mild to moderate reductions in contrast due to beam hardening. So long as the detector has sufficient signal-to-noise ratio, much of the contrast reduction can be compensated for by employing an increased slope in the contrast transfer curve for display.

(c) Evaluation of Different Types of Fats (Oils)

(i) Ultrasound properties

The most convenient fats to use as our bolus material are vegetable oils since they are inexpensive and readily available. The primary disadvantages with using fats in general are their greasiness and the difficulties associated with their cleanup. We consulted with a pharmacy professor, who suggested using a less greasy oil like isopropyl myristate (IPM). This is an oil that is commonly used in the cosmetics industry. We contacted a supplier who suggested that we also investigate two other oils that are used in cosmetics: isopropyl palmitate (IPP) and isostearyl lactate (IL). The material safety data sheets for IPP and IPM indicate that formulations containing 45.6% IPP and 43% IPM produce no signs of skin irritation or sensitization. IL is safe at even higher concentrations. We produced mixtures of these oils with other vegetable oils and measured their ultrasound properties as well as the properties of the pure oils using a technique similar to that described above. The measurements were made only with the wideband 5 MHz transducer because the other transducer was out of commission. The results of these measurements are summarized in the following table.

From this table, pure IPP and pure ILL are nearly ideal in terms of their low ultrasound attenuation, however, their speeds of sound (1340 and 1326 m/sec, respectively) are considerably slower than the average speed in breast tissue (1490 m/sec) and therefore could produce refraction artifacts. There is also a concern that the pure substances may cause skin irritation. Several of the mixtures have both speeds of sound close to that of breast tissue and low ultrasound attenuation relative to the attenuation of breast tissue (attenuation of breast tissue ~ 9.5 - 12.6 dB/cm @ 7 MHz). These are bolded in the table. The best appears to be a mixture of 60% Sunflower oil and 40% IPM.

Table 4. Measured Speed of Sound and Attenuation Properties of Oil-based Bolus Materials

Substance	Speed in m/sec	Attenuation (dB/cm) = a f(MHz)**b dB/cm at 6 MHz	dB/cm at 8 MHz	a	b
100% Sunflower (Sun)	1454	1.9	3.17	0.046	2.047
100% Mineral (Min)	1403.7	1.3	2.26	0.027	2.177
100% Soy	1458.8	1.97	3.37	0.053	2.006
100% IL	1419.1	2.26	3.87	0.054	2.079
100% IPP	1340	0.4	0.71	0.002	3.024
100% IPM	1325.7	0.43	0.69	0.003	2.614
60% Soy 40% IPP	**1439.7**	**0.98**	**1.56**	**0.02**	**2.154**
20% IL 80% Sun	1470	1.82	3.14	0.055	1.949
60% Sun 40% IPM	**1470**	**0.86**	**1.54**	**0.025**	**1.974**
60% Sun 40% IL	1459.1	1.87	3.19	0.044	2.082
40% IPM 20% IL 40% Min	1390.7	0.77	1.27	0.035	1.732
60% Sun 40% IPP	**1428.6**	**0.98**	**1.69**	**0.024**	**2.064**
40% IPP 10% IL 50% Soy	**1426.3**	**0.96**	**1.59**	**0.012**	**2.41**
60% Soy 40% IPM	**1426.5**	**0.88**	**1.54**	**0.021**	**2.074**
0% IPM 80% Sun	1475.3	1.14	2.03	0.024	2.138

(ii) X-ray properties

The x-ray attenuation properties of the oils listed above were evaluated. We used identical syringes filled with each of the oils. The syringes were laid side by side. A stepwedge-

like breast simulating plastic phantom (BR-12, 50% water/50% fat) was placed next to the syringes and a radiograph was taken. The optical densities in the images of the oils were compared with those of various thicknesses of the breast simulating plastic. We found that the oils each had about the same x-ray attenuation, and a 2-cm thickness of oil had approximately the same attenuation as 1.25 cm of BR-12. The results thus indicate that the oils would perform very well for exposure equalization.

(H) Investigation of Plastics for the Compression Paddle

Conventional x-ray mammography systems employ compression paddles that are made of 1/16 inch thick Lexan. This plastic is ideal in terms of its high flexural and tensile strength and low x-ray attenuation; however, it exhibits considerable ultrasound attenuation, which will degrade the ultrasound image. A literature search was performed to find the acoustic properties of plastics. The most thorough listing that included attenuation properties was in a paper by Hung and Goldstein [Hung, 1983]. Using the slope and intercepts of attenuation vs. frequency information in this paper, the attenuations of the various plastics were computed at the 5, 7.5 and 10 MHz frequencies commonly employed in breast imaging. These values as well as the calculated amplitude reflection coefficients are listed in Table 5, below

Table 5. Ultrasound Amplitude of Reflection and Attenuation Coefficients of Some Common Plastics

Plastic	Amplitude Reflection Coefficient	Attenuation @ 5 MHz (dB/cm)	Attenuation @ 7.5 MHz (dB/cm)	Attenuation @ 10 MHz (dB/cm)
Plexiglas	0.371	4.62	6.53	8.45
Nylon	0.344	11.06	16.91	22.76
Teflon	0.374	37.57	57.67	77.77
Oilon PV-80	0.366	30.15	46.83	63.50
Lexan	0.280	20.94	31.72	42.49
Delrin	0.384	26.57	42.15	57.72
Hi impact polystyrene	0.214	10.53	15.93	21.33
UMHW polyethylene	0.212	7.97	12.19	16.42
Low density polyethylene	0.129	24.53	37.66	50.78

Based on the information in this table, the best plastic in terms of attenuation coefficient is Plexiglas. For example at 10 MHz, it is 5 times less attenuating per cm than Lexan. However, Plexiglas is more brittle and less strong than Lexan. As a result, the required thickness for a compression paddle made of Plexiglas is 8 to 10 mm which is 5 times greater than the 1/16 inch (1.59 mm) required thickness of Lexan. Thus, the effective attenuation of the two paddles are nearly identical, and since the reflection coefficient for Lexan is less, it would still be the best choice of those listed above.

Another plastic that has great promise is Mylar ($C_{10}O_4H_8$). It is commonly used in synthetic drumheads (e.g. those manufactured by REMO, Inc. of North Hollywood, CA). A thin membrane of Mylar could be stretched to form a compression paddle with the desired high flexural strength. Since it is very thin (~37.5 - 350 microns), the anticipated acoustic and x-ray attenuation are low. The computed x-ray attenuation of a 250-micron Mylar paddle is 2% at an average mammography energy of 20 keV. This is less than the 9% attenuation of a conventional 1/16 inch Lexan paddle at this energy.

A study was performed to investigate the applicability of a Mylar compression paddle to ultrasound imaging. A tissue mimicking ultrasound phantom (CIRS Near Field Ultrasound Phantom, Model 50) was imaged with a GE LOGIQ 700 ultrasound instrument using a model M12L high frequency 1.5-D linear array transducer. This phantom contains simulated 1.6 mm, 2.0 mm, and 2.4 mm diameter cylindrical lesions that have a scatter level about 15 dB below background. The transducer was operated in its 9 MHz mode, and the phantom was imaged with no plastic, 125 microns Mylar, 250 microns Mylar, 350 microns Mylar and 1/16 inch Lexan between the transducer face and top surface of the phantom..

There was almost no difference between the images generated with no plastic and those with 125 and 250 microns of Mylar. The depth of penetration was reduced by only about 1 mm. Slightly more degradation was observed with 350 microns of Mylar (depth of penetration reduced by about 3 mm), and significant degradation was observed with the 1/16 inch slab of Lexan (depth of penetration reduced by about 8 mm). Thus, Mylar appears to be a very promising material for the compression paddle of our combined x-ray/ultrasound imaging device.

(I) Combined x-ray/ultrasound imaging - Preliminary study

Based on the investigation described above, we built a compression paddle with a thin Mylar window for the compressible tank. Our investigations indicated that 60% sunflower oil, 40% IPM mixture would be ideal for combined x-ray and ultrasound imaging, and we initially planned to use this mixture. However, in our preliminary tests, we discovered that the IPM dissolves any grease (e.g. petroleum jelly, silicone grease, etc.) that is placed around the rubber seal between the compression paddle and the tank, resulting in significant leaks. Therefore, use of this mixture will require a re-design of the compression paddle / immersion tank system to one that does not rely on a movable seal between the compression paddle and the tank. We have initiated work on developing such a system. One design we have conceived of would employ a bellows device to connect the compression paddle to the tank.

In order to perform a preliminary study with our present compression paddle/tank system and avoid the leakage problem described above, we decided to employ pure sunflower oil as the

immersion fluid. As can be seen in Table 4, above the speed of sound of sunflower oil (1454 m/sec) is close to that of breast tissue, and its acoustic attenuation though not as low as the sunflower oil/IPM mixture is still lower than that of breast tissue.

We also worked with CIRS, Inc. a manufacturer of tissue-equivalent phantoms, to design and built a compressible x-ray and ultrasound breast-simulating phantom. Prototype phantoms were built and tested. They were made of special emulsions that simulate the x-ray attenuation, ultrasound speed of sound, and ultrasound attenuation properties of breast tissue. The current version of the phantom simulates a thick patient breast with regions of dense parenchyma as shown in Fig. 1. Several simulated masses and cysts and groups of microcalcifications were embedded in various regions of the phantom. The phantom also has a skin layer with attenuation properties similar to fibroglandular tissue. This phantom was used for the combined x-ray/ultrasound imaging experiments.

A picture of the prone mammography system with the compression tank and compression paddle is shown in Fig. 3. The breast phantom was immersed in the oil in the compressible tank and compressed with the Mylar paddle. X-ray images of the phantom were recorded with a computed radiography (CR) stimulable phosphor plate and read-out as a digital image. The phantom was subsequently scanned in the compressed mammography geometry with a GE Logiq 700 ultrasound system. The ultrasound transducer was scanned across the compression paddle/scanning window and multiple adjacent ultrasound slices were recorded. Examples of the x-ray mammogram and the ultrasound images of the phantom are shown in Fig. 1 and Fig. 2, respectively. The 3-D ultrasound data set from the scans was used to generate an ultrasound "projection "image, which is shown in Fig. 2(a). Individual slices at locations within this projection image are shown in Fig. 2(b). Note the strong correspondence between the ultrasound projection image and the CR x-ray image. The ultrasound slices at specific locations within the ultrasound projection image provide a 3-D perspective that cannot be appreciated in the CR x-ray image. The ultrasound images are of high quality indicating little or no degradation due to the Mylar scanning window and sunflower oil. Simulated masses could be identified on both the x-ray and the ultrasound images.

Because the preliminary results are promising, we plan to submit grant applications to funding agencies to continue the development of the combined x-ray/ultrasound imaging system.

(J) Automated segmentation of dense tissue region on mammograms

One of the steps required in an automated combined x-ray and ultrasound imaging procedure is computerized localization of the dense tissue regions on the mammogram in real time. One of the graduate students at the Department of Nuclear Engineering and Radiological Sciences chose this topic as her master thesis project. After the master thesis [Shah, 1998] was completed, the project was further pursued by one of our research fellows. The graduate student and research fellow developed a computer program that analyzes the gray level histogram of a digital mammogram. In this approach, the breast density is classified into one of four density classes by the computer based on the shape of the histogram. For each class, a rule-based method is designed to automatically choose a gray level threshold to segment the dense regions from the fatty breast tissue background. Large dense regions can then be identified as the location for ultrasound scanning. An example of a segmented dense region on a digitized mammogram is shown in Fig. 4.

In our preliminary study described above, the dense region on the phantom breast image was manually identified because there is no interface between our computed radiography system and the prototype breast scanning device. However, if a direct digital detector is available in the prone mammography system in the future, the different steps in the combined x-ray/ultrasound procedure can be interfaced and the entire process automated. The computer-identified location of the dense region can be fed into a personal computer, which, in turn, can control the x-y translator that automatically moves the ultrasound transducer to the desired location for scanning.

Based on discussion with our radiologists, we also found that this automated breast density segmentation and classification program had important application in estimation of breast cancer risk. It has been reported in the literature [Oza, 1993] that breast density has strong correlation with the development of breast cancer. We have therefore conceived a new project to develop an image analysis tool for estimation of breast density and breast cancer risk. We have submitted an application to the USAMRMC Breast Cancer Program in June of this year to request funding for the new project.

(K) Ultrasound scanning device

A first generation ultrasound transducer translating system was developed for the combined x-ray and ultrasound-imaging device. Four Mechanical Engineering students enrolled in a Senior Design course at the University of Michigan assisted us with the design and construction of the system. The design criteria included 1) the translation system (tracks, stepper motors, etc.) fit completely on the compression paddle and not intrude on the ultrasound scanning and x-ray imaging window, 2) the translation system move the ultrasound transducer at speeds of 1 mm/sec to 100 mm/sec (1 mm/sec for fine detail scanning and 100 mm/sec for quick positioning at abnormalities for subsequent scanning), and 3) the system include a mechanism to keep the transducer in contact with a thin layer of ultrasound scanning gel applied to the scanning window.

The system that was designed and built is shown in Fig. 5. The students custom built the shafts and lead screws of the translation system. They selected stepper motors that met the speed and torque requirements, and employed a stepper motor controller system manufactured by Arrick Robotics (Hurst, Texas). A spring loaded ultrasound transducer holder was designed and built to insure the transducer pressed against the gel on the scanning window.

The prototype device that was built generally meets the requirements described above. However, a few problems will have to be fixed as is often the case with first generation devices. In our preliminary tests, we found that the system was noisy because of a bent shaft that caused vibration in one of the motor supports. A new stepping motor was ordered to replace the one with the bent shaft. Another problem was that the transducer holder did not position the transducer close enough to contact the scanning window. The design of the transducer holder will have to be modified to improve the contact. Although this prototype was not ideal, it did demonstrate that a computerized controlled ultrasound transducer translating system can be built and attached to the compression paddle for a combined x-ray and ultrasound imaging system.

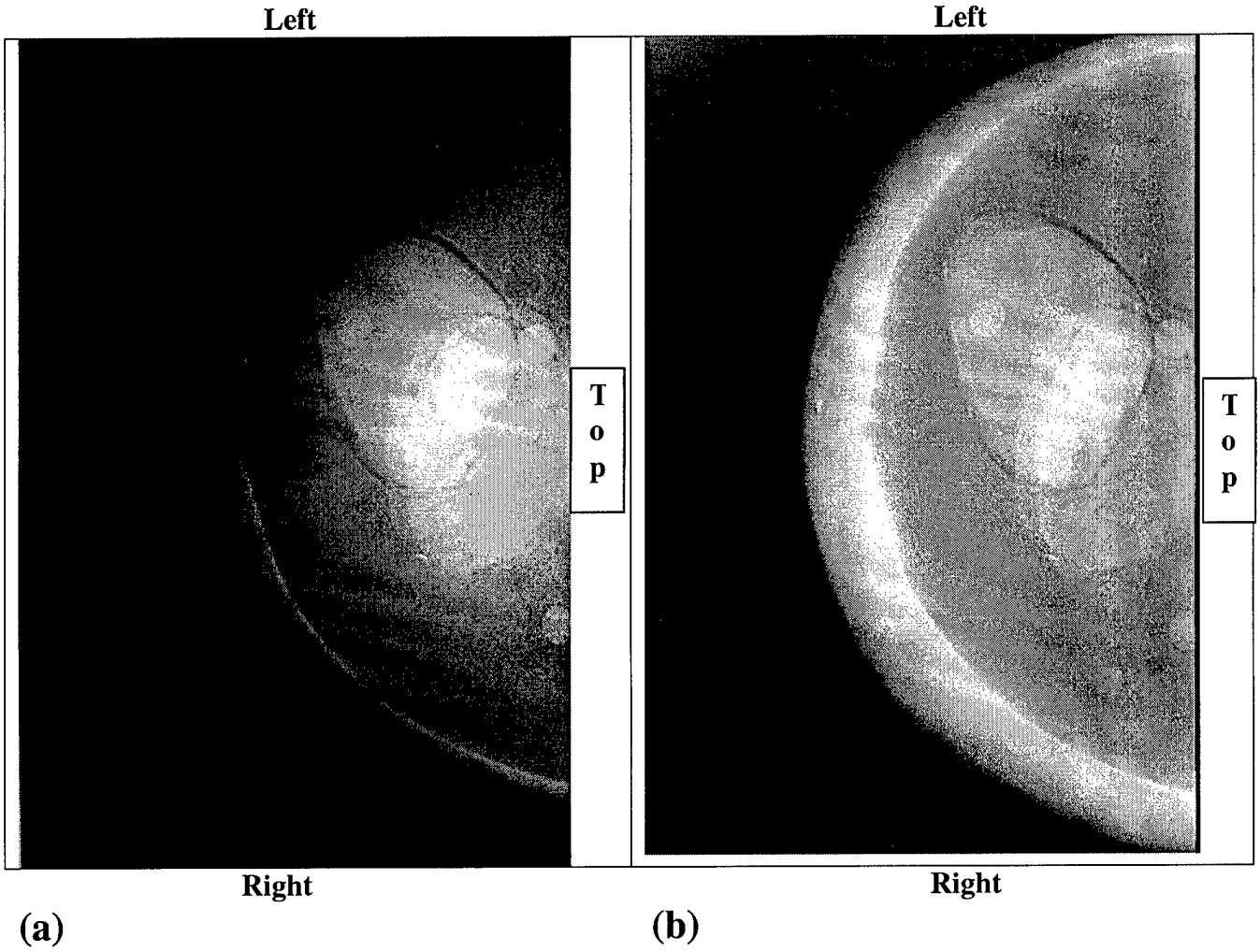

Fig. 1 Computed radiography x-ray images of the CIRS breast phantom. (a) the unequalized image produced with no oil surrounding the phantom. (b) the equalized image produced with oil surrounding the phantom. Note the improved visibility of the peripheral tissue in the equalized image (b). Ultrasound images corresponding to (b) were also generated with our combined imaging system. For the ultrasound images, the transducer was scanned manually along the Mylar compression paddle/scanning window. Examples of the ultrasound images are shown in Fig. 3 below. Please note the top, left, and right markers in both the ultrasound and the x-ray images.

Top

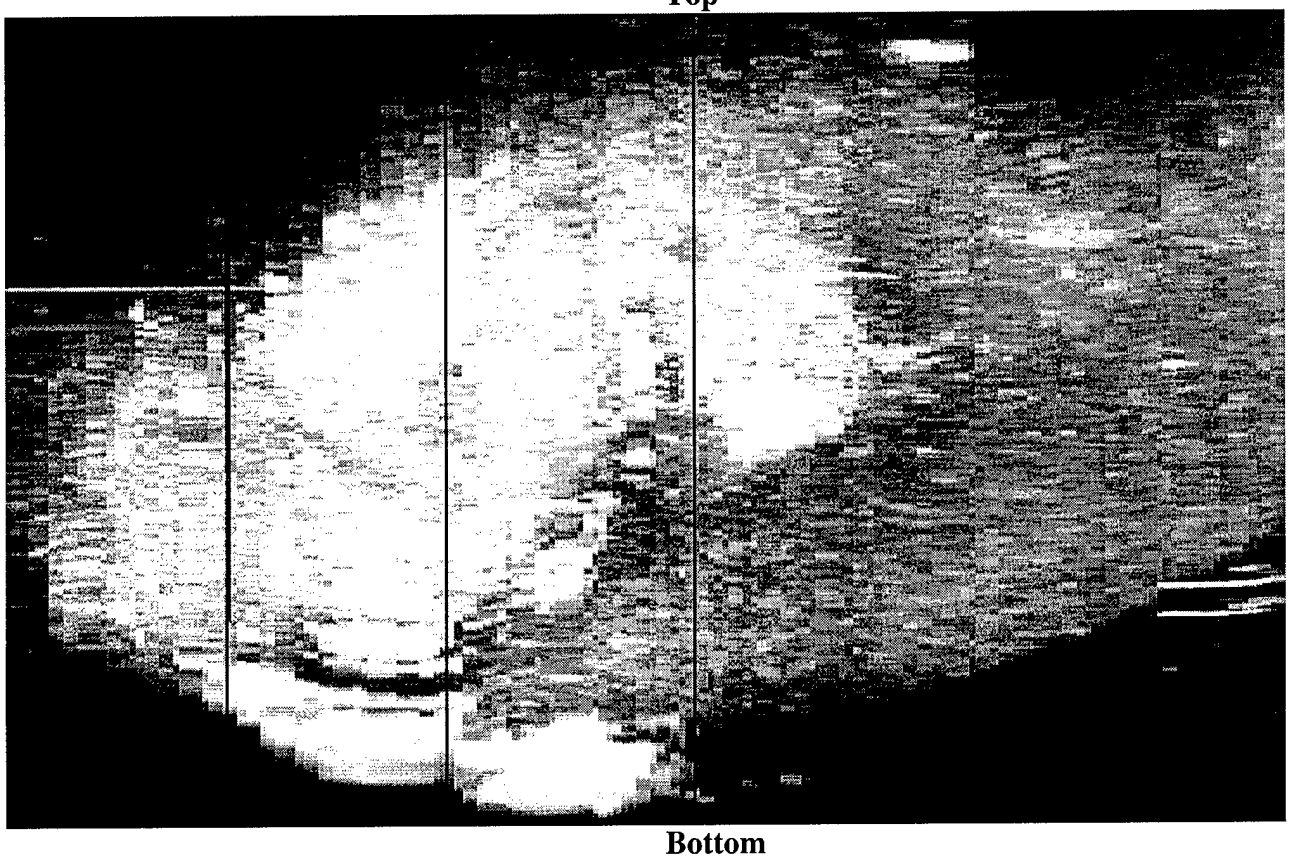

Bottom

↑ **Left** Slice: 165 131 93 **Right** ↑

(a)

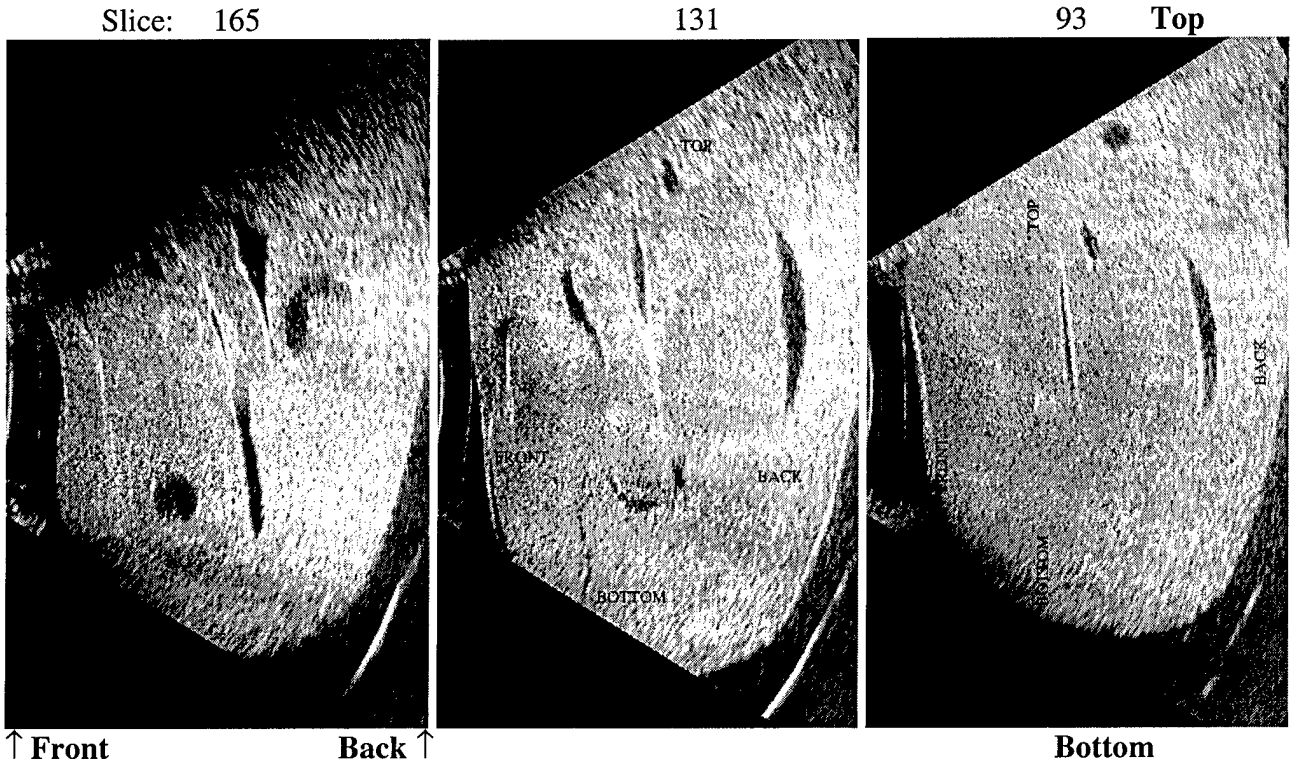

(b)

Fig. 2 B-mode ultrasound images of the CIRS breast phantom. Multiple adjacent ultrasound "slices" were generated. Each slice extended from the front (compression paddle position) to the back (CR detector position) of the phantom. A "projection" image displaying the sum of the echo amplitudes along each line extending from the front to the back was computed and is displayed in Fig. 2(a). This "projection" image has a direct correspondence with the x-ray transmission images displayed in Fig. 1. Individual B-mode ultrasound "slices" are displayed below the "projection" image. Note the high quality of the ultrasound images indicating little or no degradation due to the Mylar scanning window and oil transmission medium. The ultrasound images show locations of cyst and mass-like objects, and provide a 3-D perspective that cannot be appreciated in the x-ray image.

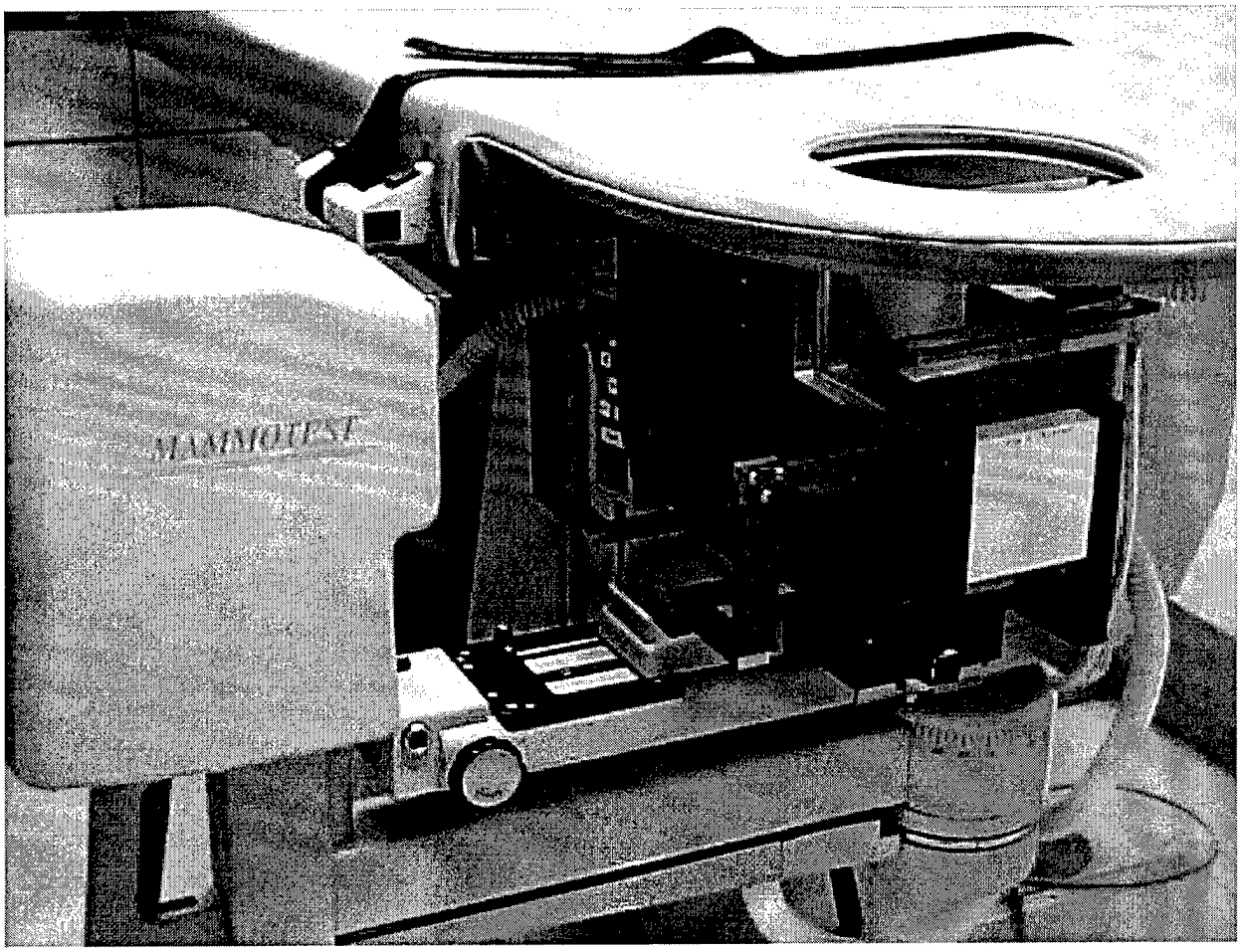

(a)

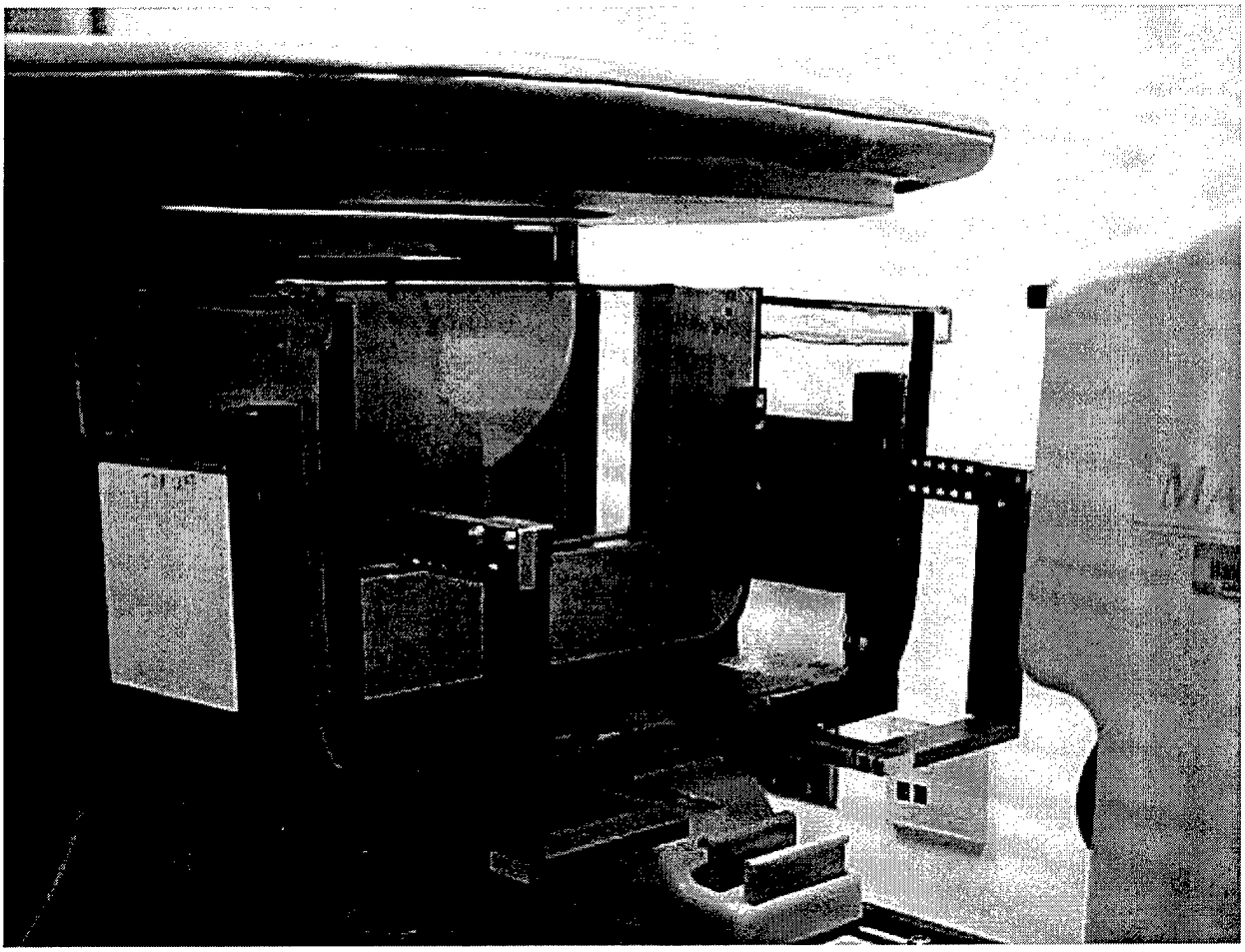

(b)

Fig. 3. The x-ray equalization compressible tank installed on a prone mammography system. (a) The x-ray tube is angulated at 90 degrees for a lateral view. Note that the compressible tank rotates with the x-ray tube support arm to any angle. (b) The x-ray tube is set at 0 degree for a craniocaudal view. The compression paddle with the thin Mylar window can be seen in both pictures. The tank will be filled with a tissue-equalivalent fluid for x-ray equalization and ultrasound coupling.

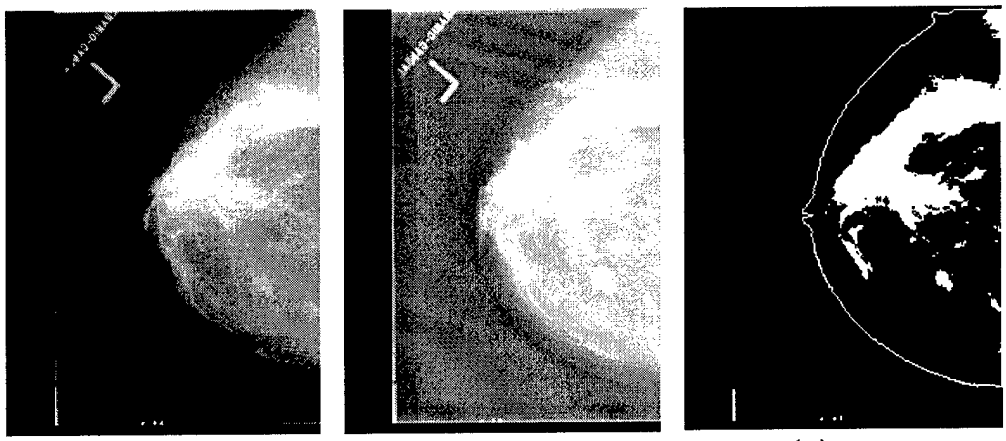

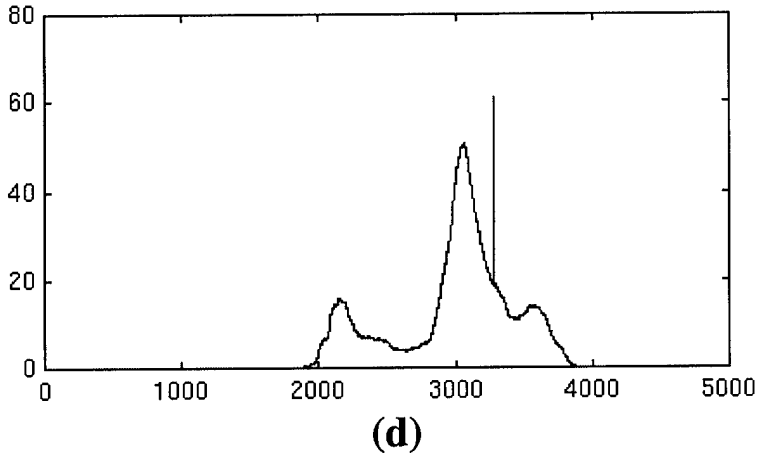

Fig. 4. The automated breast density segmentation program detects the breast border and analyzes the gray level histogram of the breast image. A gray level threshold is then automatically determined by the computer and the density tissue isolated from the fatty breast tissue. (a) Digitized mammogram, (b) digitally enhanced mammogram, (c) binary image indicating fibroglandular tissue (white) separated from fatty tissue (black), and (d) gray level histogram of breast image and the computer-selected threshold indicated by a vertical line.

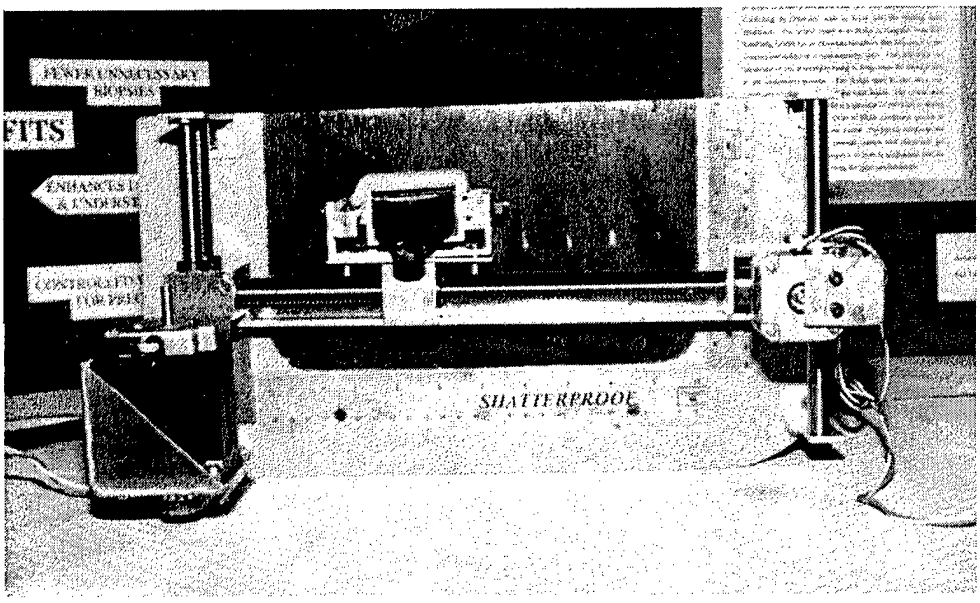

Fig. 5. The prototype motorized x-y translator for scanning the ultrasound transducer across the Mylar window on the compression paddle. In this illustration, the device was mounted on a wooden model of the compression paddle. The dark gray area represents the Mylar window. The scanning arm will be "parked" at the lower portion of the window, out of the way of the x-ray beam path, during x-ray exposure.

(7) Key Research Accomplishments

With the support of the grant, we have conducted investigations and completed the following tasks:

Task 1. Develop computerized breast border detection programs for mammograms and breast shape classification scheme

Task 2. Design and build exposure equalization filters and evaluate their effects by phantom studies

Task 3. Evaluate mammographic patient dose by Monte Carlo simulation studies

Task 4. Monte Carlo modeling of mammographic imaging systems and optimization of imaging techniques with various image detectors

Task 5. Design and build custom breast-tissue-equivalent phantoms for x-ray and ultrasound imaging

Task 6. Evaluate effects of equalization on image quality and conduct observer performance studies.

Task 7. Develop a novel combined x-ray equalization and ultrasound imaging system for improved evaluation of dense breasts and mammographic lesions

Task 8 Design and build a compressible tank for combined x-ray equalization and ultrasound imaging with a prone mammographic system.

Task 9. Evaluate tissue-equivalent fluids for x-ray equalization and ultrasound coupling

Task 10. Design and build a special compression paddle for x-ray and ultrasound transmission

Task 11. Develop breast density segmentation program for automated localization of dense tissue regions on digitized mammograms to identify regions of interest for ultrasound scanning.

Task 12. Perform phantom study to evaluate the feasibility of combined x-ray and ultrasound scanning using the prototype compressible tank and tissue-equivalent fluid.

Task 13. Design and build a prototype motorized ultrasound scanning device for combined x-ray and ultrasound imaging

Tasks 1 to 6 correspond to Tasks 1, 2, 4, 5, 7, and 8 of the Statement of Work in our original proposal. In the course of the study, we conceived the new idea of developing a compressible tank containing tissue-equivalent fluid for x-ray equalization in a prone mammography system. We further developed the system into a combined x-ray and ultrasound imaging that has the promise to improve breast cancer detection and diagnosis in dense breasts.

Tasks 7 to 13 are investigations devoted to the development of this novel imaging system. We have built a prototype system and demonstrated the feasibility of this new approach with phantom studies. These tasks replace Tasks 3, 6, 9, and 10 in the original Statement of Work. We believe that our new approach is more versatile and useful than the originally proposed external filter device. As a result of our research efforts, we have published four journal articles, two Master Theses, six abstracts and presentations, and generated two new grant applications for continued research in this and other directions for breast cancer detection.

(8) Reportable Outcomes

Publications as a result of this grant

Journal Articles:

1. Liu B, Goodsitt MM, Chan HP. Normalized average glandular dose in magnification mammography. Radiology. 1995; 197:27-32.

2. Goodsitt MM, Chan HP, Liu B. Investigation of the line-pair pattern method for evaluating mammographic focal spot performance. Medical Physics 1997; 24: 11-15.

3. Goodsitt MM, Chan HP, Liu B, Morton AR, Guru SV, Keshavmurthy S, Petrick N. Classification of compressed breast shape for the design of equalization filters in mammography. Medical Physics 25: 937-948, 1998.

4. Keshavmurthy SP, Goodsitt MM, Chan HP, Helvie MA. Design and evaluation of an external filter technique for exposure equalization in mammography. Medical Physics 1999; 26: 1655-1669.

Abstracts and presentations:

1. Goodsitt MM, Chan HP, Liu B, Guru S, Morton R. Compressed breast shape classification for the design of mammography equalization filters. Presented at the 38th Annual Meeting of the American Association of Physicists in Medicine. Philadelphia, Pennsylvania, MA, July 21-25, 1996. Medical Physics 1996; 23: 1108.

2. Liu R, Goodsitt MM, Chan HP. Normalized average glandular doses in magnification mammography. Presented at the 36th Annual Meeting of the American Association of Physicists in Medicine. July 24-28, 1994, Annaheim, California. Medical Physics 1994; 21: 917.

3. Morton AR, Chan HP, Goodsitt MM. Automated model-guided breast segmentation algorithm. Presented at the 38th Annual Meeting of the American Association of Physicists in Medicine. Philadelphia, Pennsylvania, MA, July 21-25, 1996. Medical Physics 1996; 23: 1107-1108.

4. Keshavmurthy SP, Chan HP, Goodsitt MM. Design of exposure equalization filters for mammography. Presented at the 39th Annual Meeting of the American Association of

Physicists in Medicine. Milwaukee, Wisconsin, July 27-31, 1997. Medical Physics 1997; 24: 1018.

5. Keshavmurthy SP, Chan HP, Goodsitt MM. Evaluation of x-ray detectors for digital mammography - Monte Carlo simulation study. Presented at the 83rd Scientific Assembly and Annual Meeting of the Radiological Society of North America, Nov 30-Dec 5, 1997, Chicago, Illinois. Radiology 1997; 205(P): 303.

6. Chan HP, Goodsitt MM, Keshavmurthy S, Helvie MA, Adler DD. Development of an x-ray beam equalization technique for improved mammographic imaging. Poster presentation at the Era of Hope Meeting, Washington, DC. October 31-November 4. Proceedings of The Department of Defense Breast Cancer Research Program Meeting, 1997; 1: 113-114.

Master Theses:

1. A. Ray Morton III, "Design of an X-Ray Beam Equalization Filter for Mammographic Imaging", Master Thesis, Rackham School of Graduate Studies, Department of Environmental and Industrial Health, University of Michigan, Ann Arbor, 1995.

2. Sheila M. Shah, "An Algorithm for the Quantitative Analysis of Mammographic Breast Density", Master Thesis, Rackham School of Graduate Studies, Department of Nuclear Engineering and Radiological Sciences, University of Michigan, Ann Arbor, 1998.

(9) Conclusion

In this project, we have designed and built external x-ray equalization filters for mammographic imaging. We performed simulation studies and phantom experiments to evaluate the number of required filters and the effects of x-ray equalization on mammographic image quality. The results demonstrated that compressed breasts can be classified into a small number of shapes and therefore a small number of filters could be employed for equalization. The results also showed x-ray equalization can effectively reduce the exposure dynamic range of the images and improved the visibility of mammographic features. In the course of the study, we conceived the new idea of developing a compressible tank containing tissue-equivalent fluid for x-ray equalization in a prone mammography system. We further developed the device into a combined x-ray and ultrasound imaging system. We have built a prototype system and demonstrated the feasibility of this new approach with phantom studies. The results indicate the advantages of the new approach: (1) x-ray equalization with a compressible tank and tissue-equivalent fluid is truly patient specific for breasts of any size and shape, and for any mammographic view, (2) because this technique does not employ a solid external filter there will be no artifacts that may be caused by misalignment between such a filter and the breast, (3) combined x-ray and ultrasound imaging can be developed with such a system, (4) improved correlation between mammographic and ultrasound findings may improve breast cancer diagnosis, and (5) automatic ultrasound scanning of fibroglandular regions may improve breast cancer detection in dense breasts. Although our prototype system demonstrates the promise of the approach, several technical problems remain to be resolved including (1) design of a more

practical compressible tank that is more leak-proof and can be cleaned efficiently, (2) improved design of a compression paddle that can provide the compression force required for mammography and is transparent to ultrasound, and (3) search for an inexpensive and easy-to-clean x-ray and ultrasound tissue-equivalent fluid. Finally, more extensive phantom and patient studies will be needed to evaluate the image quality of such a system and its effects on breast cancer detection and diagnosis in dense breasts.

(10) References

Baines CJ, Miller AB, Wall C, et al: Sensitivity and specificity of first screen mammography in the Canadian National Breast Screening Study: A preliminary report from five centers. Radiology 160:295-298, 1986.

Baker LH: Breast Cancer Detection Demonstration Project: A Five-Year Summary Report. CA Cancer J Clin 32:194-225, 1982.

Baxter B, Ravindra H, Normann RA: Changes in lesion detectability caused by light adaptation in retinal photo-receptors. Invest Radiol 17:394-401, 1982.

Bick U, Giger ML, Schmidt RA, Nishikawa RM, Doi K. Density correction of peripheral breast tissue on digital mammograms. RadioGraphics 1996; 16:1403-1411

Bunch PC, Huff KE, Van Metter R: Analysis of the detective quantum efficiency of a radiographic screen/film system. J Opt Soc Am A 4:902-909, 1987.

Byng JW, Critten JP, Yaffe MJ. Tissue-equalization processing for mammographic images, Radiology 1997;203:564-568.

Conway WF, Hayes CW, Brewer WH, Occult breast masses: Use of mammographic localizing grid for US evaluation, Radiology 1991; 181: 143-146.

Constantinou C, Phantom materials for radiation dosimetry. I. Liquids and gels, BJR 1982; 55: 217-224.

.Constantinou C, Tissue substitutes for particulate radiations and their use in radiation dosimetry and radiotherapy (Ph.D. Thesis, University of London) and personal communication (1998)

D'Agincourt L: Technique is everything when breast is dense. Diagnostic Imaging, September: 57-61, 1993.

Dance DR, Persliden J, Carlsson GA. Calculation of dose and contrast for two mammography grids. Physics Med. Biol. 1992; 37, 235-45.

Foster FS and Hunt JW. Transmission of ultrasound beams through human tissues – focusing and attenuation studies, Ultrasound Med Biol 1979;5:257-268.

Goodsitt MM, Chan HP, Liu B, Morton AR, Guru SV, Keshavmurthy S, Petrick N. Classification of compressed breast shape for the design of equalization filters in mammography. Medical Physics 25: 937-948, 1998.

Hammerstein GR, Miller DW, White DR, Masterson ME, Woodard HQ, Laughlin JS. Absorbed radiation dose in mammography, Radiology 1979;130:485-491.

Haug PJ, Tocino IM, Clayton PD, Bain TL: Automated management of screening and diagnostic mammography. Radiology 164:747-752, 1987.

Hung B and Goldstein A. Acoustic parameters of commercial plastics, IEEE Transactions on sonics and ultrasonics. 1983; SU-30: 249-254.

Jennings RJ, Fewell TR. Spectral simulation and photon design program suite, FDA, Rockville, MD 20857

Keshavmurthy SP, Chan HP, Goodsitt MM. Evaluation of x-ray detectors for digital mammography - Monte Carlo simulation study. Presented at the 83rd Scientific Assembly and Annual Meeting of the Radiological Society of North America, Nov 30-Dec 5, 1997, Chicago, Illinois. Radiology 1997; 205(P): 303.

Keshavmurthy SP, Goodsitt MM, Chan HP, Helvie MA. Design and evaluation of an external filter technique for exposure equalization in mammography. Medical Physics 1999; 26: 1655-1669.

Lam KL, Chan H-P. Effects of x-ray beam equalization on mammographic imaging. Medical Physics 1990;17: 242-249.

Liu B, Goodsitt MM, Chan HP. Normalized average glandular dose in magnification mammography. Radiology. 1995; 197:27-32.

McDaniel GA. Ultrasonic attenuation measurements on excised breast carcinoma at frequencies from 6 to 10 MHz. 1977 Ultrasonics Symp Proc, IEEE Cat. No. 77CH1264-ISU, 234-236 (Note: includes normal tissue information).

Morton AR III, "Design of an X-Ray Beam Equalization Filter for Mammographic Imaging", Master Thesis, Rackham School of Graduate Studies, Department of Environmental and Industrial Health, University of Michigan, Ann Arbor, 1995.

Morton AR, Chan HP, Goodsitt MM. Automated model-guided breast segmentation algorithm. Presented at the 38th Annual Meeting of the American Association of Physicists in Medicine. Philadelphia, Pennsylvania, MA, July 21-25, 1996. Medical Physics 1996; 23: 1107-1108.

Oza AM, Boyd NF. Mammographic parenchymal patterns: A marker of breast cancer risk. Epidemiologic Reviews 1993; 15: 196-208.

Rezentes PS, de Almeida A, Barnes GT. Mammography grid performance. Radiology 1999; 210: 227-232.

Richter K, Prihoda H, Heywang Kobrunner SH, Hamm B. Description and first clinical use of a new system for combined mammography and automated clinical amplitude/velocity reconstructive imaging breast sonography. Invest Radiol 1997;32:19-28.

Scherzinger AL, Belgam RA, Carson PL, Meyer CR, Sutherland JV, Bookstein FL and Silver TM: Assessment of Ultrasonic Computed Tomography in Symptomatic Breast Patients by Discriminant Analysis, Ult. in Med. Biol., 15, 21-28, 1989.

Shah SM., "An Algorithm for the Quantitative Analysis of Mammographic Breast Density", Master Thesis, Rackham School of Graduate Studies, Department of Nuclear Engineering and Radiological Sciences, University of Michigan, Ann Arbor, 1998.

Sickles EA: Mammographic features of 300 consecutive nonpalpable breast cancers. AJR 146:661-663, 1986.

Snyder HL: Chapter 3: The Visual System: Capabilities and Limitations. In: *Flat-Panel Display and CRTs*. Ed. Tannas LE Jr, Van Nostrand Reinhold, New York, 1985.

Wallis MG, Walsh MT, Lee JR: A review of false negative mammography in a symptomatic population. Clinical Radiology 44: 13-15, 1991.

Wu X, Barnes GT, Tucker DM. Spectral dependence of glandular tissue dose in screen-film mammography. Radiology 1991; 179:143-148.

(11) Appendix

Reprints of the four following journal articles are enclosed:

1. Liu B, Goodsitt MM, Chan HP. Normalized average glandular dose in magnification mammography. Radiology. 1995; 197:27-32.

2. Goodsitt MM, Chan HP, Liu B. Investigation of the line-pair pattern method for evaluating mammographic focal spot performance. Medical Physics 1997; 24: 11-15.

3. Goodsitt MM, Chan HP, Liu B, Morton AR, Guru SV, Keshavmurthy S, Petrick N. Classification of compressed breast shape for the design of equalization filters in mammography. Medical Physics 25: 937-948, 1998.

4. Keshavmurthy SP, Goodsitt MM, Chan HP, Helvie MA. Design and evaluation of an external filter technique for exposure equalization in mammography. Medical Physics 1999; 26: 1655-1669.

(12) Personnel supported by the research grant

Heang-Ping Chan, Ph.D.	PI
Mitchell M. Goodsitt, Ph.D.	Co-PI
Mark A. Helvie, M.D.	Co-investigator (Radiologist)
Dorit D. Adler, M.D.	Co-investigator (Radiologist)
Shankar Guru, Ph.D.	Postdoctoral Research Fellow
Shyam Keshavmurthy, Ph.D.	Postdoctoral Research Fellow

Q. Diagnostic: Mammography II *(Room A9)*

Q1 Evaluation of mammography shielding with aluminum oxide TLDs
R.P. Lieto, D.J. Peck,* Henry Ford Hospital, Detroit, MI 48202, L. Hefner, Wm. Beaumont Hospital, Royal Oak, MI 48073

Current shielding design follows NCRP Report 49 to estimate barrier thicknesses required for diagnostic x-ray rooms. Several limitations exist in applying this report to mammography facilities. The limitations involve the low operating energies (≤35 kVp) and equipment design. The purpose of this study was to compare calculations obtained with NCRP 49 with actual exposure measurements. This evaluation addressed compliance with new NCRP Report 116 recommendation to limit continuous exposure of the general public to 1 mSv/yr and occupational exposures to 10 mSv/yr. Aluminum oxide TLDs were chosen to measure the exposures because of their low minimum detectable dose. The TLDs could quantitate levels as low as 0.0003 mSv. The TLDs were placed on the walls and operator's barriers at three separate urban mammography facilities for 5-8 weeks. Workload data, from the number of exposures and average technique recorded for each machine, was input for NCRP 49 methodology to estimate shielding requirements. Actual exposure measurements were used to calculate shielding requirements based on the transmission data for Mo target tubes. Weekly room workloads were higher than quoted by AAPM Task Group #9. Average room dose measurements at the barriers were 0.005-0.349 mSv/week. Results demonstrated that NCRP 49 methodology overestimates shielding >7X for the room walls and >12X for the operator's barrier. Because shielding estimates based on NCRP 49 are significantly conservative, previous mammography room designs meet the lower dose limit recommendations of NCRP 116.

Q2 Normalized Average Glandular Doses in Magnification Mammography
R. Liu*, M. M. Goodsitt, H-P Chan, University of Michigan, Ann Arbor, MI 48109

We performed a Monte Carlo calculation to determine the rad/Roentgen ratios for magnification mammography. The methodology was similar to that of Wu et al. [Radiology 1991;179:143-148] for contact mammography. In general, the normalized mean glandular dose for mammography depends upon kVp, HVL, breast thickness, and breast composition. For the magnification technique, two additional parameters are also important - magnification factor and field size. The effect of the breast being closer to the focal spot is a slight reduction in percentage depth dose, and because only part of the breast is exposed, there is a reduced scatter contribution to the average glandular dose. Our calculations show that rad/R ratios for magnification mammography are about 10-30% lower than those for contact mammography. The majority of this difference results from reduced scatter due to partial irradiation of the breast volume. Thus, our results indicate that the glandular dose will be overestimated if the rad/R ratios for contact mammography are used for magnification mammography. Finally, it should be noted that although the rad/R ratios are smaller for magnification mammography, the average glandular doses can be up to a factor of 2 greater due to the increased exposures associated with the smaller source to skin distance.

Q3
TLD Measurements of *In-Vivo* Mammographic Exposures and the Calculated Mean Glandular Dose in the United States
J.R. Gentry and L.A. DeWerd, University of Wisconsin-Madison, 1530 Medical Sciences Center, 1300 University Avenue, Madison WI 53706

The exposures measured by TLDs placed on the breasts of over 4400 women at 176 institutions across the United States are presented. Breast thickness and other important parameters are examined for their effect on exposure and mean glandular dose. A linear relationship between breast size and exposure was found. Mean glandular dose was found to increase with breast thickness. Results showed that while the average mean glandular dose delivered by the institutions was well below the limit of 300 millirads (3.0 mGy) set by the American College of Radiology, a number of exams exceeded this value. Breasts of 5.0-8.0 cm thickness were twice as likely to have received a mean glandular dose exceeding 300 millirads. Ten percent of all women received a mean glandular dose exceeding 300 millirads (3.0 mGy). Of institutions delivering 5 or more doses exceeding 300 millirads (3.0 mGy), almost 25% were to breasts of 4.5 cm thickness.

Q4 Calculated Mammography X-Ray Spectra and Measured Beam Parameters
Robert G Waggener*, William H Payne, and Melissa Miller. The University of Texas Health Science Center, San Antonio, TX 78284-7800.

A program was written to calculate mammography x-ray spectra for Mo, Rh and W targets with either Al, Mo, or Rh filters. Input parameters include target material, target angle, tube tilt angle, voltage wave form, tube filtration material and thickness, and added filter thickness and material. Spectra were calculated and compared to measured beam parameters such as kVp, mR/mAs at a given distance, hvl and homogeneity coefficients. The program was used to calculate x-ray spectra for some 70 mammography units with the majority ACR accredited. Good agreement between the calculated x-ray spectra parameters and measured parameters was found for approximately 25% of the units at the first calculation. By adjusting program parameters, we were able to obtain calculated results that agreed with the measured beam parameters. The main discrepancy appears to be nominal and actual kVp and assumed and actual position of hvl measurement. Results of the calculations and measurements will be presented.

Q5 Mammographic Dose and Contrast As A Function of Anode and Filter Material,
D.R. Jacobson*, Medical College of Wisconsin, Milwaukee, Wisconsin 53226

The contrast and dose characteristics of mammography using new combinations of anode and filter materials has been assessed. Standard half-value layer measurements were performed and contrast was measured using tissue-equivalent gel/oil phantoms. Measurements were obtained using moly/moly, moly/rhodium, moly/aluminum, rhodium/rhodium, and rhodium/aluminum at a range of kVp's between 24 and 32. Average glandular dose was calculated for moly/moly and estimated for other anode/filter combinations. Over the range of kVp and anode filter combinations used, the average x-ray energy varied between about 14.5 and 19.1 keV (HVL 0.30 - 0.66). Simulated gland/adipose contrast (difference in OD) varied by over 50%. For a given anode/filter combination, increasing kVp resulted in decreasing contrast. However, this was not always true when the anode/filter combination was changed.

which is sufficient to perform 3-D morphologic analysis. Biopsy specimens and *in vivo* calcifications have been examined. In instances where calcifications are associated with a mass, we can distinguish preferentially peripherally distributed calcifications (predominantly benign) from homogeneously distributed calcifications (predominantly malignant). We have also been able to elucidate the ductal distribution of some malignant calcification clusters. In a preliminary ROC study involving 3 radiologists and 27 lesions (5 malignant), the specificity increased when 3-D images were included in the diagnostic evaluation, resulting in an increase of A_z from 0.66 to 0.87 ($p<0.005$).

WE-C4-04

COMPENSATION FOR PATIENT MOTION IN STEREOTACTIC MAMMOGRAPHY, M. Albert and A. D. A. Maidment, Thomas Jefferson University, Philadelphia, PA.

We have developed a method for performing the three dimensional (3-D) reconstruction of microcalcifications from a limited number of digital mammograms (1k × 1k × 12 bits, 48 μm pixels). The projections of a calcification in any two views, in principle, allow for the reconstruction of the true 3-D position. The pairing of calcifications between views is greatly aided by the fact that the projection of a calcification in one view determines a line along which the projection must lie in the other view. In practice this is confounded by possible non-rigid motions of the breast between exposures, which can affect the reconstructed positions and reduces the fraction of calcifications which can be paired. To correct for patient motion we use the calcifications which are readily identifiable between views to estimate an affine transformation which approximates this motion. This then aids in matching the remaining calcifications and in reconstructing their positions. In preliminary work on data from 27 cases, the distance between the observed shadows of calcifications and the computed projections of the fitted spatial positions decreases from an average RMS value of 240 μm to 50 μm. The additional degrees of freedom introduced by patient motion result in the geometric positions being underdetermined in a manner which will be discussed.

WE-C4-05

TOMOSYNTHESIS FOR BREAST IMAGING, L.T. Niklason[1], B.T. Christian[1], L.E. Niklason[1], D.B. Kopans[1], H.M. Rougeot[2], B.H. Opsahl-Ong[2], D.E. Castleberry[2], [1]Harvard University and [2]General Electric Co. A new method for tomosynthesis of the breast is described and evaluated. This method is based on using a flat-field digital detector and a conventional compression system. The breast and detector remain stationary while the tube is moved in an arc above the breast. This method is easily adaptable to many mammography systems without complex mechanical changes. Images are acquired by making a series of short low-dose x-ray exposures at fixed x-ray tube positions along an arc. The obtained images must be warped prior to reconstructing the tomosynthesis images. The warping algorithms will be described which allow reconstruction of any tomographic image plane. We will present phantom images and evaluate the tomographic angle and the number of images required for adequate blurring. Breast tomosynthesis imaging may have a major impact on the visibility of breast lesions by blurring structures above and below a lesion. Better visualization of lesions and lesion borders may increase the specificity of mammography and reduce the number of benign biopsies. The sensitivity of mammography may also be improved by using tomosynthesis on radiographically dense breasts.

WE-C4-06

DIGITAL ANGIOGRAPHY OF THE BREAST
K.D. Carumbaya, M. Albert and A.D.A. Maidment, Department of Radiology, Thomas Jefferson University, Philadelphia, PA.

Conventional mammography provides high resolution images of breast lesions, but fails to characterize the associated vasculature. Previous investigators have shown that there is a clear correlation between extent of tumor vasculature and degree of malignancy. In clinical angiographic studies, malignant breast lesions have been characterized by the presence of a "blush" (i.e., contrast media concentrated in a diffuse pattern). An energy transport model has been developed to simulate digital angiography of the breast and to aid in the development of a dedicated breast angiographic imaging system. The model considers x-ray tube target material and kilovoltage, beam filtration, detector type, scattered radiation, breast composition, lesion size, and the differential iodinated contrast agent (ICA) uptake by the lesion and surrounding normal tissue. We use the lesion signal-to-noise ratio per square root of dose as an image quality index (IQI), which allows one to determine the smallest contrast agent dose and radiation dose that may be used while still ensuring reliable characterization of angiographic and mammographic findings. Preliminary results indicate that detection of lesions with ICA concentrations <30 mg/cm^3 is optimum at 25 to 30 kVp (1 mm Al filtration). Higher ICA concentrations are optimally imaged at higher kilovoltages. Increased beam filtration will result in increased IQI, but may be impractical due to x-ray tube load limitations.

WE-C4-07

A NEW BREAST TUMOR IMAGING APPROACH USING SPECT SYSTEMS WITH NON-TILTABLE CAMERAS: A PHANTOM STUDY, H. Wang, C. Scarfone, R.J. Jaszczak, R.E. Coleman, Duke University Medical Center. A SPECT approach to breast imaging is proposed which requires that (1) the camera's axis of rotation is perpendicular to patient's craniocaudal orientation, (2) the field-of-view is extended to the edge of the camera at the patient side, and (3) each breast is imaged independently. This approach has the advantages of (1) the breast being imaged is positioned near the axis-of-rotation allowing a small radius-of-rotation, (2) a small volume of attenuating medium, (3) 360° data acquisition, and (4) the reduction of detected photons from the opposing breast. The proposed approach was evaluated using a triple-headed SPECT system with parallel-hole collimators and was compared to planar scintimammography with the same collimators. The anthropomorphic thorax phantom used for the study contains fillable liver, lung, heart, breast attachments with lesion inserts. The Tc-99m concentrations in various parts of the phantom simulated a clinical biodistribution of a 25-mCi sestamibi intravenous injection and a lesion-to-background concentration ratio of 20:1. The background concentration ratio is 0.2 μCi/ml. The lesion with a diameter of 1.2 cm was placed at the half-distance position between the nipple and the chest wall. The same acquisition time (15 and 30 minutes) was used for both SPECT and planar scintimammography. A total of 120 projections (pixel size: 1.76 mm) were acquired at equally spaced angular views over 360° for SPECT. The projections were reconstructed using a filtered backprojection algorithm with pre-smoothing using the Hann filter at 0.5-Nyquist frequency. The results show that the contrast between lesion and breast background in SPECT reconstructed images is three-to-five times the contrast in scintimammograms. This marked improvement in lesion contrast over scintimammography demonstrates the potential of the proposed SPECT approach for breast imaging.

WE-C4-08

AUTOMATED MODEL-GUIDED BREAST SEGMENTATION ALGORITHM A. R. Morton, H. P. Chan, M.M. Goodsitt, University of Michigan, Ann Arbor, MI.
We have developed a fully automated breast border detection program for segmentation of the breast region from digitized mammograms.

The program first trims the unexposed area and labels from the image, and then finds the breast border within the exposed area. Our edge detection algorithm uses a model-guided two-pass approach. In the first pass, a simple edge detection routine uses the first and second derivatives to locate the approximate edge coordinates for each line. In the second pass, an edge tracking algorithm uses an adaptive threshold criterion to determine the accurate breast boundary using the approximate edge as a guide. Starting from about the nipple of the breast image and tracking in both directions, the program estimates the local mean gray level just outside the breast border and then searches for an edge point that passes a second derivative and a threshold criteria within a local region centered at the approximate edge. For subsequent edge points, the edge tracking routine uses previously found edge points to adjust the search direction and define the search region for the breast border. Using a data set of over 1000 mammograms, we found that the edge tracking routine can accurately detect the breast borders in over 98% of the images. This model-guided search method reduces the likelihood that the edge tracking routine will be misled by noisy background fluctuations. To quantify the accuracy of the algorithm, we compared the detected breast border with a manually traced 'true' breast border for a small set of randomly selected images. The average root-mean-square difference was 1.4 mm (corresponding to 1.4 pixels). The breast segmentation algorithm will be useful for both the design of x-ray equalization filters for mammography and for computerized analysis of mammograms.

WE-C4-09

COMPRESSED BREAST SHAPE CLASSIFICATION FOR THE DESIGN OF MAMMOGRAPHY EQUALIZATION FILTERS M.M. Goodsitt, H-P Chan, B. Liu, S. Guru, R. Morton, University of Michigan, Ann Arbor, MI.

We are developing an external filter method for equalizing the mammographic x-ray exposure in the peripheral region of the breast. To be practical, it will be necessary to employ only a finite number of custom built filters. Our previous work has shown that most compressed breast shapes can be fit by the equation $y=ax^2+bx^3$, and can be classified by the a and b coefficients. In this study, we compared the goodness of classification obtained with the above coefficients and those for the fourth order polynomial $y=ax^2+bx^3+cx^4$. Classification was performed using the K-Means Cluster Analysis procedure in the SPSS statistical package, which is based on nearest centroid sorting. In the preliminary work of this study, an automated border trace algorithm was employed to determine the breast borders in 191 CC-view mammograms. These borders were fit with the above equations, and were clustered into 4 to 10 classes according to their a,b and a,b,c coefficients. For each class, an average "filter" border was determined using the average coefficients for the borders in that class. Individual borders were then translated and rotated to best match the filter border. Average rms errors between the individual borders of a given class and the "filter" borders were computed. Although the fits to the original borders were superior for the 3-coefficient equation (rms errors in many cases were better by a factor of 2), the matches to the "filter" borders determined by clustering were not improved. Results for about 500 CC-borders and 500 MLO borders will be presented at the meeting. If the results for the larger data set concur, a two tier approach will be examined in which classification is achieved using 2-coefficients for most borders and 3 when the rms error of the original fit is greater than a threshold value.

WE-C4-10

PHYSICAL MEASURES OF IMAGE QUALITY IN MAMMOGRAPHY: APPLICATION TO DIGITALLY ACQUIRED IMAGES, D. P. Chakraborty, E. L. Gingold, X.M. Zhao, University of Pennsylvania Medical Center.

A method for quantitative analysis of images of the American College of Radiology (ACR) mammography accreditation phantom has been applied to make measurements of the image quality of directly acquired digital images. Images of an ACR phantom were acquired under various conditions of kVp and mAs using a Fischer MammoTest Biopsy unit. Also acquired were 22 kVp images of the ACR phantom wax insert under conditions of similar magnification. The images were analyzed using our published methodology to yield indices that quantified the image quality of the imaging system precisely and objectively. Because of the limited field-size, for this study we centered all images on the first two microcalcification groups only, and all indices were averaged over the 12 specks in these groups. We demonstrate the measured dependence of the pixel values scale factor, correlation and noise indices on kVp, in the range 22 to 35 with phototimed mAs, and on mAs, in the range 10 to 300 at 26 kVp manual techniques. Because a digital detector is linear, some of the measures introduced earlier have a simple dependence on mAs. The noise measure was linear when plotted as a function of the square root of mAs at constant kVp. Also, the pixel values scale factor measure was linear when plotted as a function of mAs at constant kVp.

WE-C4-11

CONTRAST-DETAIL CURVES IN AN ANTHROPOMORPHIC BREAST PHANTOM WITH A DIGITAL MAMMOGRAPHY SYSTEM, G. Qu, W. Huda*, B.G. Steinbach, J.C. Honeyman, University of Florida, Gainesville, FL 32610

Digital mammography may offer improved lesion detection from modifications to the radiographic technique factors such as kVp and mAs. In this study, the contrast-detail performance of a LoRad Digital Spot Mammography system was compared with a Kodak Min R screen-film combination. An anthropomorphic phantom was used to simulate realistic mammography conditions. The contrast-detail phantom contained holes from 7 mm to 0.3 mm in diameter with a thickness from 1 mm to 0.06 mm acrylic. Screen-film radiographs were obtained using a GE 60OT mammography unit. Using the screen-film combination, the kVp and mAs could only be varied over a narrow range whilst still maintaining a satisfactory optical density. The digital detector, however, had a linear response up to about 100 mR and permitted a wider latitude in selecting radiographic techniques. The results obtained showed that the performance of the screen-film system was only optimal over a narrow range of radiation exposures with a relatively minor dependence on the selected kVp. The wide latitude of the digital detector resulted in a superior performance when compared to a screen-film system and showed a maximum performance at the highest radiation exposures.

WE-C4-12

SELECTION OF BEAM FILTERS IN DIGITAL MAMMOGRAPHY FOR TUNGSTEN-TARGET X-RAY TUBES. M.P. André, B.A. Spivey, J.M. Tran, University of California and Department of Veterans Affairs, San Diego, CA.

Tungsten (W) target x-rays tubes are being studied for use in digital mammography to improve x-ray flux, reduce noise and increase tube heat capacity. A parametric model was developed to compute spectra for combinations of beam filters, kVp, breast type and thickness (30-75 mm). Contrast/noise ratio and spectral quantum efficiency were computed for these combinations to evaluate performance of filtered spectra for each breast type. The model is derived from a combination of classic equations, XCOM from NBS, and published data. X-ray spectra were calculated and

experimental, daily QA during clinical trials is necessary. Since analyzing results from each module is time consuming, an analysis program to find the objects in the phantom and automatically score the image is being developed. The phantom configuration will be redesigned for each manufacturer's prototype unit, but each component will remain the same. After testing for 6 months, factors which do not predict equipment failure will be deleted from the phantom.

WE-C1-05

DESIGN OF EXPOSURE EQUALIZATION FILTERS FOR MAMMOGRAPHY

S. P. Keshavmurthy, H. P. Chan and M. M. Goodsitt, University of Michigan, Ann Arbor, MI.

We are developing an x-ray equalization filter technique for mammography. Our approach is to pre-fabricate a small number of shaped filters based on analysis of compressed breast shapes, and to use a digitized video image of the compressed breast to find the best-matched filter for a specific patient. In our previous study, we digitized over 1000 randomly selected mammograms and classified the breast shapes in CC and MLO-view into 4 and 6 groups, respectively. The classification was based upon the a and b coefficients of $y=ax^2+bx^3$ polynomial fits to the detected breast borders. In this study, we analyzed the exposure profiles along normals to the average breast border for each group. A Monte Carlo simulation using the MCNP code was conducted to obtain the scatter fraction along a normal to the breast border. The scatter fraction calculated using MCNP was compared with experimental results measured by a beam stop method. The MCNP predicted scatter component was subtracted from the exposure profiles to obtain an average primary exposure profile for each class. Filter thickness profiles for various potential filter materials were calculated. A simulation study was performed in which a best-matched filter was used to attenuate the calculated primary exposure profiles from randomly selected digitized mammograms classified to belong to a particular group. The exposure dynamic ranges of these "exposure-equalized" breast images were analyzed and compared with those of the unequalized images. The need to design several filter thicknesses for a given breast-shape group to accommodate breasts that have different thicknesses and compositions was evaluated. Using some of the selected filter materials, filters were fabricated and tested on CIRS breast phantoms. The effects of the equalization filters will be demonstrated with the CIRS phantom images.

WE-C1-06

APPLICATION OF A HIGH RESOLUTION SMALL GAMMA CAMERA TO SCINTIMAMMOGRAPHY : MEASUREMENTS AND SIMULATIONS, D.Steinbach, S.Majewski, M.Williams, B.Kross, A.Weisenberger and R.Wojcik, Thomas Jefferson National Accelerator Facility. Test results of a small field of view scintimammography camera based on a position sensitive photomultiplier tube (PMT) and a crystal scintillator gamma sensor are presented. A 5" Hamamatsu PMT was coupled to a variety of scintillators, including planar and pixelized NaI(Tl), CsI(Na), and YAP. Laboratory and phantom studies were performed to compare performances of the above scintillator sensors with special emphasis on spatial resolution and scatter rejection. A slant collimator and imaging light guides were tested to eliminate the dead region close to the chest wall.

WE-C1-07

THE DIGITAL FILM VIEWER: A NOVEL FILM READING TECHNOLOGY, D. Inbar, H. Wolf, R. Sohval, SmartLight Research Laboratories, Israel. A digital film viewer (DFV) has been developed that significantly improves reading and interpretation of X-Ray films compared to a conventional light box, which typically limits the reader to perceive only a fraction of the information recorded on the film. The DFV uses advanced electro-optical technologies to electronically optimize film reading acuity and to minimize visual fatigue. The DFV incorporates an artificial vision system which identifies each film, analyzes the clinical image recorded on it, and automatically optimizes five key viewing parameters: The DFV (1) adapts the illumination intensity up to 10,000 nits according to film density, so the optimal light level always reaches the observer's eye; (2) electronically masks the image, seamlessly, to completely eliminate glare; (3) adjusts the chromaticity of the illumination, based on film density, to optimize the effects of both cone and rod vision; (4) employs micro-optic beam formers to suppress optical scatter within the film; (5) controls the ambient light level according to reader activity. In addition, the DFV allows the operator to eliminate cognitive distraction and optimize reading of clinically important parts of the image. Preliminary clinical evaluation demonstrates that the DFV improves diagnostic confidence and the ability to detect small lesions. The DFV complies with MQSA and the 1996 European Guidelines on Quality Criteria for Diagnostic Radiographic Image Viewing Conditions.

The research described in this abstract was supported by a grant from the SmartLight Research Laboratories.

WE-C4 Brachytherapy II Calculations and Measurements *(Juneau)*

WE-C4-01

DOSIMETRIC MODELING OF ^{137}C S INTRACAVITARY SOURCES: THE AMERSHAM CDCS J -TYPE SOURCE J. F. Williamson, Washington University School of Medicine, St. Louis, MO 63110.

The Amersham CDCS J-type source is currently the only manually-afterloadable ^{137}Cs intracavitary source commercially available in the U.S. However, a complete 2D dose-rate table is not available for this source. Detailed dose-rate tables have been calculated for this source as well as its predecessor, the 3M model 6500/6D6C source, using a Monte Carlo photon transport code, which has been systematically benchmarked against dose measurements. The root mean-square (RMS) average difference between two resultant dose distributions is 2.6% (-6% to +14% range). In addition, the accuracy of the widely-used 1-D pathlength (Sievert integral) algorithm has been systematically tested against Monte Carlo benchmark calculations. If the filtration coefficients for steel and ceramic media are approximated by linear energy absorption coefficients, the RMS accuracy achieved is 2.4% to 2.8% (error range of -1.4% to 7.6%). Treating the filtration coefficients as parameters of best fit, selected so as to minimize the differences between 1-D pathlength and Monte Carlo calculations, the RMS error is reduced to 0.8% (error range of -1.8% to 4.1%). The optimal filtration coefficient values for stainless steel and low-density ceramic matrix are nearly independent of source geometry. The accuracy of Sievert algorithm implementations commonly found on commercial RTP systems will be presented.

This work was supported in part by Amersham/Medi-physics.

WE-C4-02

MEASUREMENT OF DOSE DELIVERED BY AMERSHAM J TYPE CESIUM SOURCES, R. J. Baker, Walter Grant III, David Belleza, David Ballinger, Baylor College of Medicine, Houston Texas.

Historically, intracavitary brachytherapy has employed cesium tubes manufactured by the 3M Corporation, but such sources

685 • 11:24 AM

Evaluation of X-ray Detectors for Digital Mammography-Monte Carlo Simulation Study

S.P. Keshavmurthy, PhD, Ann Arbor, MI • H. Chan, PhD • M.M. Goodsitt, PhD

PURPOSE: To compare the performance of several potential x-ray detectors for digital mammography.

MATERIALS AND METHODS: A simulation model of a mammography system has been developed using Monte Carlo (MC) analysis. This model includes photon transport in the breast and the grid, and x-ray absorption in the detector. Electron and light photon transport in the detector are not considered. The MC code MCNP developed by Los Alamos laboratories is used. In this study, spectra between 26 and 40 kVp from a Mo target with Mo and Rh filters were analytically generated and the next-event estimator of MCNP was used to calculate detector energy deposition. Potential x-ray detectors including CsI (50 m m), Se (150 m m), Gd_2O_2S (100 m m), Pb_2I (50 m m), and CdTe (50 m m) were studied. A 100- m m-thick cylinder of calcium hydroxyapatite was modeled as a contrasting calcification. The incident exposure, mean glandular dose, scatter fraction, contrast, and quantum noise in the detector were calculated from MCNP simulation results. A figure-of-merit (FOM) that represented the tradeoff between the SNR and the dose was used to estimate the optimal imaging energy.

RESULTS: The MC predicted contrast and the scatter fractions were in good agreement with published and measured results. For a 5-cm 50% glandular and 50% adipose breast we obtained the following

RESULTS: 1) the optimal kVp with Mo/Mo spectra was 32 kVp for CsI, 30 kVp for Gd_2O_2S, Pb_2I, CdTe, and 29 kVp for Se, 2) the optimal kVp for Mo/Rh spectra was 28 kVp for CdTe and close to 30 kVp for all other detectors, 3) CsI showed slightly higher SNR than all other detectors for both Mo/Mo and Mo/Rh spectra, 4) the quantum noise for CsI and CdTe was slightly higher at energies above 35 kVp. Studies are being conducted to estimate the optimal kVp with W spectra .

CONCLUSION: Under the conditions studied, the optimal spectra for the detectors range from 28 to 32 kVp.

Learning Objectives:

1) To understand the effect of detector response on image SNR and to determine the optimal spectrum for the different x-ray detectors. 2) To compare the imaging properties of different x-ray detection materials. 3) To study photon transport in a mammography system with Monte Carlo simulation.

686 • 11:33 AM

A Novel Screen-film Combination For Breast Cancer Screening of Women with Dense Breasts

Z. Jing • J.K. Walker, PhD, Gainesville, FL

PURPOSE: To investigate the potential imaging performance of a novel screen-film combination for breast cancer screening of women with dense breasts.

METHODS AND MATERIAL: A new phosphor screen was made of Gd2O2S:Tb phosphor coated on a layer of transparent backing material so that light are emitted from both side of the screen. This screen (screen #1) and a conventional mammography film (film #1, Kodak Min-R E) were loaded in a cassette in their relative positions as those in a modern mammography cassette. A new dual screen-dual film combination was formed by further loading a second screen (screen #2, Kodak Min-R medium) and a double emulsion film (film #2) so that this double emulsion film was sandwiched between the transparent backing side of screen #1 and the phosphor side of screen #2. This new screen-film combination produces two images of the same compressed breast from a single exposure. The image on film #1 resembles a conventional mammogram that can be produced from a modern mammography screen-film combination. The effective speed of film #2 is faster than that of film #1. Thus, some dense breast regions that would otherwise be underexposed on film #1 could be properly exposed and displayed with high film contrast on film #2. Spatial resolution performance of film #2 is investigated by taking images of a star resolution pattern. Optimal separation in the two films_ effective speeds was investigated. The speed requirement for film #2 was then determined by measuring relative light emissions from the phosphor and backing side of the screen(s). Potential improvements in the detection of breast lesions were investigated using an ACR accreditation phantom and an anthropomorphic breast phantom.

RESULTS: A limiting spatial resolution of ~10 lp/mm was observed on film #2. It was found that a factor of two separation in the two films_ effective speeds could provide an adequate exposure latitude for imaging of dense breasts. This can be achieved by the use of a film #2 with speed about a factor of 2.5 times faster than film #1. Phantom studies showed significant improvement in the detection of simulated breast lesions in the simulated dense regions of the phantoms.

CONCLUSION: The method overcomes one major technical problem of screen-film mammography.

Learning Objectives:

1. Improve breast cancer detection in women with radiographically dense breasts.
2. Study the necessary exposure latitude of screen-film mammography systems for imaging of dense breasts
3. Investigate a method to increase the exposure latitude of screen-film mammography systems without sacrificing film contrast.

687 • 11:42 AM

The Sensitivity and Specificity of Mammographic Image Quality Tests: A Comparison of the ACR Method and the Mammography System Test

B.M. Galkin, MS • A.D. Maidment, PhD, Philadelphia, PA • F.P. Moyer, BSRT

PURPOSE: A method for changing the currently used ACR phantom image test into a more comprehensive Mammography System Test has been previously described*. The purpose of this report is to summarize the results of a comparison study of both methods using different mammography units, target filter combinations, and imaging systems.

MATERIALS AND METHODS: The ACR test consists of comparing serial radiographs of an approved breast phantom and a superimposed plastic disc, to determine if there has been a change in the number of test objects seen, or a change in optical density that exceeds prescribed control limits for the phantom background, disc, or contrast. The Mammography System Test uses optical density measurements of films containing multiple images the same breast phantom a mammography beam quality phantom*, and a sensitometric pattern. The same control criteria were used for both methods.

RESULTS: Unlike the ACR test, the Mammography System Test is able to detect changes as small as ± 1 kVp, ± 5% in phototimer response, and ± 0.01 mm Al HVL. It can also identify whether the cause for image change is due to the processor or mammography unit.

CONCLUSION: The Mammography System Test provides a greater degree of image quality control than the ACR method.

* Galkin BM, U.S. Patents 5,063,583; 5,276,726; 5,406,612; 5,544,238; other patents pending.

Learning Objectives:

Describe a Mammography System Test film and explain how it differs from an ACR image quality test film. Describe the advantages of the Mammography System Test over the ACR test in monitoring mammographic image quality.

688 • 11:51 AM

The Value of Biphasic Breast Compression for Craniocaudal and Mediolateral Oblique Projections in X-ray Mammography

F. Zandrino, MD, Genova, Italy • E. Bonaldo, MD • A. Imperiale, MD • E. Bertoli, MD • R.C. Parodi, MD • F. Sardanelli, MD

PURPOSE: To evaluate the value of biphasic compression (BC) in X-ray mammography.

METHODS AND MATERIALS: 40 women (aged 55.1 ± 10.3) underwent two craniocaudal (CC) projections of right (29) or left (11) breast,one with standard monophasic compression (MC),the other with BC (a first compression phase with a 22.5° angled plate,followed by progressive angle reduction). Other 40 women (aged 50.2 ± 10.8) underwent two 45° oblique (OBL) projections of right (24) or left (16) breast, one with standard MC, the other with BC. Mammographic unit:Sophie (Planmed). For CC projection,we considered evidence of pectoral muscle (McNemar test), maximal distance (A) between the cutaneous profile and the posterior border of the film (paired T test). For OBL projection, we considered the distance (B) between nipple projection and the pectoral muscle along the posterior border of the film (paired T test). For both projections, a blinded subjective evaluation was performed, choosing which of the two mammograms showed the better image quality or to judge the two modalities equivalent (McNemar test).

RESULTS: CC projection: pectoral muscle was detected in 11 BC and in 4 MC mammograms ($p=0.016$); A ranged 4.9-14.5 cm (9.8±2.2) for BC versus 4.7-14.5 cm (9.5±2.2) for MC, in 34/40 women A being longer with BC than with MC, in 3 patients equal for both modalities, in 3 longer with MC than with BC ($p<0.001$); at subjective evaluation,36/40 BC produced better (30) or equivalent (6) results compared with MC ($p<0.001$). OBL projection: B ranged 0-7.2 cm (3.08±1.74) for BC versus 0-7.0 cm (3.25±1.57) for MC (no significance); at subjective evaluation, 34/40 BC produced better (16) or equivalent (18) results compared with MC (no significance) but if the 34 better or equivalent results are grouped, statistical significance is reached ($p=0.018$). BC did not cause any complaint by the patients; no more time consuming than MC.

CONCLUSION: BC seems to be a promising technical improvement for X-ray mammography.

Learning Objectives:

To describe a new biphasic procedure for breast compression in X-ray mammography.

To demonstrate that biphasic compression allows us to study more breast with higher image quality in craniocaudal projection.

To suggest that some advantages are possible for biphasic compression also in oblique projection.

To remark that biphasic compression is well tolerated by the woman and seems to be no more time consuming than monophasic compression.

Tuesday

Classification of compressed breast shapes for the design of equalization filters in x-ray mammography

Mitchell M. Goodsitt,[a] Heang-Ping Chan, Bob Liu,[b] Shankar V. Guru,[c] A. Ray Morton,[d] Shyam Keshavmurthy, and Nick Petrick
Department of Radiology, University of Michigan Hospital, Ann Arbor, Michigan 48109

(Received 28 May 1997; accepted for publication 17 March 1998)

We are developing an external filter method for equalizing the x-ray exposure in mammography. Each filter is specially designed to match the shape of the compressed breast border and to preferentially attenuate the x-ray beam in the peripheral region of the breast. To be practical, this method should require the use of only a limited number of custom built filters. It is hypothesized that this would be possible if compressed breasts can be classified into a finite number of shapes. A study was performed to determine the number of shapes. Based on the parabolic appearances of the outer borders of compressed breasts in mammograms, the borders were fit with the polynomial equations $y=ax^2+bx^3$ and $y=ax^2+bx^3+cx^4$. The goodness-of-fit of these equations was compared. The a,b and a,b,c coefficients were employed in a K-Means clustering procedure to classify 470 CC-view and 484 MLO-view borders into 2–10 clusters. The mean coefficients of the borders within a given cluster defined the "filter" shape, and the individual borders were translated and rotated to best match that filter shape. The average rms differences between the individual borders and the "filter" were computed as were the standard deviations of those differences. The optimally shifted and rotated borders were refit with the above polynomial equations, and plotted for visual evaluation of clustering success. Both polynomial fits were adequate with rms errors of about 2 mm for the 2-coefficient equation, and about 1 mm for the 3-coefficient equation. Although the fits to the original borders were superior for the 3-coefficient equation, the matches to the "filter" borders determined by clustering were not significantly improved. A variety of modified clustering methods were developed and utilized, but none produced major improvements in clustering. Results indicate that 3 or 4 filter shapes may be adequate for each mammographic projection (CC- and MLO-view). To account for the wide variations in exposures observed at the peripheral regions of breasts classified to be of a particular shape, it may be necessary to employ different filters for thin, medium and thick breasts. Even with this added requirement, it should be possible to use a small number of filters as desired.
[S0094-2405(98)00106-0]

Key words: mammography, equalization, classification, filtration

I. INTRODUCTION

Mammographic abnormalities related to early breast cancers include clustered microcalcifications, spiculated and irregular masses, areas of parenchymal distortion, and skin thickening.[1,2] These abnormalities are often subtle and low contrast. Therefore, low-energy radiation and high-contrast screen/film systems are recommended for mammographic imaging in order to increase the contrast between the lesion and the background tissue. Despite the use of vigorous compression during examinations,[3] the low-energy x-ray beam results in a wide dynamic range (the ratio of the maximum to the minimum x-ray exposure at the detector) for the radiation penetrating the breast. This range can be greater than 100.[4] On the other hand, high-contrast film provides a narrow latitude which is about 10 for a typical mammographic system.[5,6] As a result, thick and glandular regions of the breast are often imaged at the toe of the sigmoid-shaped sensitometric curve of the screen/film system; whereas thin peripheral regions are imaged at the shoulder. The contrast and signal-to-noise ratio (SNR) of mammographic features are greatly reduced in these regions due to decreased film gradient. The contrast sensitivity of the human visual system also drops rapidly as the film density increases.[7–9] Kopans[10] found that 70% of breast cancers in women with dense breasts are in the periphery of the mammary parenchyma adjacent to the subcutaneous fat or retromammary fat. The poor image quality in the peripheral region thus imposes a serious limitation on the sensitivity of cancer detection in breasts with dense fibroglandular tissue.

A variety of exposure equalization methods have been proposed to improve mammographic imaging. In one, either a water bag[11–13] or a solid, elastic, unit density x-ray attenuator[14] is placed between the breast and the compression paddle to make the total breast thickness uniform all the way out to the periphery. This gap-filling method has the advantage of being patient specific. However, it can be difficult to implement, especially for oblique views. Another, more sophisticated method involves scanning of the breast

with either single or multiple x-ray beams that are intensity modulated based on x-ray transmission signals obtained from single or multiple detectors.[15,16] Such a method can equalize the exposure throughout the breast rather than just at the periphery. However, the method is complex and requires much greater heat loading of the x-ray tube than conventional mammography. Recently, a rotary scanning equalization method has been developed that reduces, but does not eliminate the heat loading and complexity issues.[17]

We have proposed a practical and cost-effective exposure equalization method for reducing the dynamic range of the mammograms. The method employs a set of x-ray beam intensity shaping filters that are positioned near the collimator of the mammography system. Each filter is designed to match the shape of the compressed breast border and to preferentially reduce the exposure to the detector in the peripheral region of the breast. It is our hypothesis that compressed breasts can be classified into a finite number of shapes, and therefore only a finite number of filters will be needed. In this paper, we report on the results of a study we conducted to determine the validity of our hypothesis.

II. METHODS

A. Border detection and modeling

1004 clinical mammograms including both craniocaudal (CC) and mediolateral oblique (MLO) views were digitized with a DBA Systems, Inc. (Melbourne, Florida) model ImageClear M2100 film digitizer. This system has 21 micron resolution, which is much finer than is required for our application. We operated the digitizer in a mode whereby two of every three pixels is skipped, yielding an effective resolution of 63 microns. The resolution was further reduced to 1 mm by averaging the pixel values in 1 mm areas. The light transmission through the films was digitized in 16-bit linear format, and these values were later converted to 12-bit logarithmic format to yield a fairly linear relationship between film optical density and digitized value.

An automated border tracing algorithm was applied to the digitized images.[18] Acceptable borders were obtained in 95% of the mammograms (954 of the 1004), which formed the data set used in our study. The 5% of the mammograms that were excluded exhibited problems such as: (1) a substantial portion of the breast edge extended outside the imaging area of the film; (2) a significant portion of the breast edge was obscured by a patient label; and (3) numerous artifacts (e.g., streaks) were present at the breast periphery caused by the film digitizer. In a separate study, we found the automated border trace routine to be accurate. Comparing the difference between hand-traced and automatically detected borders in a random sample of images, we computed an average root-mean-square difference of 1.4 mm (1.4 pixels).[19] An example of the manually traced and automatically detected borders is shown in Fig. 1.

A total of 470 CC-view and 484 MLO-view automatically traced borders were analyzed in the present study. In reviewing these borders, we observed that the shapes appear to be well characterized by either symmetric or asymmetric polynomials. Therefore, we decided to model the borders with the polynomial equations $y=ax^2+bx^3$ and $y=ax^2+bx^3+cx^4$. These equations have the advantage of producing only two (a,b) or three $(a, b,$ and $c)$ coefficients which can be used in cluster analysis to classify the border shapes.

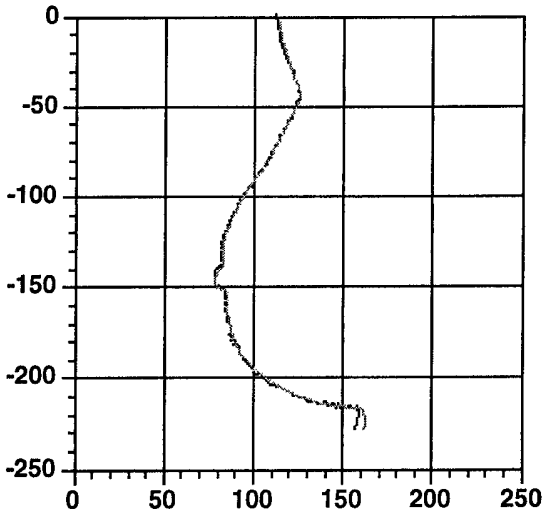

FIG. 1. Example of automatic versus hand-traced compressed breast borders. The hand-traced border is indicated by the lighter gray curve.

B. The border fitting procedure

The fitting procedure involves either translating and rotating the borders about the x- and y-axes or, equivalently, translating and rotating the axes. We wrote custom software to accomplish this task. The method is described below.

First, small irregularities are removed from the borders by applying run-length averaging (run-length employed= 15).

Next, an initial best estimate of the axis positions is made. The approach that was utilized is illustrated in Fig. 2. In brief, it determines the y'-axis by least-square fitting a line

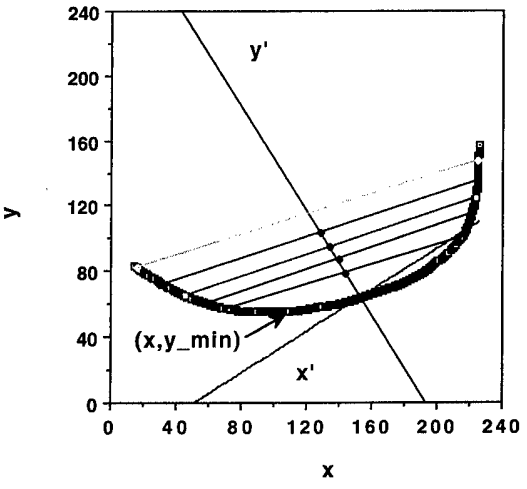

FIG. 2. Example of the x'-y' starting axes computed with the subroutine STARTAXIS. These axes are translated and rotated to find the best fits to the borders using the equations $y'=ax'^2+bx'^3$ and $y'=ax'^2+bx'^3+cx'^4$.

through the midpoints of line segments drawn between appropriate points on the right and left sides of the borders. When suitable line segments are drawn, the border will be fairly symmetric about the line through the midpoints of the line segments, and this line should be a good starting axis for the curve fits.

The algorithm that was written to locate the initial axes, STARTAXIS, first determines the point on the border that has a minimum y-value, (x,y_min). Next, the number of points on the border to the left and right of (x,y_min) are computed. If either number is less than 25, the topmost point on that side is selected as a starting point. Otherwise, the derivatives (dy/dx) of the topmost 25% of the points on each side of (x,y_min) are computed. The point at which the derivative is a minimum (most negative) on the left side of (x,y_min) is selected as a starting point for the left side. Similarly, the point at which the derivative is a maximum (most positive) on the right side is selected as the starting point for the right side. (The topmost, light gray line in Fig. 2 connects the left and right starting points.) Next, the number of points between the left starting point and (x,y_min), and the number of points between the right starting point and (x,y_min) are computed. The smaller of these two numbers is divided by 5 to create an incremental unit. Using the convention that the endpoint of the border on the left is point number 1 and the endpoint on the right is the final point, line segments are determined between points on the border corresponding with the leftmost starting point plus an integer multiple of the incremental unit and the rightmost starting point minus that same value. (See the black lines in Fig. 2) Finally, the midpoint of each line segment is computed.

The y'-axis is then ascertained by least square fitting a line between the midpoints of the line segments. The intersection of this line with the border is defined to be the origin, and the x' axis is the line perpendicular to the y'-axis passing through the origin (see Fig. 2).

C. Determination of best fit by translation and rotation of axes to find the best fit

The next task of the computer program is the translation and rotation of the axes to find the best fit of the polynomial equation to the smoothed border. Equations employed for the translation and rotation were:

$$x' = x_S \cos\theta + y_S \sin\theta$$

and

$$y' = -x_S \sin\theta + y_S \cos\theta,$$

where $x_S = x - x_{\text{origin}} + x_{\text{shift}}$, $y_S = y - y_{\text{origin}} + y_{\text{shift}}$, and $\theta = (\pi/180)\cdot(\theta_{\text{Start}} + \theta_{\text{shift}})$. $(x_{\text{origin}}, y_{\text{origin}})$ and θ_{Start} are the coordinates of the origin and the angle of the starting abscissa (in degrees relative to the x-axis), respectively, and x_{shift}, y_{shift}, and θ_{shift} are the translation and rotation values.

The fit error was defined to be the root-mean-square (rms) distance between corresponding y-values on the smoothed, automatically detected borders and the fitted borders. The equation utilized was

$$\text{error} = \sqrt{\sum_{i=1}^{n} (y_i - y_{\text{fit}_i})^2 / n}.$$

The best fit corresponded to a minimum rms error.

To improve the efficiency of this process, we first employ coarse shifts and rotations with increments of 4 mm and 4 degrees, respectively. We use an x-translation range of $+/-40$ mm, a y-translation range of $+/-20$ mm and rotation angle range of $+/-40$ degrees. The translation shifts (x_{shift}, y_{shift}) and the angle shift (θ_{shift}) corresponding to the best fit are found. After this, finer increments of 1 mm and 1 degree are employed within the best "coarse" shift ranges $+/-4$ mm and $+/-4$ degrees. For each type of fit ($y = ax^2 + bx^3$ and $y = ax^2 + bx^3 + cx^4$), the entire fitting and shifting iteration process takes about $\frac{1}{2}$ second per border on a Digital Equipment Corporation (DEC) AlphaStation. The validity of the above chosen ranges is confirmed by the fact that the fits within these ranges had average rms errors of about 2 mm or less and only in very rare instances (11 cases for CC and 24 for MLO including both a,b and a,b,c fits) did the best fit occur at the limits of translation or rotation. Furthermore, in the majority of the latter cases (e.g., 32 of 35 cases), the fit errors were less than 2.5 mm, which is considered a very good fit.

Finally, to verify that the minima in the rms fit errors were not passed over using coarse followed by fine increments in translation and angulation, the computation was repeated in 229 cases using only fine increments. The resulting rms fit errors were on the average only 0.01 less than those using coarse followed by fine increments, the rms difference between the errors was only 0.02, and the maximum rms difference was 0.13. Thus in general, the minima were not passed over, and greater efficiency was achieved without sacrificing accuracy.

D. Cluster analysis

To classify the border shapes, the resulting best fit coefficients (either a and b or a, b, and c) for each border were introduced into a K-Means Cluster Analysis algorithm incorporated in the SPSS statistical package (SPSS Inc., Chicago, Il). This clustering method is based upon nearest neighbor sorting, whereby each case is assigned to the cluster for which the distance between the cluster center and the case is a minimum.[20] Since the cluster centers are not known initially, they are iteratively estimated from the data. The coefficients for the CC-view and MLO-view borders were analyzed separately. Absolute values of the b-coefficients were used since the curve shapes for positive and negative b-values are mirror images of one another. Thus the same filter could be employed; it would simply have to be flipped 180 degrees for one of the b-value polarities. We used the K-Means method to classify the borders into 2, 3, 4, 5, 6, 8, and 10 clusters.

In addition, we performed limited studies of various modifications of traditional K-Means clustering. In one, which we termed the "hybrid technique," the a and b parameters were employed (c set to 0) when the fit to a given

border using $y=ax^2+bx^3$ was better than a threshold value (e.g., when the rms error was $\leq$3 mm (3 pixels)). Otherwise, the border was refit using $y=ax^2+bx^3+cx^4$, and the a, b, and c parameters of that fit were employed. This hybrid method is based on the assumption that if the fit to the 2-parameter equation is sufficient, it is not necessary to use a 3-parameter fit. It is further assumed that under those circumstances, use of the coefficient (c) of the fourth order term only adds noise to the data being clustered.

In a second modification, we used the Z-scores of the variables (a, b, and c) rather than the variables themselves in the cluster analysis. The Z-score is the number of standard deviations that a given variable for a particular border differs from the mean value for all borders. Such a method makes the importance of each parameter more equivalent. It compensates for the wide variations in the magnitudes of the parameters. For example, the b-values were about 20 to 200 times smaller than the a-values, and the c-values were about 20 to 500 times smaller than the b-values.

Finally, in a third modification, we first applied K-Means Cluster analysis to the entire CC border set to obtain six clusters. We then fixed the cluster membership for the two best clusters, eliminated the corresponding borders from the data set, and performed K-Means Cluster analysis on the remaining borders. The second stage cluster analysis classified the remaining borders into 4, 5, or 6 clusters. The resulting total number of clusters was 6, 7, or 8, respectively. The underlying assumption for this method was that better clustering might be obtained in the second stage for the smaller set of borders. Thus, the overall clustering would be better than when the entire set of borders was clustered all at one time.

E. Determination of filter shapes and refitting of borders

Once the classification of each border was determined, the mean a and b values or mean a, b, and c values for the borders within each class were determined. The border defined by the equation using the mean coefficients defined the "filter." A computer routine was written to translate and rotate each of the individual borders within each class to best match their corresponding "filter." This routine again utilized coarse and fine increments for translation and rotation similar to the increments employed in the original fitting routine. The translation and rotation values determined with the original fitting routine were employed as starting values for the matching routine. The rms distance between the individual border and the filter of its class was minimized as an indication of best match. For each filter or class, the mean and standard deviation of the rms distances were computed. These values were used to quantitatively assess the success of the border classification. Also, for each type of clustering, the overall mean rms distance for all of the filters was computed using the equation:

$$\bar{d}=\sum_{g=1}^{N}\sum_{i=1}^{P_g} \mathrm{rms}_{ig}/T,$$

where N is the total number of clusters (e.g., 2, 3, 4, 5, 6, 7, 8 or 10), P_g is the number of borders in cluster g, rms_{ig} is the rms distance between border i and the filter for cluster g, and T is the total number of borders (e.g., $T=\Sigma_{g=1}^{N} P_g$). In addition, a figure of merit (FOM) was derived to estimate the optimal number of clusters. The equation employed was

$$\mathrm{FOM}=\sum_{g=1}^{N} (P_g/(\overline{\mathrm{rms}_g})^2)/\sqrt{N},$$

where P_g and N are as defined above, and $\overline{\mathrm{rms}_g}$ is the average rms error for cluster g. The denominator in this equation ($\sqrt{N}$) is a term that penalizes the use of larger numbers of clusters, and the numerator gives greater weight to those clusters having greater number of borders and smaller rms errors. Finally, the newly rotated and translated borders were refit with the equations $y=ax^2+bx^3$ and $y=ax^2+bx^3+cx^4$. The new coefficients, (a,b) and (a,b,c), were plotted to enable visual evaluation of the success of classification.

F. Investigation of optical density and exposure values near the filter position

The filters that will eventually be built must be custom-shaped in the thickness dimension to compensate for the variations in x-ray transmission at the periphery of the breast. To assess this effect, we computed mean optical density and mean exposure profiles along normals to the "filter" contour for one of the highly populated clusters in the classification study of CC-view mammograms. The particular cluster consisted of 231 of the 470 CC-view borders, and it was computed by the K-Means technique for the case in which there was a total of six clusters, and the borders were fit with the equation $y=ax^2+bx^3$. Twenty-one equally spaced normals were derived along the contour of the "filter." Each normal started at a position about 1 cm outside the "filter" contour and extended about 2 cm inside the contour (into the breast). The pixel values at the points along the normals were converted to optical densities using a pixel value to optical density transform derived from the film digitizer calibration curve. The means and standard deviations of the optical densities along each normal were computed. To convert the optical densities to x-ray exposures, which would eventually be needed for the filter design, we derived a film characteristic curve using x-ray sensitometry. The curve was generated with a bootstrap method using three mAs values (2, 20, and 100), four focus-to-film distances (23.5, 33.5, 47.5, and 66.5 cm), and three Lucite attenuator thicknesses (12, 24, and 36 mm). Within each segment, the four distances were employed at fixed mAs and fixed attenuator thickness. This was done to avoid errors due to reciprocity law failure and due to changes in x-ray beam quality. The curve segments were then bootstrapped together to create a characteristic curve extending over the entire exposure range. All measurements were made at 28 kVp, which is typical for the wide range of mammograms analyzed in this study. A

TABLE I. Results of fitting the CC- and MLO-view borders with the equations $y=ax^2+bx^3$ and $y=ax^2+bx^3+cx^4$.

No. of images	View	Type of fit	Mean rms error between fit and run-length averaged automatically tracked border (mm)
470	CC	a,b	2.18
470	CC	a,b,c	1.07
484	MLO	a,b	1.53
484	MLO	a,b,c	1.07

Keithley (Cleveland, Ohio) model 35050A dosimeter with a Keithley model 96035 15-cc ionization chamber was used to measure the exposures at the closest position, and the exposures at other positions were computed using the inverse square law.

III. RESULTS

The average rms errors for the fitting of the original run-length averaged borders with the equations $y=ax^2+bx^3$ and $y=ax^2+bx^3+cx^4$ are compared in Table I. The data in the fourth column of this table demonstrate that both fits are very good [errors are ~2 mm (pixels) or less], and use of 3-coefficients (a,b,c) reduced the fitting errors by about 30%–50%. An example of a fitted curve for which the rms error is equal to the mean value for all MLO views (1.53 mm) using the a and b parameters is displayed in Fig. 3, below. Figure 4 illustrates a case in which the rms error was 4.03 mm for the two parameter (a,b) fit and 1.18 mm for the three parameter (a,b,c) fit.

Clustering results are listed in Tables II to IV. The mean rms distances or errors between individual borders within clusters and their corresponding "filters" for CC-view borders are listed in Table II and those for the MLO-view borders are listed in Table III. The overall mean rms distances between the borders and filters for the various clustering parameters and methods are listed in Table IV.

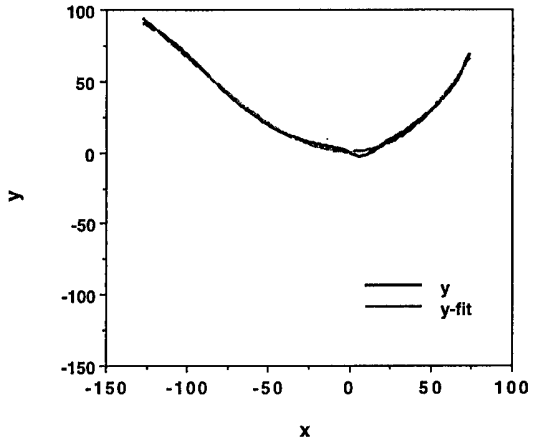

FIG. 3. Example of a fit for an MLO-view in which the fitted border (lighter curve) has an rms error of 1.53 mm, which is equal to the mean value for all MLO-views obtained using the a- and b-parameter fitting routine.

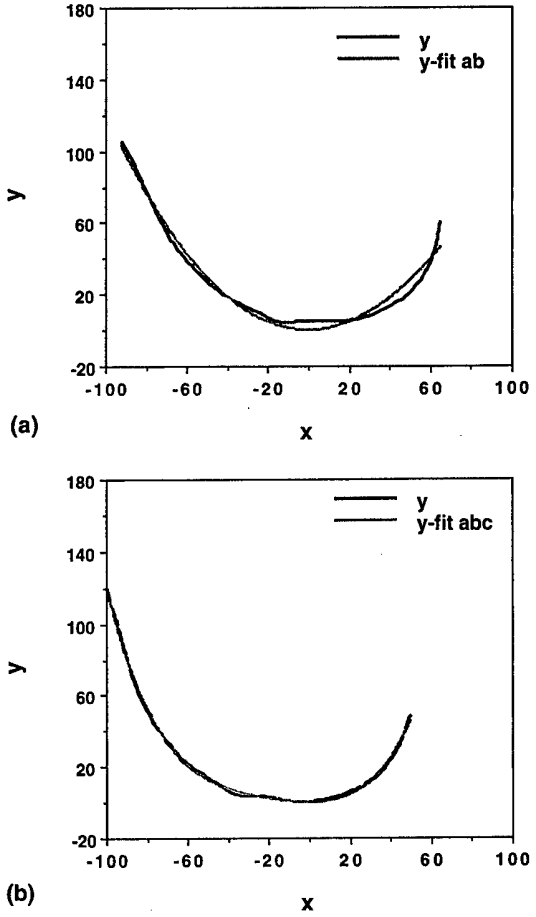

FIG. 4. Example of a case in which a fitted border using the 3-coefficient (a,b,c) equation is significantly superior to that using the 2-coefficient (a,b) equation. The same MLO-view border was fit using both equations. The rms error for the 2-coefficient fit (part a) is 4.03 mm and that for the 3-coefficient fit (part b) is 1.18 mm.

Scattergrams displaying the original a and b fitting coefficients for the 470 CC-view borders and 484 MLO-view borders are shown in Fig. 5. These are the a and b values that are input into the K-Means Cluster analysis program. Figure 6 shows examples of the a and b and a, b, and c values of the second-stage fits to the borders after they were translated and rotated to best match the cluster "filter" (the curve generated with the mean coefficients for the cluster).

Our clustering figure of merit as a function of number of clusters is plotted in Fig. 7.

Figure 8 shows an overlay of a "filter" and its associated normals on a mammogram whose automatically traced breast border was clustered to belong to the filter shape. Examples of filter shapes for the CC- and MLO-views are illustrated in Fig. 9(a) and (b), respectively.

Finally, plots of the mean film optical densities as a function of position along normals to the "filter" are shown in Fig. 10(a) and (b). As described in the Materials and Methods section, the mean values were obtained from the 231

TABLE II. Mean rms distances (mm) between individual borders and "filters" for CC-views. (Standard deviations for each distribution are noted in parentheses.) Results in each row are ordered from the smallest mean rms distance to the largest. n = number of borders in a particular cluster.

(A). a,b fit Total no. of clusters	Cluster 1	2	3	4	5	6	7	8	9	10
2	2.7 (1.4) $n=314$	3.7 (2.1) $n=156$								
3	2.2 (1.2) $n=139$	2.6 (1.2) $n=248$	4.1 (2.4) $n=83$							
4	2.0 (1.1) $n=93$	2.4 (1.1) $n=235$	3.5 (4.0) $n=9$	3.6 (2.0) $n=133$						
5	2.1 (1.1) $n=137$	2.5 (1.2) $n=232$	3.5 (4.1) $n=9$	3.7 (2.7) $n=4$	3.8 (2.1) $n=88$					
6	2.1 (1.1) $n=131$	2.5 (1.2) $n=231$	3.1 (3.3) $n=5$	3.7 (2.7) $n=4$	3.7 (2.1) $n=95$	3.9 (6.1) $n=4$				
6 (2 best from 6 clusters+ recluster remaining into 4 clusters)	2.1 (1.1) $n=131$	2.5 (1.2) $n=231$	3.4 (2.1) $n=60$	3.5 (4.1) $n=9$	3.7 (2.7) $n=4$	3.8 (2.1) $n=35$				
7 (2 best from 6 clusters+ recluster remaining into 5 clusters)	2.1 (1.1) $n=131$	2.5 (1.2) $n=231$	3.4 (2.1) $n=60$	3.4 (2.9) $n=2$	3.5 (4.1) $n=9$	3.8 (2.0) $n=35$	3.8 (2.9) $n=2$			
8 (2 best from 6 clusters+ recluster remaining into 6 clusters)	2.1 (1.1) $n=131$	2.5 (1.2) $n=231$	3.1 (3.3) $n=5$	3.4 (2.2) $n=55$	3.4 (2.9) $n=2$	3.7 (1.9) $n=40$	3.8 (2.9) $n=2$	3.9 (6.1) $n=4$		
8	1.7 (0.9) $n=52$	2.0 (0.9) $n=119$	2.3 (1.2) $n=144$	3.0 (1.7) $n=93$	3.1 (3.3) $n=5$	3.7 (2.7) $n=4$	3.8 (2.3) $n=49$	3.9 (6.1) $n=4$		
10	0.9 (0) $n=1$	1.7 (0.9) $n=52$	2.0 (0.9) $n=113$	2.3 (1.2) $n=145$	2.8 (1.5) $n=89$	3.2 (3.1) $n=4$	3.4 (2.9) $n=2$	3.8 (2.9) $n=2$	3.9 (2.3) $n=58$	3.9 (6.1) $n=4$

(B). a,b,c fit Total no. of clusters	Cluster 1	2	3	4	5	6	7	8	9	10
2	2.9 (1.7) $n=82$	3.1 (2.0) $n=388$								
3	2.8 (1.7) $n=175$	3.2 (2.0) $n=23$	3.2 (2.1) $n=272$							
4	2.7 (1.8) $n=205$	2.9 (1.9) $n=60$	3.2 (2.0) $n=199$	3.6 (2.2) $n=6$						
5	2.4 (1.4) $n=34$	2.7 (1.7) $n=136$	3.0 (2.0) $n=202$	3.6 (2.4) $n=92$	3.6 (2.2) $n=6$					
6	1.0 (0.0) $n=1$	2.4 (1.4) $n=34$	2.7 (1.7) $n=136$	2.9 (2.2) $n=5$	3.0 (2.0) $n=204$	3.6 (2.4) $n=90$				
6 hybrid[a]	1.7 (2.0) $n=7$	2.0 (1.1) $n=157$	2.2 (0.7) $n=48$	2.3 (1.9) $n=139$	4.2 (2.8) $n=80$	4.5 (2.8) $n=44$				
6 using Z-scores	1.0 (0.0) $n=1$	1.3 (0.8) $n=2$	1.4 (0.0) $n=1$	2.6 (1.6) $n=136$	3.1 (2.0) $n=309$	4.4 (4.1) $n=21$				
8	1.0 (0.0) $n=1$	1.3 (0.0) $n=1$	1.8 (1.0) $n=4$	2.4 (1.5) $n=28$	2.7 (1.6) $n=109$	2.8 (2.0) $n=130$	3.0 (1.8) $n=145$	4.0 (2.7) $n=52$		
8 hybrid[a]	0.8 (0.1) $n=3$	1.9 (1.8) $n=4$	2.0 (1.1) $n=140$	2.1 (1.5) $n=134$	2.2 (0.6) $n=44$	3.7 (2.2) $n=52$	4.1 (3.8) $n=66$	4.6 (3.0) $n=27$		
10	0.7 (0.0) $n=1$	1.0 (0.0) $n=1$	1.3 (0.0) $n=1$	2.1 (1.0) $n=3$	2.4 (1.5) $n=28$	2.7 (1.6) $n=103$	2.8 (2.0) $n=107$	2.9 (1.7) $n=122$	3.1 (2.0) $n=72$	4.2 (2.8) $n=32$

[a]Hybrid=use a,b coefficients ($c=0$) when original fit error $\leq$3.0 mm, use a,b,c coefficients when original fit error>3.0 mm.

TABLE III. Mean rms distances (mm) between individual borders and "filters" for MLO-views. (Standard deviations for each distribution are noted in parentheses.) Results in each row are ordered from the smallest mean rms distance to the largest. n = number of borders in a particular cluster.

(A). a,b fit

Total no. of clusters	Cluster 1	2	3	4	5	6	7	8	9	10
2	2.2 (1.1) $n=306$	3.2 (1.9) $n=178$								
3	1.9 (0.9) $n=172$	2.2 (1.1) $n=227$	3.5 (2.0) $n=85$							
4	1.7 (0.7) $n=107$	1.9 (0.8) $n=219$	2.9 (1.4) $n=134$	4.1 (1.9) $n=24$						
5	1.7 (0.7) $n=154$	1.8 (0.8) $n=58$	2.2 (1.1) $n=185$	3.4 (1.8) $n=83$	4.0 (3.1) $n=4$					
6	1.6 (0.7) $n=109$	1.9 (0.8) $n=179$	2.1 (0.7) $n=18$	2.5 (1.3) $n=129$	3.3 (3.1) $n=3$	3.7 (1.9) $n=46$				
8	0.6 (0.0) $n=1$	0.8 (0.0) $n=1$	1.6 (0.7) $n=142$	1.8 (0.8) $n=64$	2.0 (0.8) $n=165$	3.0 (1.4) $n=87$	4.0 (2.0) $n=22$	4.0 (3.2) $n=2$		
10	0.6 (0.0) $n=1$	0.8 (0.0) $n=1$	1.5 (0.6) $n=81$	1.5 (0.0) $n=1$	1.7 (0.7) $n=117$	1.9 (0.8) $n=150$	2.1 (0.7) $n=17$	2.8 (1.4) $n=71$	3.3 (1.6) $n=35$	4.8 (2.3) $n=10$

(B). a,b,c fit

Total no. of clusters	Cluster 1	2	3	4	5	6	7	8	9	10
2	2.9 (2.2) $n=191$	3.6 (2.3) $n=293$								
3	2.7 (2.3) $n=234$	3.1 (1.9) $n=81$	3.9 (2.4) $n=169$							
4	2.9 (2.2) $n=229$	2.9 (2.2) $n=123$	4.0 (2.5) $n=130$	6.4 (1.6) $n=2$						
5	2.4 (1.9) $n=188$	3.0 (2.3) $n=81$	3.2 (2.2) $n=153$	4.9 (3.0) $n=60$	6.4 (1.6) $n=2$					
6	2.3 (2.1) $n=140$	2.9 (1.8) $n=71$	3.3 (2.4) $n=147$	3.7 (2.3) $n=111$	4.8 (3.3) $n=13$	6.4 (1.6) $n=2$				
6 Hybrid[a]	1.5 (0.3) $n=2$	2.1 (1.5) $n=138$	2.4 (2.4) $n=152$	2.6 (1.1) $n=65$	3.3 (3.0) $n=106$	5.5 (4.8) $n=21$				
8	0.3 (0.0) $n=1$	1.3 (0.0) $n=1$	2.6 (2.0) $n=127$	2.6 (1.4) $n=53$	2.7 (2.7) $n=76$	3.3 (2.3) $n=115$	3.7 (2.4) $n=98$	4.8 (3.3) $n=13$		
10	0.3 (0.0) $n=1$	1.3 (0.0) $n=1$	2.4 (2.4) $n=78$	2.8 (2.0) $n=114$	2.8 (1.0) $n=13$	2.8 (1.5) $n=28$	3.2 (2.0) $n=76$	3.4 (2.4) $n=97$	3.5 (3.2) $n=7$	4.9 (3.4) $n=41$

[a]Hybrid=use a,b coefficients ($c=0$) when original fit error ≤ 3.0 mm, use a,b,c coefficients when original fit error >3.0 mm.

mammograms containing compressed breast borders that were classified to belong to a particular cluster. The clustering involved 470 CC-view borders which were classified into six groups using a and b parameters. Curves depicting the mean $+/-1$ standard deviation for several of the normals are shown in Fig. 10(c). Figure 10(d) depicts the mean relative x-ray exposures at the film plane as a function of position along the normals.

IV. DISCUSSION

Even though the original fits are better for three coefficients (a, b, and c) instead of two (a and b) (see Table I),

TABLE IV. Overall mean rms distance between individual borders and "filters."

Total no. of clusters	Overall mean rms error (mm) CC-View *ab*-fit	CC-View *abc*-fit	MLO-View *ab*-fit	MLO-View *abc*-fit
2	3.02	3.11	2.54	3.34
3	2.73	3.05	2.33	3.18
4	2.68	2.97	2.25	3.24
5	2.67	2.98	2.19	3.11
6	2.66	2.97	2.18	3.12
8	2.48	2.91	2.12	3.07
10	2.48	2.89	2.09	3.11
6 hybrid	-	2.69	-	2.68
6 using Z-scores	-	2.99	-	-
6 (2 best from 6 clusters +recluster remaining into 4 clusters)	2.63	-	-	-
7 (2 best from 6 clusters +recluster remaining into 5 clusters)	2.63	-	-	-
8 (2 best from 6 clusters +recluster remaining into 6 clusters)	2.62	-	-	-
8 hybrid	-	3.03	-	-

there is either only slight improvement [e.g., for 6 clusters in the CC case (Table II A, B)] or no improvement [for the MLO case (Table III A, B)] in the clustering success as measured by the mean rms distances between the individual borders within a class and the mean border or "filter." In fact, the overall mean rms error results listed in Table IV indicate that, in general, better matches between the individual borders and the filters are achieved when the filters are based upon the a,b clustering. Therefore, the 2-coefficient fit is preferred.

The number of filters to be employed in our exposure equalization method must be a compromise between goodness-of-fit and practicality. The results in Table IV indicate the goodness-of-fit, as represented by the overall mean rms distance error, generally improves as the number of clusters increases. However, this improvement is not very great beyond three or four clusters. The individual cluster results in Tables II and III also exhibit this trend, and the figures of merit that were derived (see Fig. 7) peak at about three clusters. Therefore, three or four filter shapes for each view appear to be optimum.

The hybrid approach of using a and b values with c set to zero when the original fit to the automatically traced border is less than or equal to a threshold value and using a, b, and c values otherwise improves the clustering relative to use of the conventional a, b, and c values in some cases (e.g., Table III B), but degrades clustering in others (e.g., Table II B). However, for all of the hybrid cases shown in the tables, the corresponding clustering that is obtained using the same total number of clusters and only the a and b parameters of the fit equation $y=ax^2+bx^3$ yields superior results.

Use of the Z-scores of the a, b, and c values rather than the values themselves did not improve clustering (Table II B). The effect of employing the two best clusters of six from

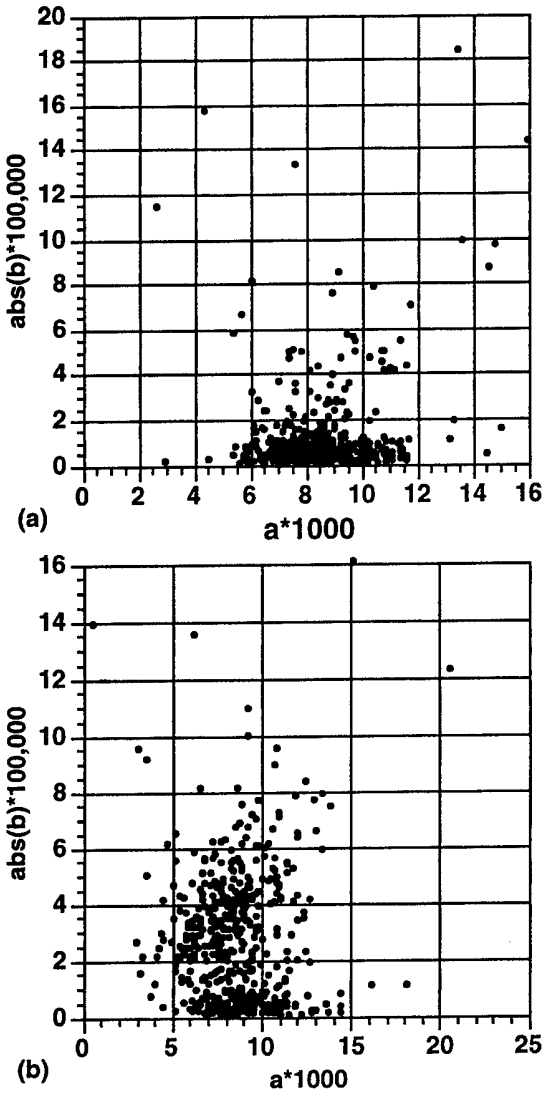

FIG. 5. Plots of a and b values of original $y=ax^2+bx^3$ fits to borders of (a) 470 CC-view and (b) 484 MLO-view mammograms. Absolute values of b are plotted since the shapes of the curves for positive and negative b-values are mirror images of one another.

an initial cluster analysis followed by reclustering the remaining borders into 4, 5, or 6 groups was an insignificant ($\sim 1.2\%-1.5\%$) improvement.

Figure 10(c) provides an example of the variability in the optical densities near the periphery of the breast that might be expected for a set of compressed breasts classified to be of a particular shape. The standard deviations of the optical densities range from about 0.2 to 0.6 OD. This translates to a fairly wide range of exposure values, especially in the high density region just outside the breast border. Our calculations show that, in this region, the mean exposure to the film minus 1 standard deviation is about half the mean exposure value. The mean exposure to the film plus 1 standard deviation could not be determined just outside the breast because these exposures are in the shoulder region of the film characteristic curve, where there are large uncertainties in the optical density to relative exposure conversion. Also, the op-

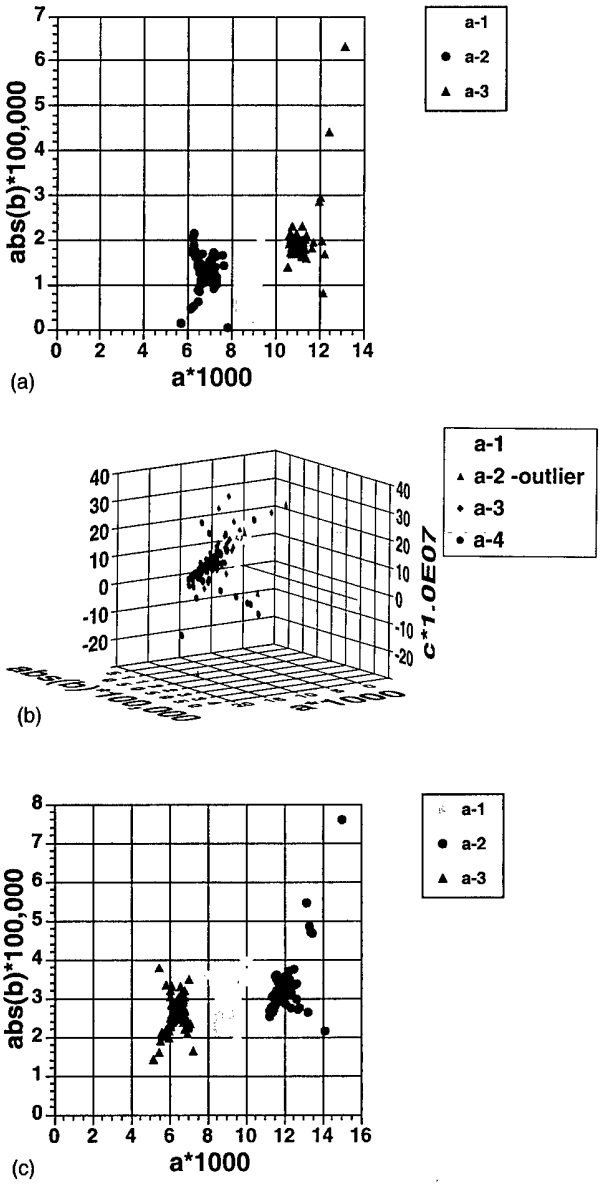

FIG. 6. Pictorial representations of clustering. The borders that are classified into each cluster are translated and rotated to best match the average border (filter) for that cluster, and they are then re-fit with the equations $y=ax^2+bx^3$ and $y=ax^2+bx^3+cx^4$. The resulting a,b, or a,b, and c coefficients are plotted. Part (a) shows the a,b coefficients, and part (b) shows the a,b, and c coefficients that are generated when the 470 CC-view borders were clustered into 3-groups for a,b and 4-groups for a,b,c. (The outlier in the second group for the a,b,c clustering had (a*1000, b*100,000, c*10^7) coordinates of (5.1, 93.4, −71.7) and was not plotted so the other data points could be better visualized.) Part (c) shows the a,b coefficients that are generated when the 484 MLO-view borders were clustered into three groups. The particular sets shown represent the better clustering results based on the figure of merit criteria for a,b clustering, and a close to minimum overall mean rms error for a,b,c clustering (see Fig. 7 and Table IV).

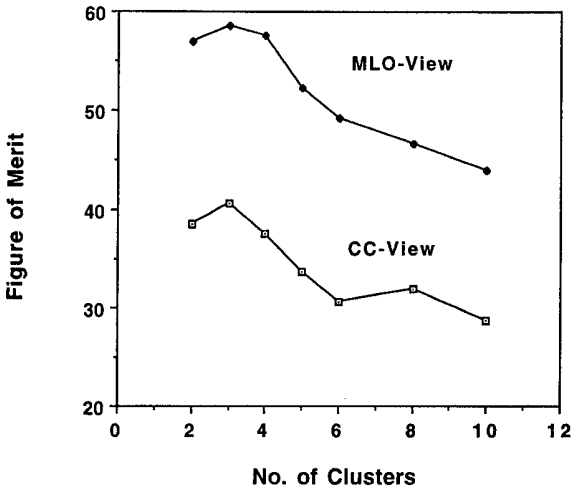

FIG. 7. Plots of clustering figure of merit as a function of number of clusters for the CC- and MLO-views. Both exhibit maximum figure of merits at about three clusters.

tical densities in this region could not be digitized to good accuracy with our film digitizer. A review of Fig. 10(c) also shows that the optical density ranges within the breast are about as variable as those outside the breast for the mammograms in this cluster. Some of this variability can be attributed to differences in breast thickness and composition in the regions and some can be attributed to variations in phototimer response, technique (kVp), and film processor conditions.

It is possible that up to three filters of different degrees of equalization will be necessary for the dense, mixed dense and fatty, and fatty breasts or for the thick, medium, and thin breasts in the same breast shape class. We plan to conduct further studies to determine the acceptable range of variation in the primary exposure profiles for each filter subclass. Once the filter subclass criteria are set and the breast images are grouped into the subclasses, the average primary exposure profile of the breast images in a given filter subclass will be

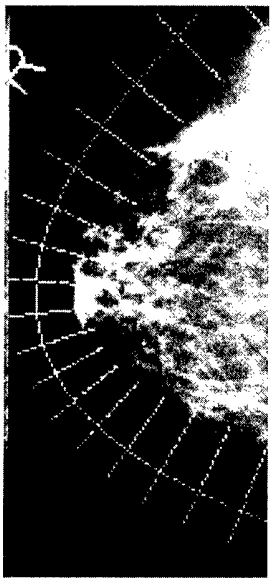

FIG. 8. Example showing overlay of "filter" contour and normals to that contour on one of the mammograms that is classified to belong to the filter shape. The mammogram was histogram equalized using NIH Image to better visualize the breast tissue out to the periphery. The rms distance error to the average "filter" shape is 3.19 mm for this case.

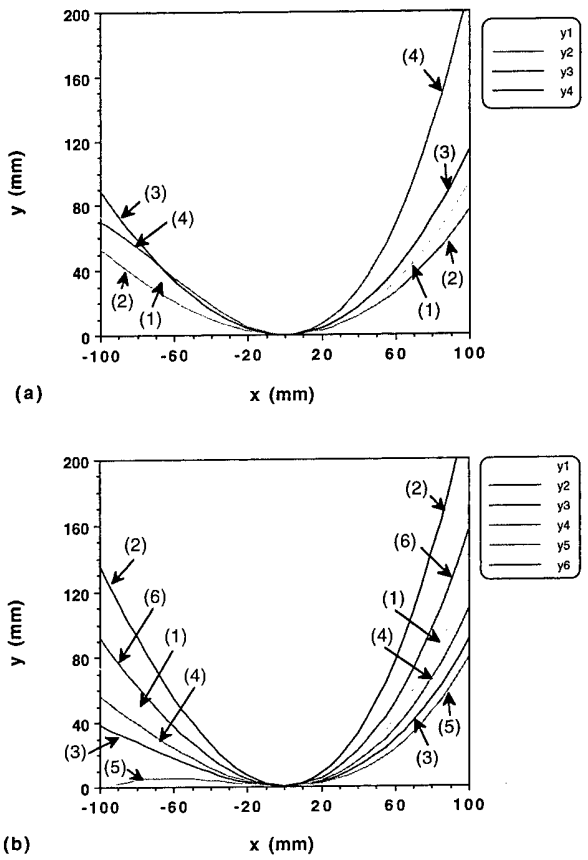

FIG. 9. Examples of "filter" shapes. (a) represents the "filter" shapes derived when the 470 CC-view borders were clustered into 4 groups using the $y=ax^2+bx^3$ fitting equation. (b) represents the "filter shapes derived when the 484 MLO-view borders were clustered into six groups using the $y=ax^2+bx^3$ fitting equation. The number of borders that are classified as being the same shape as the filters in (a) are: 235 for filter #1, 93 for filter #2, 133 for filter #3, and 9 for filter #4. The number of borders that are classified as being the same shape as the filters in (b) are 129 for filter #1, 3 for filter #2, 109 for filter #3, 179 for filter #4, 18 for filter #5, and 46 for filter #6.

estimated by averaging the primary exposure profiles obtained from the individual mammograms in that subclass. The thickness profile of a filter for this subclass can then be derived for a given filter material.

The significance of this study is that, using a large data base of about 500 mammograms in each view, the results support our hypothesis that a small number of pre-fabricated filters will be sufficient to allow selection of a nearly patient-specific filter for each breast being examined. This is the basis of our approach to exposure equalization in mammographic imaging. With this technique, the dynamic range of the x-ray intensities incident on the recording system will be reduced and the entire image can be recorded in the high contrast region of the film. The improved image quality can be achieved without additional radiation dose to the patient. Furthermore, a very high-contrast mammographic technique may be developed in combination with exposure equalization to further improve the signal-to-noise ratio (SNR) of the subtle lesions in the entire breast. We expect that the optimized technique will significantly improve the detectability of cancers in mixed and dense breasts and increase the efficacy of mammography as a screening and diagnostic tool for breast cancers.

In this work, we assumed that an rms fitting error between the filter contour and a particular breast border of 2 or 3 mm would be acceptable. We based this assumption on the fact that the filter will be smoothly shaped in the thickness dimension as well, which should result in a smooth exposure gradient rather than a step function. Therefore, small gaps between the breast and filter borders should be smoothed out in exposure space.

Mismatches between the filter exposure compensation profiles and the breast attenuation profiles can in practice result in artifacts. For example, if a portion of the filter extends too far toward the inside of the breast, the exposure in this region will be reduced too much, resulting in a light (low optical density) area in the mammogram. Such overcompensation is likely to occur in the MLO-view in the pectoral region where the filters, in general, do not match the breast shapes as well. The filters may have to be designed to have more gradual compensation in these regions to reduce artifacts. To better understand the potential for artifact production and the acceptable rms fitting errors, we are performing a simulation study in which exposure profiles generated in the present study are employed to construct simulated filters which are then applied to images belonging to particular compressed breast shape classes. The results of that study will be presented in a future publication.

Finally, it should be mentioned that our plans for the eventual implementation of the equalization technique do not require the use of a pre-exposure x-ray mammogram of the patient for filter selection. Rather, the filter will be selected based on the measured thickness of the patient's compressed breast, the breast contour as determined from a visible light image of the compressed breast recorded by a TV camera that is interfaced to a computer, and the clustering results gained from a large database of digitized mammograms with corresponding compressed breast thickness information as described in this study. Fabrication of individual filters for a functional system could be accomplished with either a computerized milling machine or stereolithography. Plastics doped with metals such as aluminum and copper might be employed as the filter material in either case to reduce the required filter thickness. The filters would be automatically positioned by a microprocessor controlled stage that translates and rotates the appropriate filter to a location such that the projected filter exposure profile matches the compressed breast border derived from the TV camera image. The filter positioner would be located close to the x-ray tube to minimize x-ray scatter to the breast and minimize artifact production. The individual filters could be placed in the positioner manually, or an automated filter wheel could be developed. Lastly, the entire filter selection/positioning process should take place in only a few seconds to minimize patient discomfort from any additional time the breast must remain compressed.

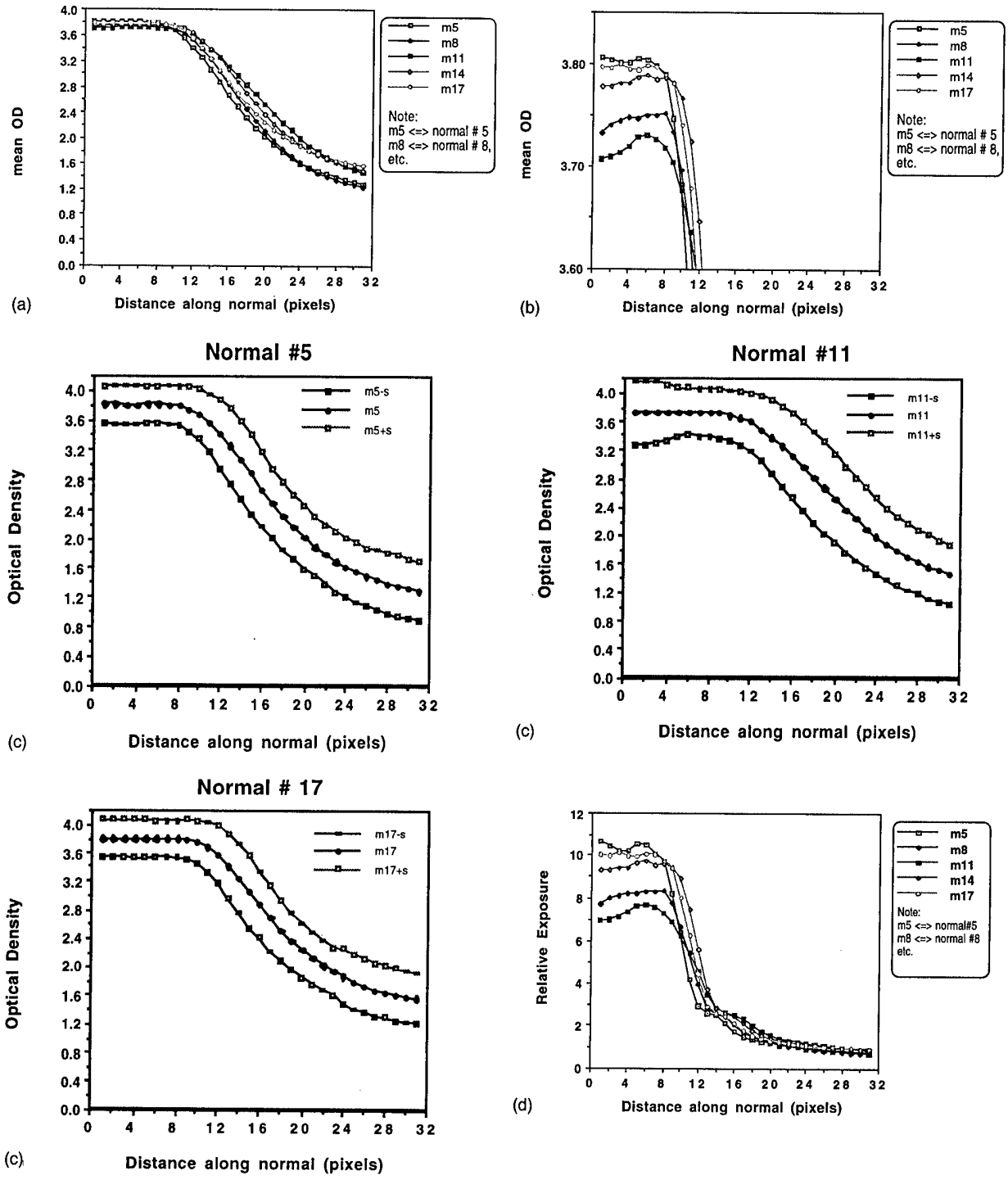

FIG. 10. (a) Mean optical density as a function of position along normals to the filter when the filter is aligned with the automatically detected borders in mammograms classified to belong to the filter shape. For the particular case shown, 231 CC-view borders were classified to match the filter. Pixel #11 along each normal corresponds with the filter edge. Pixels less than 11 are outside the breast, and those greater than 11 are inside the breast. Normal #11 is the middle normal (for a symmetric breast, it is closest to the nipple position). (b) Magnified view showing the details of the high optical density region in plot (a). (c) Mean optical density +/−1 standard deviation for selected normals. (d) Mean exposures corresponding to the optical densities in (a).

ACKNOWLEDGMENT

This work was supported in part by Grant No. DAMD 17-94-J-4292 from the USAMRMC.

[a]Corresponding author: Mitchell M. Goodsitt, Ph.D., University of Michigan Hospitals, Department of Radiology, Room B1F510C, 1500 E. Medical Center Drive, Ann Arbor, MI 48109-0030. Electronic-mail: goodsitt@umich.edu

[b]Present address: Vanstar Corp., 201 Hanfen Ct. Suite 119, Wood Dale, IL 60191.

[c]Present address: Industrial Electronics Lab, GE Corporate R&D, Schenectady, NY 12301.

[d]Present address: Health Physics Office, Walter Reed Army Medical Cen-

ter, Building 41, Rm. 38, 6825 16th St. NW, Washington DC 20307-5001.

[1]E. A. Sickles, "Mammographic features of "early" breast cancer," Am. J. Roentgenol. **143**, 461–464 (1984).
[2]E. A. Sickles, "Mammographic features of 300 consecutive nonpalpable breast cancers," Am. J. Roentgenol. **146**, 661–663 (1986).
[3]W. W. Logan and J. A. Janus, "Screen/film mammography," in *Breast Cancer Detection: Mammography and Other Methods in Breast Imaging*, 2nd ed., edited by L. W. Bassett and R. H. Gold (Grune & Stratton, New York, 1987).
[4]R. M. Nishikawa, G. E. Mawdsley, A. Fenster, and M. J. Yaffe, "Scanned-projection digital mammography," Med. Phys. **14**, 717–727 (1987).
[5]R. M. Nishikawa and M. J. Yaffe, "An investigation of digital mammographic imaging," Proc. SPIE **419**, 192–200 (1983).
[6]P. C. Bunch, K. E. Huff, and R. Van Metter, "Analysis of the detective quantum efficiency of a radiographic screen/film system," J. Opt. Soc. Am. A **4**, 902–909 (1987).
[7]H. R. Blackwell, "Contrast thresholds of the human eye," J. Opt. Soc. Am. **36**, 624–643 (1946).
[8]B. Baxter, H. Ravinda, and R. A. Normann, "Changes in lesion detectability caused by light adaptation in retinal photo-receptors," Invest. Radiol. **17**, 394–401 (1982).
[9]H. L. Snyder, "Chapter 3: The Visual System: Capabilities and Limitations," in *Flat-Panel Display and CRTs*, edited by L. E. Tannas, Jr. (Van Nostrand Reinhold, New York, 1985).
[10]L. D'Agincourt, "Technique is everything when breast is dense," Diagnostic Imaging, Sept., 57–61 (1993).
[11]K. L. Lam and H.-P. Chan, "Development of x-ray beam equalization technique in mammography," Radiology **169**(P), 338 (1988).
[12]K. L. Lam and H.-P. Chan, "Exposure equalization techniques in mammography," Invest. Radiol. **24**, 154–157 (1989).
[13]K. L. Lam and H.-P. Chan, "Effects of x-ray beam equalization on mammographic imaging," Med. Phys. **17**, 242–249 (1990).
[14]G. Panayiotakis, H. Likaki, Z. Kolitsi, and J. Dimopoulos, "An anatomical filter for exposure equalization in mammography," Eur. J. Radiol. **15**, 15–17 (1992).
[15]J. M. Sabol, I. C. Soutar, and D. B. Plewes, "Mammographic scanning equalization radiography," Med. Phys. **20**, 1505–1515 (1993).
[16]J. W. Oestmann, B. Stoel, H. Schrijvershof, J. Vrooman, and L. J. Schultze Kool, "Scanning equalization mammography: Preliminary evaluation," Radiographics **14**, 123–128 (1994).
[17]J. M. Sabol, I. C. Soutar, and D. B. Plewes, "Practical application of a scan-rotate equalization geometry to mammography," Med. Phys. **23**, 1987–1996 (1996).
[18]A. R. Morton, H. P. Chan, and M. M. Goodsitt, "Automated model-guided breast segmentation algorithm," Med. Phys. **23**, 1107–1108 (1996).
[19]M. M. Goodsitt, H.-P. Chan, B. Liu, S. Guru, and R. Morton, "Compressed breast shape classification for the design of mammography equalization filters," Med. Phys. **23**, 1108 (1996).
[20]M. R. Andenberg, *Cluster Analysis for Applications* (Academic, New York, 1973).

Design and evaluation of an external filter technique for exposure equalization in mammography

Shyam P. Keshavmurthy, Mitchell M. Goodsitt, Heang-Ping Chan,[a] Mark A. Helvie, and Emmanuel Christodoulou
Department of Radiology, University of Michigan, 1500 E. Medical Center Drive, Ann Arbor, Michigan 48109–0030

(Received 8 July 1998; accepted for publication 16 April 1999)

We are developing an external filter method for equalizing x-ray exposure in the peripheral region of the breast. This method requires the use of only a limited number of custom-built filters for different breast shapes in a given view. This paper describes the design methodology for these external filters. The filter effectiveness was evaluated through a simulation study on 171 mediolateral and 196 craniocaudal view digitized mammograms and through imaging of a breast phantom. The degree of match between the simulated filter and the individual 3-D exposure profiles at the breast periphery was quantified. An analysis was performed to investigate the effect of filter misalignment. The simulation study indicates that the filter is effective in equalizing exposures for more than 80% of the breast images in our database. The tolerance in filter misalignment was estimated to be about ±2 mm for the CC view and ±1 mm for the MLO view at the image plane. Some misalignment artifacts were demonstrated with simulated filtered mammograms. © *1999 American Association of Physicists in Medicine.* [S0094-2405(99)01108-6]

Key words: mammography, equalization, external filtration, simulation

I. INTRODUCTION

Radiographic contrast plays a crucial role in the detection of subtle lesions that are signs of early breast cancer. Since radiographic contrast decreases with increasing hardness of the x-ray spectrum,[1] low-energy radiation and high-contrast screen/film systems are recommended to maximize the contrast between a lesion and the background breast tissue. The low energy x rays used in mammography and reduced tissue thickness at the breast periphery result in a large exposure range in a breast image. We have estimated that the exposure range for a 5-cm-thick breast of dense fibroglandular tissue can be as great as 145:1 for a 28 kVp Mo/Mo spectrum. Since a typical high-contrast film used in mammography provides a narrow latitude in the range of about 10:1, it generally cannot accommodate the wide exposure range of a breast image.[2,3] The radiographic contrast of mammographic features imaged at the toe and the shoulder regions of the sensitometric curve is greatly reduced. Stacey-Clear *et al.*[4] have shown, in their study of breast cancer location in women aged under 50, that 73% of the cancers (63 out of 86) were at the periphery of the breast parenchyma, with the majority near the subcutaneous fat. Since the contrast sensitivity of the human visual system also decreases rapidly with an increase in the film density,[5–7] the poor image quality in the peripheral region imposes a serious limitation on the sensitivity of cancer detection in breasts with dense fibroglandular tissue. These problems may be reduced if an exposure equalization technique can be developed for mammographic imaging.

Several exposure equalization methods have been proposed to improve mammographic imaging. In one method, a water bag[8–10] or a solid, elastic, unit density x-ray attenuator[11] fills the gap between the breast and the compression paddle to reduce the breast thickness variation in the peripheral region. This method can be patient-specific. However, it may be difficult to implement, especially for oblique views, when using a water bag. Another method involves scanning of the breast with either single or multiple intensity-modulated x-ray beams that are based upon x-ray transmission signals obtained from single or multiple detectors.[12–14] Such a method can equalize the exposure throughout the breast rather than just at the periphery. However, the method is complex and requires much greater heat loading of the x-ray tube than conventional mammography and much longer exposure time. The latter may result in significant motion artifacts. Better visualization of lesions at the breast periphery can be achieved by display equalization methods such as hot lighting and postprocessing of digital images.[15] These methods reduce the contrast threshold for perception. However, they do not improve the signal-to-noise ratio of the image.

We have proposed a new exposure equalization method for reducing the dynamic range of the mammograms.[16] This method employs a set of external x-ray beam intensity shaping filters that are positioned near the collimator of a mammography system. A similar technique was reported by Boone *et al.* for equalizing chest radiographs.[17] However, no x-ray pre-exposure will be required for filter selection in our approach. The proposed mammography equalization system is shown schematically in Fig. 1. A video camera will acquire a color image of a compressed breast. Next, an image segmentation program will be employed to extract the breast boundary. This breast border will then be classified into a breast shape group. A prefabricated exposure equalization

 0094-2405/99/26(8)/1655/15/$15.00

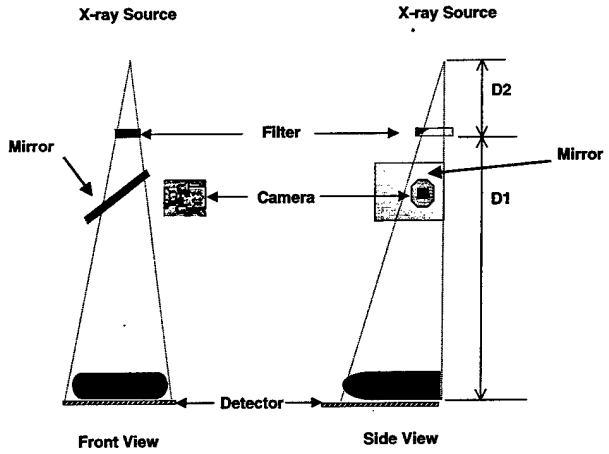

FIG. 1. Schematic of a mammography unit implemented with an equalization filter system.

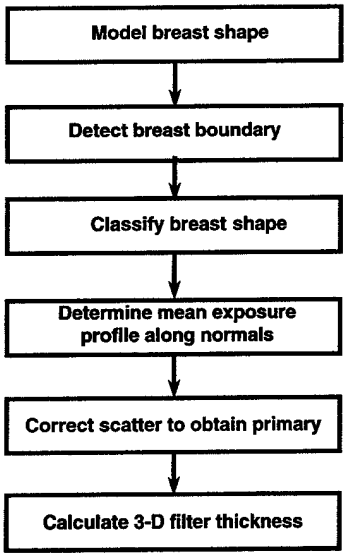

FIG. 2. Procedure for designing an external equalization filter.

filter corresponding to this group will be placed in the beam path and aligned with the breast border by a translation-rotation apparatus operated under computer control. The focal-spot-to-filter distance ($D2$) can be varied to match different breast sizes. The mirror shown in Fig. 1 is used to acquire the *TV* camera image and will be removed from the beam path before the acquisition of the x-ray image.

In an earlier study, Goodsitt *et al.*[16] demonstrated that compressed breasts can be classified into a finite number of shapes and therefore only a finite number of filters are needed for equalization. In this paper, we report the results of a computer simulation study that was conducted to determine the effectiveness of using a finite number of filters in equalizing the exposures of mammograms.

II. MATERIALS AND METHODS

A. Data set of digitized mammograms

1004 clinical mammograms acquired with a dedicated mammographic system with a Mo anode and Mo filter were randomly selected from patient files in our department. All mammograms were recorded with Kodak Min-R/Min-RE screen-film systems. The selected images included both craniocaudal (CC) and mediolateral oblique (MLO) views. The films were digitized with a DBA Systems, Inc. (Melbourne, FL) model ImageClear M2100 film digitizer. The light sensor of this system is composed of two linear arrays of charge coupling devices (CCD) that are butted together to form a contiguous array. The original pixels in each digitized image were averaged and subsampled to produce images with a 1×1 mm^2 pixel size. The digitized values were later converted to 12-bit logarithmic format to yield a fairly linear relationship between the film optical density (OD) and pixel value, with larger pixel values corresponding to lower ODs. The pixel value versus OD calibration curve leveled off at an OD of about 3.6, beyond which the pixel values remained almost constant.

B. Classification of breast shapes

An automated border-tracking algorithm was applied to the digitized images.[18] A total of 470 CC view and 484 MLO view automatically traced borders were analyzed. This is the same set of borders that was analyzed in our previous study.[16] In that study,[16] we found that the breast borders could be fit very well with the polynomial $y=ax^2+bx^3$. This functional form has the advantage of producing only two coefficients (a,b) which can be used in a cluster analysis to classify the border shapes. These coefficients were introduced into a k-means clustering algorithm. Optimal clustering was achieved for three or four groups in both CC and MLO views.

C. Filter design

Before building an actual system, we conducted a simulation study to investigate the effectiveness of the external filters. In this simulation study, we designed a simulated equalization filter for each group of breasts. The a-b polynomial fit discussed earlier only describes the projected breast shape on the image. It does not account for the thickness variation near the periphery of a compressed breast. The inclusion of this third dimension in the design of the filter is the subject matter of the present study. Changes in the breast thickness at the periphery are observed as changes in the gray scale values of pixels on the digitized mammogram. Because equalization occurs in the exposure domain, the pixel values have to be converted to exposures. The conversion involves use of the digitizer calibration curve and the sensitometric curve of the screen-film system. The exposure profiles at the breast periphery estimated from the digitized mammograms for a particular group can be used to design a three-dimensional (3-D) filter for that group.

The calculation procedure used for designing an exposure equalization filter is presented as a flow chart in Fig. 2. For each image, the pixel value profiles along a number of nor-

mals (25 to 35) to the automatically detected breast boundary[18] were obtained. Each normal consisted of 41 points that were 1 pixel apart, of which 20 points were outside the breast and 20 were inside the breast. The 21st point was exactly on the detected breast boundary. Thresholding criteria were employed to exclude pixels where the normals intersected lead markers or the pectoral muscle. The pixel values were converted to optical densities by using the CCD digitizer calibration curve and linear interpolation. The OD profiles along all the normals were averaged to obtain a mean OD profile for each breast. The mean OD profiles for all images in a given group were in turn averaged to obtain an average OD profile for the entire group. This process of multistep OD averaging ensured that a smooth relative exposure profile was used for filter design. This OD profile was subsequently converted to a relative exposure profile using a typical sensitometric curve for the Kodak Min-R/Min-RE screen film system.

The exposure in the profile is the total exposure including primary and scatter. The primary exposure, which the filter directly attenuates, can be obtained using the following relationship:

$$\bar{E}_p = \bar{E}_t(1-\mathrm{SF}), \tag{1}$$

where $\bar{E}_p$ is the mean primary exposure, $\bar{E}_t$ the mean total exposure, and SF the scatter fraction. Dance *et al.*[19] found in an earlier study that the scatter component of the total exposure depends on the breast composition, breast thickness, and x-ray spectrum. However, these factors were not known for the digitized mammograms used in our study. Also, there is a variation of the scatter fraction due to the decreasing thickness in the periphery region of the breast.[10] This variation depends on the thickness profile of a compressed breast and the tissue composition, which were not known. For the simulation study, we made the simplifying assumption that the scatter fraction was constant. The assumption of a constant scatter fraction causes the effect of the scatter fraction before and after equalization to cancel out. However, to keep the model complete, the scatter fraction is included in the discussion of the appropriate steps in the simulation study.

It should be noted that an actual equalization filter would effectively reduce the peak of the scatter fraction that occurs near the periphery of the breast, which was not included in our simulation. This would further improve the image quality in the peripheral region, as was shown by Lam and Chan.[10]

Ideally, equalization reduces the exposure at the breast periphery to approximately the same low value as that in the central region of the breast. The exposure reduction factor at a given point along a normal was therefore defined as the ratio of the minimum exposure on the normal to the relative exposure value at that point. A profile of average exposure reduction factors was generated and used to specify the filter for equalization of the breasts in a particular group.

To design a physical filter, the average exposure reduction factor profile along a normal was converted to a filter thickness profile using a filter thickness versus exposure reduction factor look-up table. Although the thickness matrix was not used in our simulation study, it would be useful for fabricating actual filters.

FIG. 3. Schematics of fabricating filters with (a) liquid or (b) solid material.

To generate a filter thickness-to-exposure reduction factor conversion table, a filter material was selected and the attenuation coefficients for this material were obtained using the XCOM[20] computer program. The attenuation coefficients were then used in the following relationship to calculate the exposure reduction that could be obtained with a given filter thickness:

$$Es_f(t_f) = \frac{\Sigma_E f(E) E e^{-\mu_f(E) t_f} (\mu_e(E)/\rho)_{\mathrm{air}}}{\Sigma_E f(E) E (\mu_e(E)/\rho)_{\mathrm{air}}}, \tag{2}$$

where $Es_f(t_f)$ is the filtered relative exposure, also referred to as the exposure reduction factor, $f(E)$ is the relative number of photons at a given energy E of the spectrum, $(\mu_e(E)/\rho)_{\mathrm{air}}$ is the mass energy absorption coefficient of air at energy E, and $\mu_f(E)$ and t_f are the linear attenuation coefficient at energy E and the thickness of the filter material, respectively. The mass energy absorption coefficients of air were obtained from Johns and Cunningham.[21] This calculation provided a relative exposure of 1 when the filter thickness was zero and a value less than 1 for larger filter thicknesses. In this study, we assumed a spectrum ($f(E)$) of Mo/Mo 28 kVp with a HVL of 0.32-mm Al.[22] The exposure reduction factor was stored along with the corresponding filter thickness as a look-up table for use in the filter design procedure.

Ideally, the energy absorbed in the screen rather than the exposure to the screen/film should be equalized. However, the energy absorption of the screen depends upon the x-ray spectrum incident on the screen. This spectrum is not known unless the imaging parameters (kVp and filtration), breast thickness, and composition are available, and Monte Carlo calculations are performed. For the design of an average filter for a breast group, the entire process involves a number of averaging and approximation steps. Since the goal of our approach is to reduce the exposure dynamic range rather than to produce perfect equalization, the error caused by the approximation of energy absorption in the screen by exposure will not impose a substantial effect.

We can use either solid materials, tissue-equivalent fluids or more radiodense liquids with radiation transparent molds enclosed in a sealed container to build the equalization filters. Figure 3 shows sketches of such solid and liquid filters. Examples of liquids that might be used in filters include water, saline, and water/alcohol solutions. Solid filters might be made of plastic or plastics impregnated with heavy elements.

D. Simulation study

To verify the effectiveness of external-filter-based exposure equalization, the entire filtration process was simulated using computer programs and was tested on digitized mammograms. In this simulation study the filter was positioned just above the compressed breast. This simplification enabled the use of fitted curves to the breast boundary for filter alignment calculations. Since the equalization process occurred in the exposure domain, the pixel values in the digitized images were converted to relative exposure values. The exposure reductions by the filter near the breast periphery were estimated and converted to changes in pixel values. The digitized image was corrected with the appropriate pixel value change at each pixel, producing a "filtered" digitized mammogram. Changes were implemented in the pixel value domain rather than the optical density domain, because it facilitated direct display and comparison of the equalized and unequalized images on a high-resolution workstation monitor. Furthermore, because this approach did not entail printing the filtered image on film for comparison with the original film, it avoided possible artifacts in the center of the filtered breast image caused by uncertainties in the pixel-value-to-OD conversion curve of the digitizer. Uncertainties in the pixel value changes in the peripheral region were digitally smoothed out to simulate filtration by a smooth physical filter, as detailed below. The various steps in the simulation process are presented as a flow chart in Fig. 4.

For a given mammogram to be equalized, the procedure started by detecting the boundary of the breast image using our automated breast border tracking program. The detected boundary was then fitted with the ax^2+bx^3 polynomial. Using the a and b values, the breast border was classified into a particular group. On the basis of this classification, the average equalization filter designed for that breast group was chosen. The equalization filter was represented by a 2-D ar-

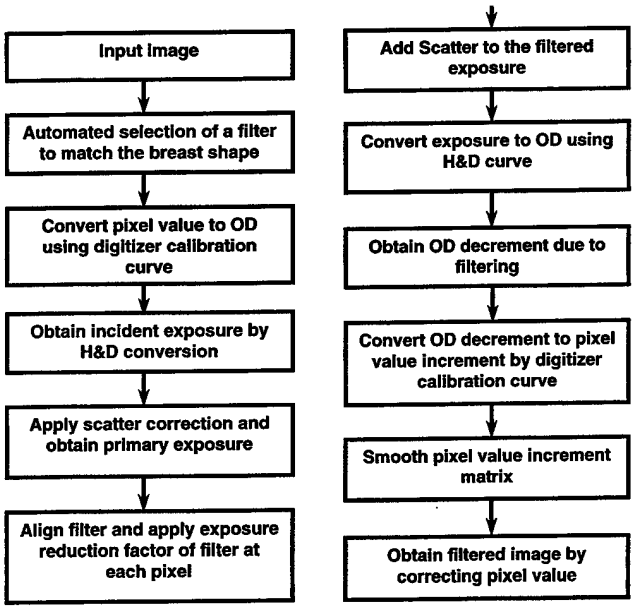

FIG. 4. Flow diagram of the simulation study for evaluation of the effects of x-ray equalization on mammograms.

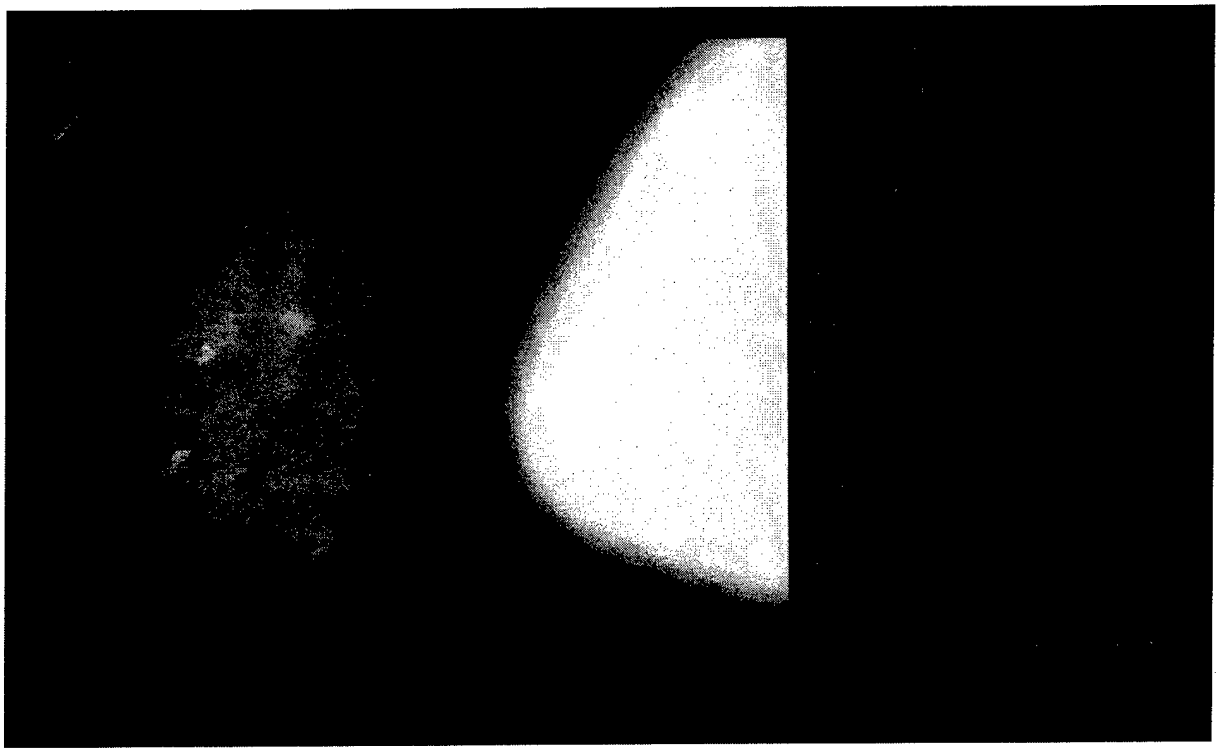

FIG. 5. An example of (a) a digitized mammogram, (b) an exposure reduction factor matrix displayed as a gray scale image, and (c) the corresponding pixel value increment matrix.

ray of exposure reduction factors described in Sec. II C. This exposure reduction factor array was rotated and translated along both the X and Y directions to achieve the best alignment between the filter and the breast image. The criterion for best alignment was assumed to be the minimization of the root-mean-square (rms) distance between the filter boundary and the automatically detected breast boundary. The pixel values in the digitized mammograms were then converted to OD using the digitizer calibration curve. The OD at each pixel was subsequently converted to relative exposure using a typical Hunter and Driffield curve for a Kodak Min-R/Min-RE screen film system.[23] The relative exposure thus obtained included both the primary and the scatter components. Since we assumed that the scatter fraction was constant over the entire breast area in this study, the total exposure would be proportional to the primary exposure. The exponential attenuation process of the filter could therefore be applied to the total exposure. The total exposure at each pixel location was reduced using the exposure reduction factor at that location. Exposure equalization by the external filter was accomplished at this step.

The equalized total exposure was subsequently converted back to OD using the H&D curve. This OD was compared with the original OD to obtain the OD decrement for a given pixel. This OD decrement was converted to a pixel value increment using the digitizer calibration curve. Because the conversion in each step involved uncertainties, especially in the shoulder and toe regions of the H&D curve, the 2-D array of pixel value increments contained numerical errors that would not exist with an actual filter. To reduce the fluctuations in the pixel value increments, a 2-D smoothing was performed by applying a 3×3-pixel convolution kernel to the pixel value increment array before the array was added to the original image.

Figure 5 shows an example of a digitized mammogram, the corresponding array of exposure reduction factors displayed as a gray scale image, and the array of pixel value increments also displayed as a gray scale image. The dark and gray areas in the background outside the breast indicate that the exposure reduction factor array was rotated and aligned to match the given breast shape. Additionally, the pixel value increment array is approximately a negative image of the exposure reduction factor array. The dark area within the breast region indicates pixel value increments of zero.

E. Filter misalignment analysis

We designed a Figure-of-Merit (FoM) to evaluate the "goodness of alignment" for our external-filter equalization method. First, approximately 25–35 equally spaced normals to the detected breast border were generated for each image. The pixel values in the digitized mammograms along these normals were obtained at 31 points. Only ten points outside the breast boundary were used because we were interested in the artifacts that occurred at the breast periphery. The pixel value increments used for equalization of the same image were also obtained along each normal and these values represented the 3-D profile of the filter. The pixel values decreased from the inside to the outside of the breast periphery, whereas the pixel value increments increased. The complement of the pixel value increment profile was computed by transforming the pixel value increment profile using the following relationship:

$$\text{pixcor}(i,j)=\text{Max}\,[\text{pixinc}(i)]+\text{base}(i)-\text{pixinc}(i,j), \quad (4)$$

where $\text{pixcor}(i,j)$ was the transformed pixel value increment, $\text{base}(i)$ was the minimum pixel value increment on the ith normal and was obtained by averaging the pixel value increments over the last ten points inside the breast along the ith normal, $\text{Max}\,[\text{pixinc}(i)]$ was the maximum pixel value increment on the ith normal, and $\text{pixinc}(i,j)$ was the pixel value increment at the jth point along the ith normal.

The correlation coefficient between the pixel value profile and the transformed pixel value increment profile was defined as

$$\text{corf}(i)=\frac{\Sigma_j(\text{pix}(i,j)-\text{mpix}(i))(\text{pixcor}(i,j)-\text{mpixcor}(i))}{[\Sigma_j(\text{pix}(i,j)-\text{mpix}(i))^2]^{1/2}[\Sigma_j(\text{pixcor}(i,j)-\text{mpixcor}(i))^2]^{1/2}}, \quad (5)$$

where $\text{pix}(i,j)$ and $\text{mpix}(i)$ indicate the jth pixel value and the mean pixel value along the ith normal in an unfiltered image. The values $\text{pixcor}(i,j)$ and $\text{mpixcor}(i)$ are the transformed pixel value increment and the mean transformed pixel value increment, respectively, along the same ith normal. The summation j was over all 31 points along the ith normal. The correlation coefficients for all the normals in a given image were averaged and a mean correlation coefficient was obtained. This mean correlation coefficient was used as the FoM that quantified the match between the filter and the breast image. A good match between the transformed pixel value increment profile and the pixel value profile in the original image would result in an FoM close to 1.

To study the sensitivity of the FoM to misalignment artifacts in an equalized image, we simulated some situations of misalignment by displacing the filter either laterally or transversely. The simulated filter was displaced from its optimal position (Sec. II D) by 2, 4, and 6 mm) in either direction, and the corresponding equalized images were generated. By inspecting the changes in the FoM and the misalignment artifacts on the equalized images at different amounts of filter displacement, we could judge if the FoM could be corre-

(a)

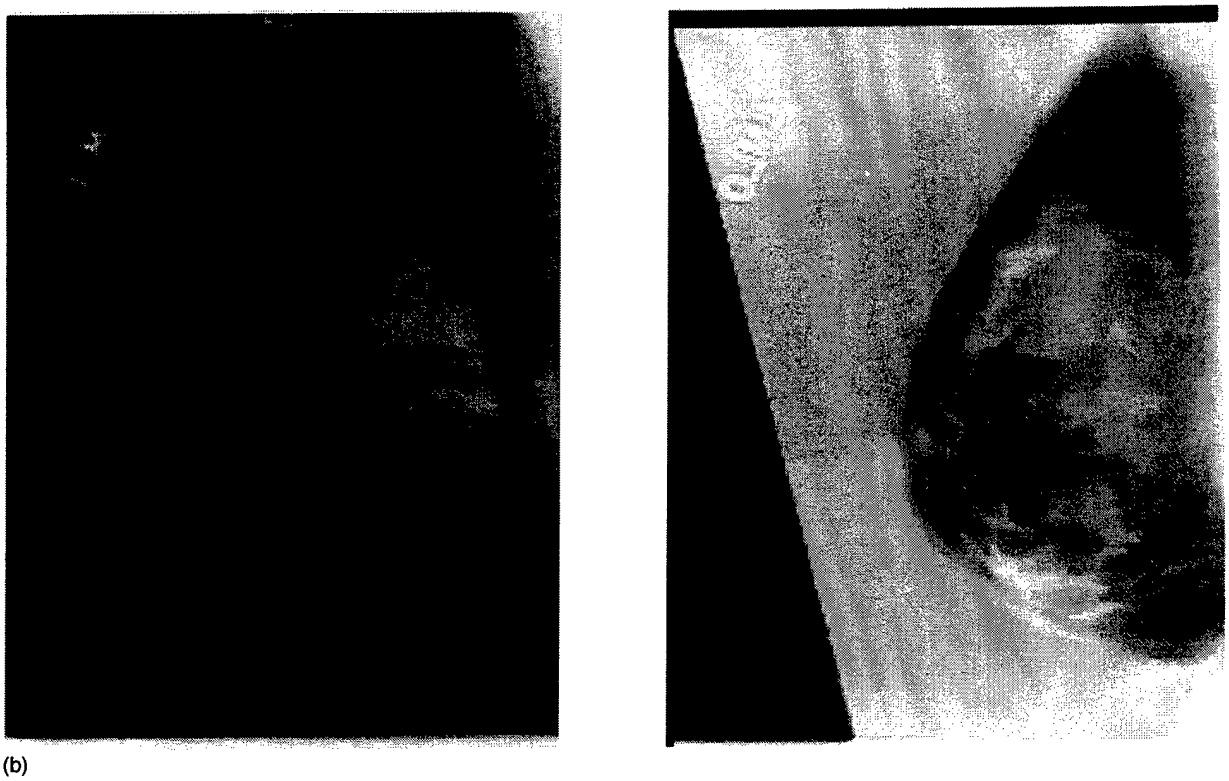

(b)

FIG. 6. Examples of (a) unequalized and equalized CC view images and (b) unequalized and equalized MLO view images.

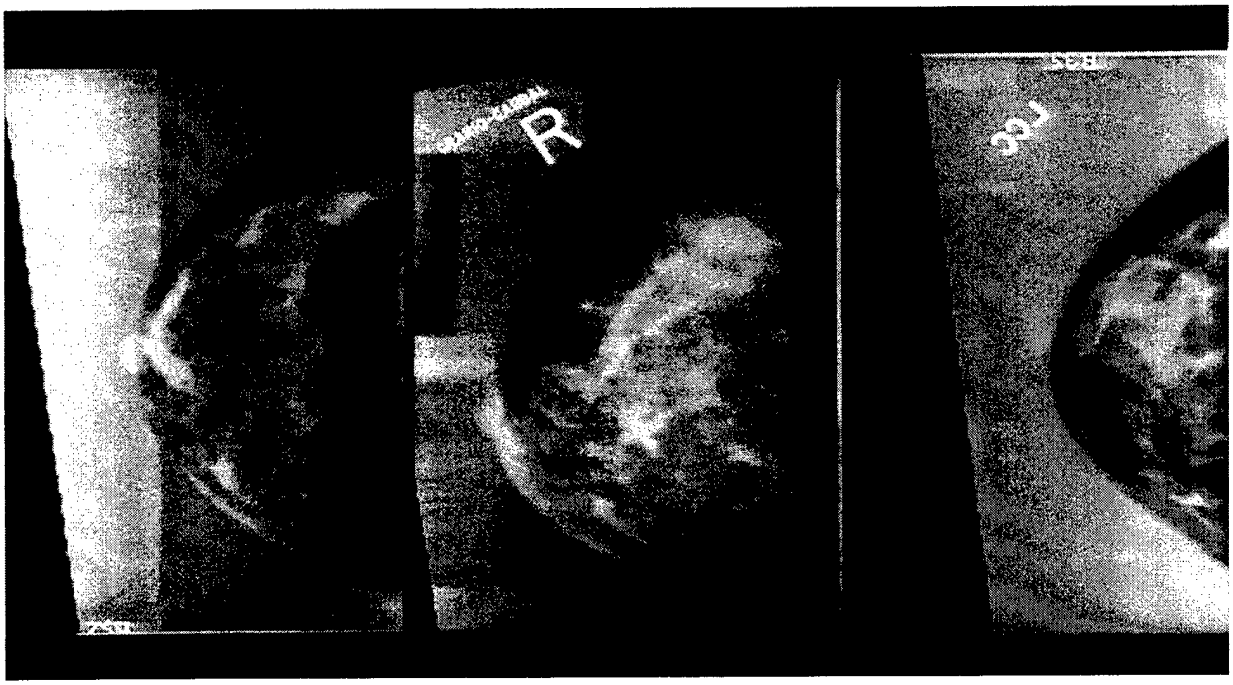

(a)

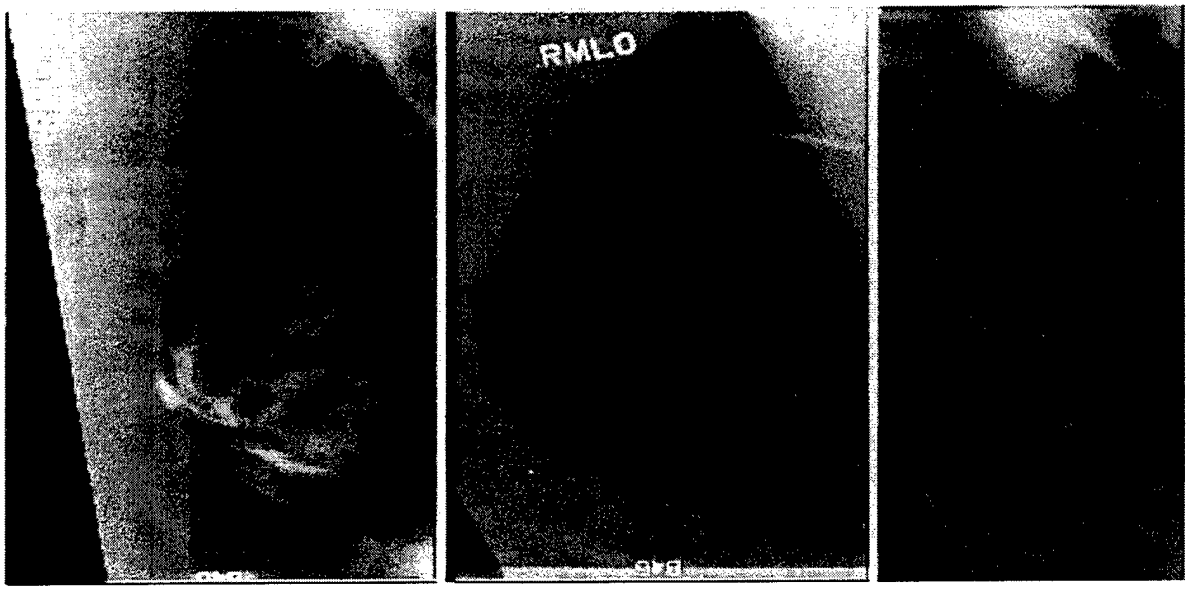

(b)

FIG. 7. A set of (a) CC view and (b) MLO view images obtained using external exposure equalization technique. These images used an average filter specific to their group. All the CC view images are from the same group. Similarly, all the MLO view images belonged to a single group.

lated with the goodness of filter alignment. We also analyzed the histogram of the FoMs for the CC view and MLO view group of images at ±2 mm filter displacements. This analysis provided an estimate of the tolerance requirement for the construction of an automated filter alignment device.

F. Observer study

The misalignment analysis described above provided a mathematical relationship for evaluating the match between the filter profile and the exposure profiles at the breast periphery; however, it did not consider some of the subjective image quality preferences of a human observer.

To test the effectiveness of the filter, 60 images from the CC view group were randomly selected and were viewed by an experienced radiologist. The quality of the equalized image was ranked between 1 and 5. A quality rating of 1 represented an image that was significantly degraded by artifacts caused by equalization, and a quality rating of 5 represented an image that exhibited near perfect equalization. The radiologist also rated the breast densities in terms of the ACR-BIRADS categories 1 to 4, where 1 signified almostentirely fatty and 4 signified extremely dense.

G. Preliminary phantom experiment

To demonstrate the effect of an external filter, we built two types of filters and obtained equalized images of a breast phantom. A 4.5 cm CIRS (CIRS, Inc., Norfolk, VA) phantom of 50% glandular and 50% adipose composition was chosen to represent an average compressed breast.

The first type of filter was a liquid filter. It consisted of a handcrafted Styrofoam mold and a container filled with saline (≈3% of NaCl by weight). The size of the Styrofoam mold was calculated by minifying a full scale drawing of the CIRS phantom. A geometric minification factor of 3 was assumed for this calculation. Two paper templates with different minification factors were made to represent the top and the bottom surfaces of the filter mold. These two pieces were pasted on to an approximately 2 cm thick Styrofoam sheet and the filter mold was then carved out using the paper templates as a guide. When the container was filled, the thickness of water was 2 cm outside the mold and it gradually decreased to less than 1 mm over the top of the mold. Care was taken to make sure that the liquid layer over the mold covered the entire field of view. This design ensured that there was minimal beam hardening over the central region of the breast and there were no artifacts due to a discontinuity of the liquid filter material at the breast boundary.

The second type of filter was a solid filter. It consisted of a piece of Teflon attached to a thin Plexiglas plate. The Plexiglas plate was used to protect the thin edge of the Teflon filter. The solid Teflon piece was machined using a computer-controlled mill to a wedge shape that approximated an equalization filter. The Teflon filter is a 5 cm wide rectangular strip that has a maximum thickness of 1.8 cm. As a prototype, it was not fabricated to match a breast shape in the X-Y plane.

For each filter, the filter-to-phantom distance and the filter orientation were adjusted manually to obtain the best alignment between the filter and the breast phantom to acquire an exposure-equalized image.

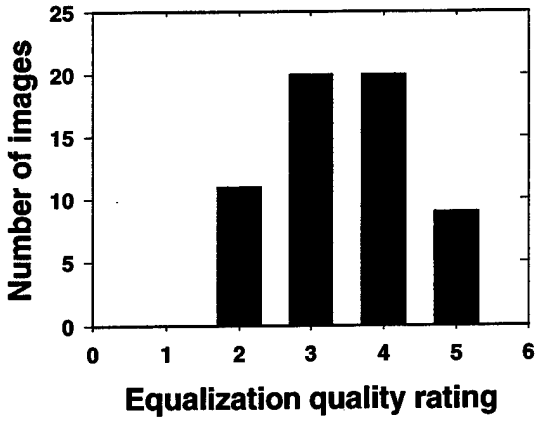

FIG. 8. Distribution of equalization quality ratings for 60 equalized images, evaluated by an experienced breast radiologist.

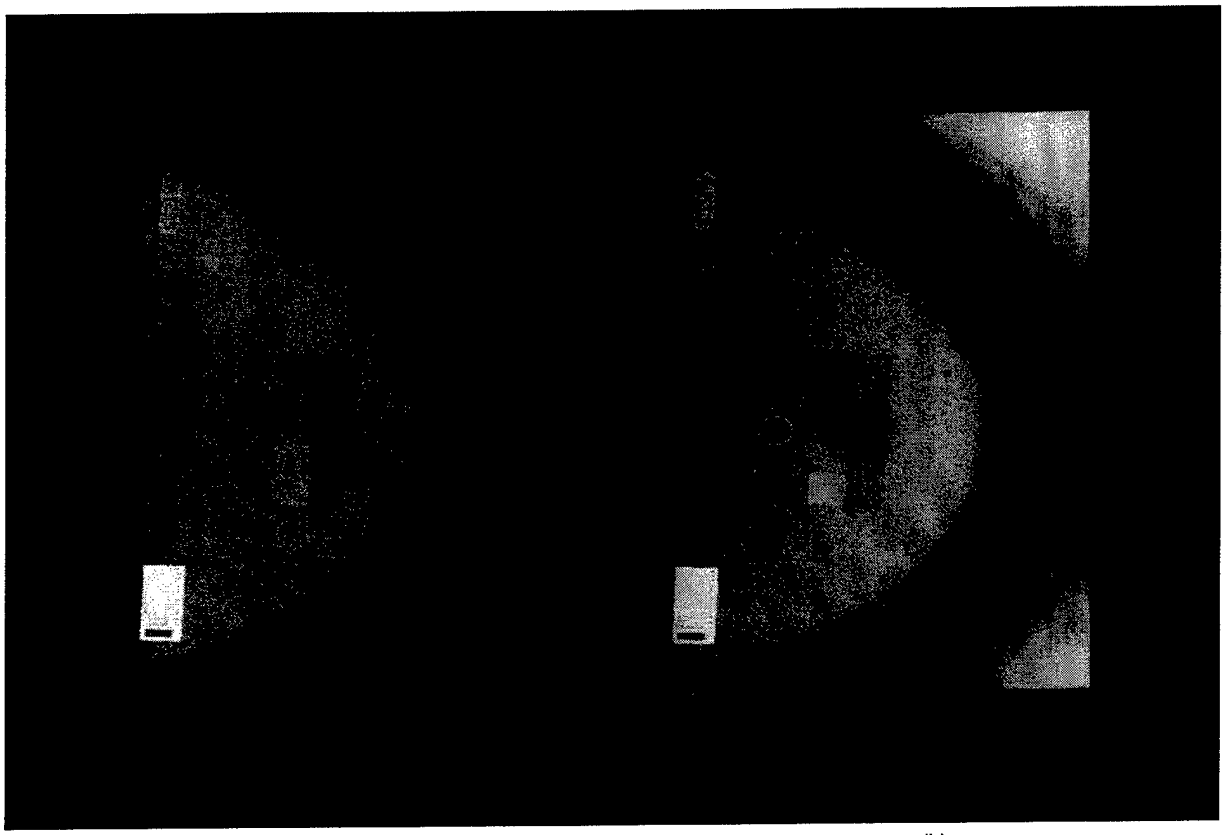

FIG. 9. The CIRS phantom image (a) unequalized and (b) equalized with a liquid filter.

FIG. 10. The CIRS phantom image (a) unequalized and (b) equalized with a solid filter made with Teflon. A piece of silly putty was placed on top of the phantom to simulate dense breast parenchyma and calcium carbonate specks were placed at the periphery. The visibility of the peripheral region of the dense parenchyma and of the breast phantom is improved by equalization.

III. RESULTS

A. Simulation study

The digitized mammograms in the CC and MLO views were each classified into three groups.[16] To have reasonable statistics, we chose the largest group in each view as case samples for our simulation study. The selected CC view group contained 196 images and the MLO view group contained 171 images. For each of these groups, we estimated the mean exposure range as the ratio of the maximum to the minimum exposures along the average relative exposure profile (described in Sec. II C). These exposure ranges were found to be 5.46:1 and 5.18:1 for CC and MLO views, respectively. These exposure ranges are lower than what we would expect for breast images and will be discussed further in the Sec. IV. Using the average exposure reduction factor array and the steps described in Sec. II D, the pixel value increment array and the equalized image were computed for each mammogram in the group. Figure 6 shows examples of the unequalized and equalized images from the CC and the MLO groups. Figure 7 shows additional examples of equalized images from the CC and MLO view groups.

B. Observer study

A histogram of the equalization quality rating by the radiologist is shown in Fig. 8. It can be seen that about 81% of the images had ratings greater than or equal to 3. The radiologist rated 6 images to be in ACR-BIRADS breast density category 1, 31 to be in category 2, 16 to be in category 3, and 7 to be in category 4.

C. Preliminary phantom experiment

The images of the CIRS phantom before and after equalization with saline as a filter material are shown in Fig. 9. It can be seen that the filter equalized the periphery region around the nipple reasonably well. However, the filter undercompensated the periphery in the upper and lower parts of the image. This was probably caused by the mismatch between the filter boundary and the breast border in these regions because the shape of the handcrafted mold did not match very well with the breast phantom shape in the X-Y plane. The 0.4-cm-thick fatty skin layer in the CIRS phantom is clearly visible in the equalized image near the nipple region. Some dark spots seen in this image were due to air bubbles entrapped near the mold.

Images of the CIRS phantom before and after equalization with the Teflon filter are shown in Fig. 10. A piece of silly putty was added on the phantom to simulate dense parenchyma in a breast. The filter strip was oriented approximately in the 4 o'clock direction in the equalized image. The fatty skin layer in the CIRS phantom and some calcium car-

TABLE I. The effect of 2 mm filter displacement on the FoM for the CC and MLO view images.

Filter displacement	CC view group		MLO view group	
	Mean FoM	% of Images FoM≤0.8	Mean FoM	% of Images FoM≤0.8
0 mm[a]	0.89	6%	0.85	19%
Transverse +2 mm	0.87	12%	0.83	29%
Transverse −2 mm	0.90	8%	0.86	16%
Lateral +2 mm	0.88	12%	0.84	24%
Lateral −2 mm	0.90	5%	0.85	16%

[a]Filter location determined by minimum rms criterion.

bonate specks placed near the periphery are clearly visible in the region equalized by Teflon filter. The contrast of the edge of the simulated dense parenchymal region is also greater in the equalized part of the image.

D. Misalignment analysis

Histograms of the FoMs for the CC and MLO view images at the optimal filter position are plotted in Fig. 11. It can be seen that the mean FoM for the group of CC view images was 0.89 and over 93% of the images had FoMs greater than 0.8. Only 12 of the 196 images had FoMs less than or equal to 0.8 and the minimum FoM was 0.72. Similarly, for the group of MLO view images the mean FoM was 0.85 and about 81% of the images had FoMs greater than 0.8. Only 33 of the 171 MLO images had FoMs less than or equal to 0.8. Thus, the average filter shape matched well with over 80% of the images in a given group.

The distribution of the FoMs at ±2 mm filter displacement was also analyzed. The mean FoM and the percentages of images that had FoM values less than or equal to 0.8 are tabulated in Table I. Equalized images with 0 mm and ±6 mm displacements of the filter in the lateral and transverse directions are shown in Fig. 12. The FoMs that were calculated for each image are also shown. For this example, the rms difference between the breast border and the filter border at the "optimal" alignment position (0,0) was 2.13 mm and the FoM was 0.89. There is a dark boundary around the upper section of the breast border due to the slight misalignment as indicated by the rms error. Displacing the filter by 2 mm in the negative lateral direction (not shown in Fig. 12) reduced the dark rim in the upper border section to lower OD and the FoM increased to 0.90. As the filter was displaced transversely away from breast, the FoM reduced to 0.87, 0.82, and 0.77 for 2, 4, and 6 mm displacements, respectively. The OD along the breast periphery increased as the transverse displacement increased positively, indicating increasing under-compensation by the filter. On the other hand, when the filter was displaced in the negative transverse direction, the breast periphery became increasingly over-compensated and the FoM reduced to 0.86, 0.84, and 0.79 for 2, 4, and 6 mm displacements, respectively. Except for the −2 mm displacement discussed above, a similar reduction in FoM was also observed for filter displacements along the lateral direction. This example illustrates the effectiveness of the correlation coefficient in quantifying the degree of misalignment.

IV. DISCUSSION

A. Effectiveness of external exposure equalization method

It can be seen in Fig. 6 that the equalization along the breast periphery is very good in these examples, despite the fact that the filter was designed by using an average exposure profile for a given breast shape class. It can also be seen from Fig. 7 that although the sizes and shapes of the breasts varied over a wide range, the average filter was effective in equalizing these images without obvious artifacts. Digitizer artifacts due to the unbalanced sensitivity of the two CCD arrays, charge transfer, and blooming can be seen on some of the images. The digitizer artifacts are specific to this simulation study and will not exist in an actual equalization pro-

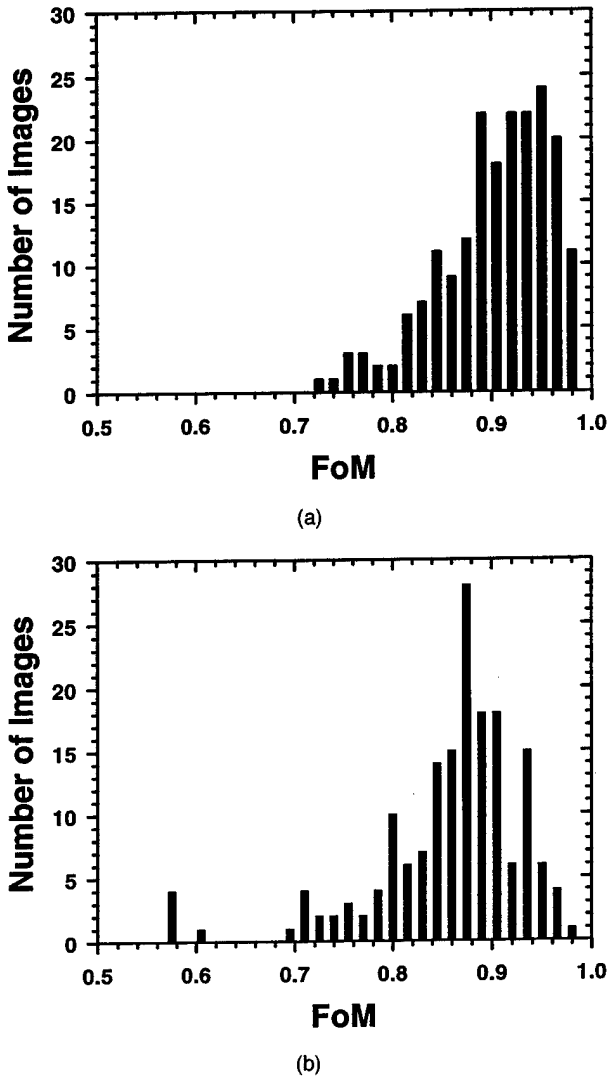

FIG. 11. Distribution of the Figure-of-Merit for the group of (a) CC view and (b) MLO view images.

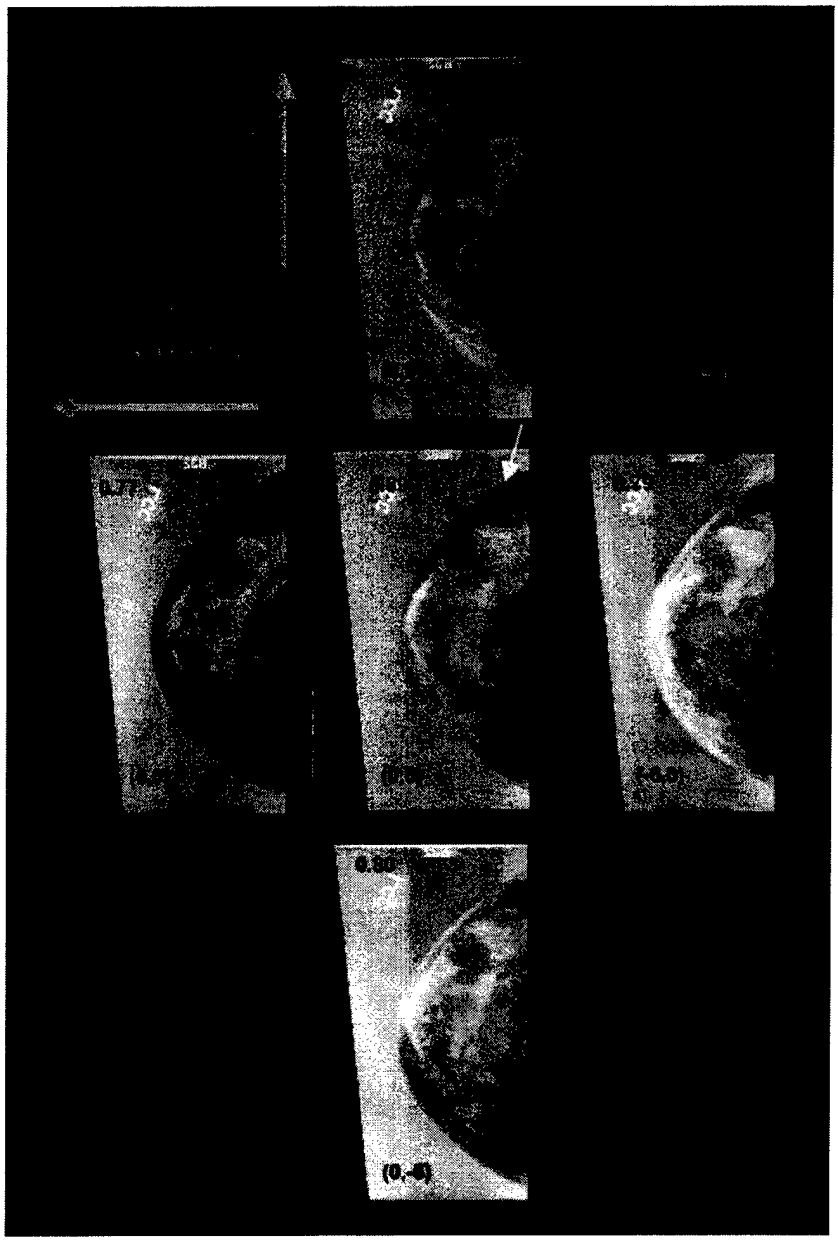

FIG. 12. Effect of filter misalignment on the FoM. The dark areas seen along the breast periphery are due to under-compensation whereas the lighter areas are due to over-compensation. The numbers in parentheses indicate the filter displacements and the numbers at the upper left corner are the corresponding FoM values.

cess. These examples illustrate that a small number of external filters can be designed to provide effective equalization at the breast periphery for breasts in a given mammographic view.

B. Misalignment and filter positioner design

The results in Table I indicate that a 2 mm displacement did not reduce the FoM substantially for the CC view images. The fraction of CC images with FoMs greater than 0.8 was over 88% for 2 mm displacements in all directions. For the MLO view images, the mean FoM for 2 mm displacements in all directions was still greater than 0.8. However, the fraction of images with FoMs greater than 0.8 decreased to a minimum of 71%. Because the shapes of MLO images are more complicated than CC view images, the simple polynomial used for the filter shape probably cannot tolerate misalignment as well as in a CC view. This may have to be improved through shaping of the filter thickness profile so that less equalization is performed at the pectoral muscle and lower breast regions, or through a more complicated filter shape. The latter approach may increase the number of filters required for the MLO view.

From the filter displacement simulation, we estimated that a misalignment of up to 2 mm between the filter edge and breast boundary is tolerable for the CC view. However, for the MLO view, the misalignment may have to be less than 1 mm. Because the simulation study used digitized mammograms and an analytical filter, the misalignment occurred in the image plane. In actual implementation the filter will be about 20 cm from the focal spot. With such a geometry, the 1 mm corresponds to about 0.3 mm in the filter plane. Such a tolerance is achievable through commercially available X-Y translators. Moreover, placement of the filter 20 cm from the focal spot will result in significant geometric blur of

the projected filter shape, which should further relax the requirements for filter alignment. Thus, we expect that it will be feasible to build an automatic filter selection and alignment system economically.

C. Observer study

Although the data set used in this observer study was small, the radiologist's quality ratings (Fig. 8) demonstrate that the image quality for most of the equalized images was greater than or equal to 3, which can be considered acceptable. The average quality rating was 3.3 for images in breast density categories 1 and 2, and it was 4.1 for images in breast density categories 3 and 4. The lower average quality rating for the images with lower breast density is probably caused by the fact that they are more likely to be over-compensated by the average filter. This is consistent with the radiologist's comments after the observer study that (1) slight under-compensation and images with a dark rim are in general preferred, (2) any over-compensation and equalized breast images with a low-OD boundary are undesirable, and (3) small fatty breasts do not require equalization.

D. Discrepancy in the estimated exposure dynamic range of breast images

The average exposure range values presented earlier were lower than an expected range of 20:1 for a typical mammogram. To understand this discrepancy, histograms of maximum exposure ranges in each image for the CC and MLO view image groups were generated. The maximum exposure range in an image was estimated as the ratio of the maximum to the minimum exposures among all exposure profiles along a set of normals in that image. The histograms of the maximum exposure ranges are shown in Fig. 13. The mean values for the CC and MLO view histograms are 10.24 and 9.97, respectively, which are still lower than the expected dynamic ranges of breast images. A major reason for the underestimation of the exposure range in the digitized mammogram is the inability of the film digitizer to digitize accurately in the high-OD region. The OD-to-pixel value calibration curve of the digitizer leveled off at about 3.6 OD, whereas the maximum OD of mammography film can be greater than 4. Any OD above 3.6 essentially was digitized to about the same pixel value. The OD converted from a pixel value in the breast periphery therefore could be greatly underestimated. This problem was further amplified by the small gradient in the shoulder region of the H&D curve; a small error in OD corresponded to a large error in relative exposure. Another reason for the small exposure range from our estimation is that searching for the minimum exposure along the selected normals did not guarantee that the densest region in the breast image would be found. The extreme dynamic range of breast images is usually estimated from the densest region (OD near fog and base level) relative to the maximum exposure outside the breast region.

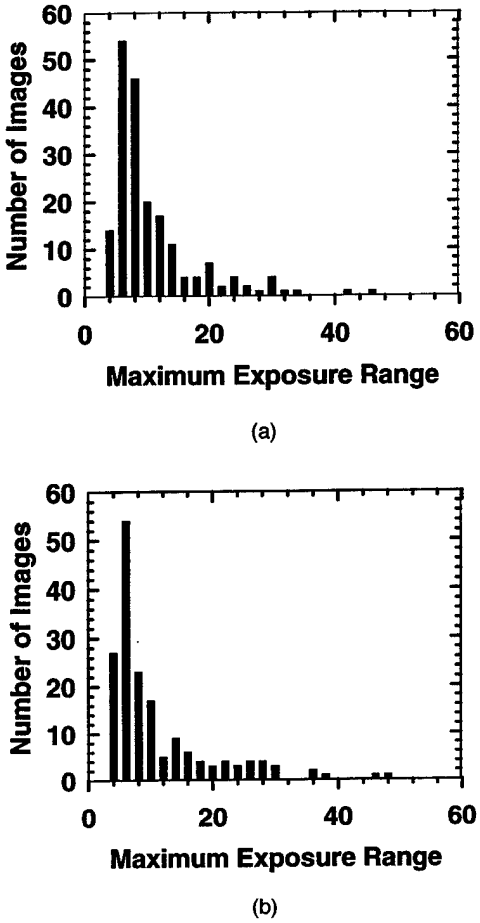

FIG. 13. Histogram of maximum exposure range for the group of (a) CC view and (b) MLO view images.

E. Drawbacks of the external exposure equalization method

The equalization filter may cause artifacts on some images. These artifacts are mainly due to mismatches between the equalization filter and the breast.

Part of the edge or the entire edge may appear brighter than the surroundings. This is an artifact of over-compensation, which arises when part of the filter or the entire filter extends too far into the breast and/or the slope of the filter is greater than that needed to compensate for the exposure gradient at the periphery of the breast. Over-compensation may result in contrast reduction because of the low gradient in the toe region of the H&D curve.

A dark rim or dark areas may appear around the breast. This is an artifact caused by under-compensation. It arises when part of the filter or the entire filter is positioned too far outside the breast or when the slope of the filter is less than that needed to compensate for the exposure gradient at the periphery of a particular breast. Under-compensation is likely to be more acceptable to radiologists because the breast periphery is improved even if it is not completely equalized. This is confirmed by the impression of the radi-

(a)

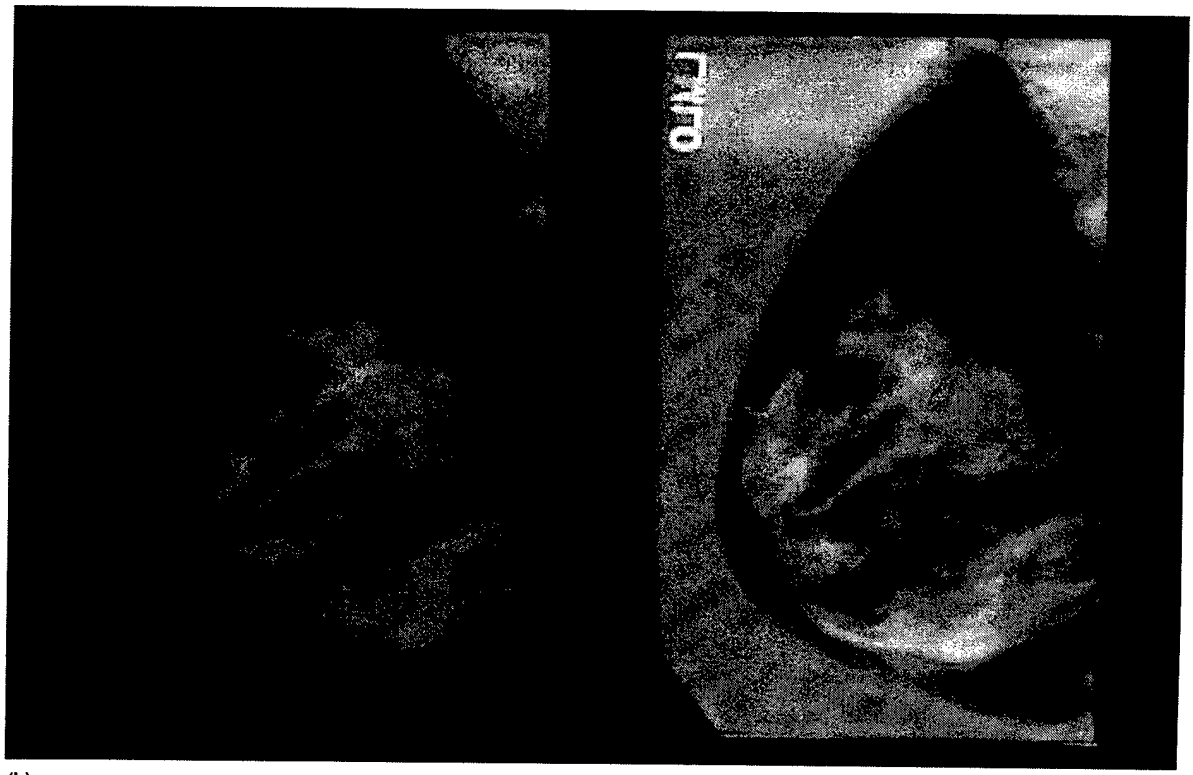

(b)

FIG. 14. Example of images with artifacts: (a) unequalized CC view image (left) and equalized image with under-compensation artifact (right) in the upper portion and below the nipple and (b) unequalized MLO view image (left) and equalized image with over-compensation artifact (right) in the lower portion of the breast periphery.

ologist who evaluated the equalized images in the observer study.

Figure 14 shows examples of images from the CC and MLO groups that demonstrate some of these artifacts.

One problem revealed by the simulation study of the equalization system is that a single filter thickness for all breasts in one group may not be adequate. It is known that breast density and thickness do change the amount of exposure compensation required for equalization. The rightmost image in Fig. 7(a) shows that the image background is brighter than the breast, indicating that the filter was thicker than that needed for this breast. The rightmost image in Fig. 7(b) shows an under-compensated image with a background darker than the breast, which indicates that the filter was thinner than that needed for this breast. In actual implementation, the mismatch due to breast thickness can be reduced by building three filters with different thicknesses for each breast shape group; one of these filters may be selected depending on the breast thickness. A criterion can also be set so that no equalization will be used for breasts thinner than a threshold thickness. Although the number of filters will increase by threefold, the total number of filters is still reasonably small and may be acceptable.

For this simulation study, we used a single exposure profile to generate the filter profile along the entire breast border. It can be seen from Fig. 7(b) that, in equalized MLO view images, the pectoral muscle regions are generally overcompensated relative to the breast region. This result indicates that a uniform filter profile along the entire breast border is not a good approximation for the MLO view images. A solution to this problem may be making the filter thickness gradually taper off in the pectoral muscle region for the MLO groups.

F. Implementation of an exposure equalization system

The simulation study used a digitized mammogram as the input image. However, in actual implementation a digital video image of the compressed breast will be used for selection and alignment of the filter. A color video image of the compressed breast can be acquired with a dark green background to facilitate segmentation and breast shape classification. Experiments in our laboratory have shown that compressed body parts have a higher red component. A red component image of the compressed breast can be segmented easily from a dark green background by simple thresholding. The breast shape as determined from the segmented boundary may need corrections for potential differences in the geometry of the video and x-ray images. The algorithms developed here for the simulation study can then be used for breast shape classification, filter selection, and alignment of the filter with the breast boundary.

V. CONCLUSIONS

We have demonstrated the effectiveness of an exposure equalization technique for mammographic imaging using a small set of near patient-specific external filters. Through a computer simulation study on a large set of digitized CC and MLO view breast images, it is shown that an average filter for a group of breasts with a similar shape can be designed using a polynomial to represent the breast shape and an average exposure profile to derive the filter thickness profile. This average filter is effective in providing exposure equalization without significant misalignment artifacts for approximately 80% of the images used in this study. Additionally, it is shown that slight misalignment of the filter is tolerable.

A preliminary phantom study using handcrafted filters indicates that it is feasible to fabricate an external exposure equalization filter using either a solid filter material or a negative mold with a liquid filter material.

ACKNOWLEDGMENTS

This work was supported by Grant No. DAMD 17-94-J-4292 from the U. S. Army Medical Research and Material Command. The content of this publication does not necessarily reflect the position of the government and no official endorsement of any equipment and product of any companies mentioned in the publication should be inferred.

[a]Electronic mail: chanhp@umich.edu

[1]E. L. Gingold, X. Wu, and G. T. Barnes, "Contrast and Dose with Mo-Mo, Mo-Rh, and Rh-Rh target-filter combinations in mammography," Radiology **195**, 639–644 (1995).

[2]A. Maidment, R. Fahrig, and M. J. Yaffe, "Dynamic range requirements in digital mammography," Med. Phys. **20**, 1621–1633 (1993).

[3]P. C. Bunch, K. E. Huff, and R. Van Metter, "Analysis of detective quantum efficiency of radiographic screen/film system," J. Opt. Soc. Am. A **4**, 902–909 (1987).

[4]A. Stacey-Clear, K. A. McCarthy, D. A. Hall, E. P. Spellman, G. White, C. A. Hulka, G. J. Whitman, E. F. Halpern, and D. B. Kopans, "Mammographically detected breast cancer in women under 50 years old," Radiology **186**, 677–680 (1993).

[5]H. R. Blackwell, "Contrast thresholds of the human eye," J. Opt. Soc. Am. **36**, 624–643 (1946).

[6]B. Baxter, H. Ravindra, and R. A. Normann, "Changes in lesion detectability caused by light adaptation in retinal photo-receptors," Invest. Radiol. **17**, 394–401 (1982).

[7]H. L. Snyder, "Chapter 3: The Visual System: Capabilities and limitations," in *Flat-Panel Display and CRTs*, edited by L. E. Tannas, Jr. (Van Nostrand Reinhold, New York, 1985).

[8]K. L. Lam and H. P. Chan, "Development of x-ray beam equalization technique in mammography," Radiology **169(P)**, 338 (1988).

[9]K. L. Lam and H. P. Chan, "Exposure equalization technique in mammography," Invest. Radiol. **24**, 154–156 (1989).

[10]K. L. Lam and H. P. Chan, "Effects of x-ray beam equalization on mammography imaging," Med. Phys. **17**, 242–249 (1990).

[11]G. Panayiotakis, H. Likaki, Z. Kolitsi, and J. Dimipoulos, "An anatomical filter for exposure equalization in mammography," Radiology **15**, 15–17 (1992).

[12]J. M. Sabol, I. C. Soutar, and D. B. Plewes, "Mammographic scanning equalization radiography," Med. Phys. **20**, 1505–1515 (1993).

[13]J. W. Oestmann, B. Stoel, H. Schrijvershof, J. Vrooman, and L. J. Schultze Kool, "Scanning equalization mammography: Preliminary evaluation," Radio Graphics **14**, 123–128 (1994).

[14]J. M. Sabol, I. C. Soutar, and D. B. Plewes, "Practical application of a scan-rotate equalization geometry to mammography," Med. Phys. **23**, 1987–1996 (1996).

[15]J. W. Byng, J. P. Critten, and M. J. Yaffe, "Thickness-equalization processing for mammography images," Radiology **203**, 564–568 (1997).

[16]M. M. Goodsitt, H. P. Chan, B. Liu, A. R. Morton, S. V. Guru, S. Keshavmurthy, and N. Petrick, "Classification of compressed breast shape or the design of equalization filters in mammography," Med. Phys. **25**,

937–948 (1998).
[17]J. M. Boone, I. Duryea, and R. M. Steiner, "Filter wheel equalization for chest radiography: A computer simulation," Med. Phys. **22**, 1029–1037 (1995).
[18]A. R. Morton, H. P. Chan, and M. M. Goodsitt, "Automated model-guided breast segmentation algorithm," Med. Phys. **23**, 1107–1108 (1996).
[19]D. R. Dance, J. Persliden, and G. A. Carlsson, "Calculation of dose and contrast for two mammography grids," Phys. Med. Biol. **37**, 235–245 (1992).
[20]M. J. Berger and J. H. Hubbell, *XCOM: Photon cross sections on a personal computer*, US Department of Commerce, National Bureau of Standards, Gaithersburg, MD, NBSIR 87-3597 (1987).
[21]H. E. Johns and J. R. Cunningham, *The Physics of Radiology*, 4th ed. (Thomas, Springfield, IL, 1983).
[22]R. J. Jennings, "Spectral simulation and photon design program suite," FDA, Rockville, MD 20857 (1993).
[23]W. E. Moore, Estimated sensitometric data for Kodak Min-RE film, personal communication, Eastman Kodak Company, Rochester, NY (1995).

Investigation of the line-pair pattern method for evaluating mammographic focal spot performance

Mitchell M. Goodsitt,[a] Heang-Ping Chan, and Bob Liu
Department of Radiology, University of Michigan, Ann Arbor, Michigan 48109-0030

(Received 20 May 1996; accepted for publication 25 October 1996)

The latest American College of Radiology (ACR) Mammography Quality Control Manual contains a new method for evaluating focal spot performance, which this paper refers to as the "line-pair pattern test." The ACR describes a variety of methods for performing this test, and does not advocate one method over another. The authors of this paper conducted an investigation to compare the optional ways for performing the test. Resolution measurements were obtained using a prototype line-pair resolution phantom imaged with a GE DMR mammography unit. Measurements were made with the line-pair pattern 4.5 cm above the breast support platforms in both conventional (contact) and magnification geometries. Both 4.5 cm of air and Lucite were tested as attenuators between the line-pair pattern and the breast support platform. Image receptors that were employed included film alone, screen-film, and screen-film that was not allowed to wait the recommended 15 min before exposure. kVp was varied as was the orientation of the line-pair pattern relative to the chest wall. For the air attenuator case, the screen degraded the measured resolution by 1–3 lp/mm when compared to the direct film. The Lucite attenuator reduced the resolution by an additional 1 lp/mm. Increasing kVp improved the resolution slightly for the conventional mode, but decreased it slightly for the magnification mode. Based upon the results of this study, recommendations are made for improving the test protocol. For a test of focal spot performance, one should use the no-attenuation with direct film detector setup. For a measure of the resolution of the entire imaging chain, one should use the Lucite attenuator with screen-film detector setup. © *1997 American Association of Physicists in Medicine.* [S0094-2405(97)01001-8]

Key words: mammographic resolution, focal spot, quality control

I. INTRODUCTION

The latest edition of the American College of Radiology (ACR) Mammography Quality Control (QC) Manual[1] contains a description of a new method for routine evaluation of focal spot performance in mammographic units. This method determines "limiting resolution" in units of line pair per millimeter (lp/mm) rather than effective focal spot size in millimeters, which is determined with the other (slit camera) method described in the manual. The ACR refers to the new method as a "high-contrast resolution pattern" method and recommends that either a bar pattern, star pattern or wedge pattern be employed as the test tool. Since most implementations of this method involve bar or line-pair patterns, we will refer to it as the "line-pair" method in this paper. The ACR recommends that both the line-pair and slit camera methods be employed for acceptance testing of new mammography units, and the line-pair method alone be used for routine (e.g., annual) QC tests. If a system fails the routine QC test, the ACR suggests performing a more detailed investigation using the slit camera method. Although the motivation for recommending the new focal spot test is not discussed in the manual, it is obvious that the ACR desires a test that is easier to perform and more directly related to the spatial resolution observed in clinical images.

The ACR recommends that a high-resolution bar pattern be employed for the line-pair test, specifically, one extending to about 20 lp/mm. This pattern is placed 4.5 cm above the breast support plate, centered laterally and positioned within 1 cm of the chest wall edge of the imaging receptor. The pattern is imaged with the bars both parallel and perpendicular to the anode–cathode axis of the x-ray tube. The ACR describes several optional setups for performing the line-pair resolution test. These include: (1) either no material (except air) or a 4.5-cm-thick homogeneous attenuator (e.g., Lucite) being placed between the pattern and the breast support plate, and (2) either screen-film or direct film (e.g., a ready pack) being employed as the detector.

The purpose of our study was to compare the results for a variety of the possible attenuator–detector combinations. Other studies on the effects of intensity distribution, position, kVp/mA and screen-film contact on mammographic focal spot measurements have been reported in the literature,[2–4] but none have specifically analyzed the line-pair pattern methods recommended by the ACR.

II. MATERIALS AND METHODS

The test tool we employed was a prototype manufactured by Computerized Imaging Reference Systems (CIRS, Inc., Norfolk, VA). It has a solid Lucite base with a slider/pattern holder on the top surface. The slider can either be positioned directly above the Lucite base to achieve the 4.5-cm-thick homogeneous attenuator condition, or be extended out from the base (i.e., cantilevered) to achieve the "no attenuator" condition, with the pattern held securely 4.5 cm above the

breast support plate. The line-pair pattern itself is made of gold and contains individual segments having resolutions of 5, 8, 10, 11, 12, 13, 14, 15, 16, 17, 18, 19 and 20 lp/mm. The length of the pattern from the 5 lp/mm end to the 20 lp/mm end is 1.8 cm. The pattern is encased in a thin plastic piece that fits within a recessed well in the slider, permitting the pattern to be positioned either with the bars parallel or perpendicular to the x-ray tube anode–cathode axis.

All tests were performed on a General Electric (Milwaukee, WI) model DMR mammography x-ray unit in our clinic. This unit has nominal focal spot sizes of 0.1 and 0.3 mm. It was operated only in the molybdenum target, molybdenum filter mode for this study. Using 0.5° and 1.0° star patterns within a GE supplied holder that positions the patterns along the appropriate reference axes of the mammography unit, we measured the large and small focal spot dimensions to be 0.42 mm×0.33 mm and 0.09 mm×0.06 mm, respectively, where the first dimension represents the width and the second, the length of the focal spot.

The screen-film detector was Kodak (Rochester, NY) Min-R/Min-R E. To ensure that the same imaging geometry (specifically focus-to-film distance) was employed for both the screen-film and direct film detector situations in our study, we chose not to use a "ready pack" as the direct film detector. Instead, we used an identical screen-film cassette, but blocked virtually all screen light by placing a totally black film between the screen and the Min-R film that was used as the detector. The latter film was placed emulsion side up (facing the x-ray tube) to further reduce any effects of the screen light. The "totally black film" was obtained by developing a Min-R E film that we purposely exposed to direct light. Its measured optical density was 4.39; hence its visible light transmission was about 0.004%.

To begin the study, we placed the line-pair pattern directly on top of a screen-film cassette that was placed on the breast support plate and made an exposure (the technique was 26 kVp, 5 mAs, 0.5 mm aluminum additional filtration). The developed film provided us with the limiting resolution of the screen-film system by itself (no effect of the focal spot).

We then proceeded to perform the line-pair pattern test under a variety of possible conditions described in the ACR manual. For conventional (contact) geometry (0.3 mm focal spot, line-pair pattern 4.5 cm above the cassette holder/breast support plate), these included tests with no attenuator (air) between the pattern and breast support plate and both direct film and screen-film as the detectors, and tests with 4.5 cm of Lucite between the pattern and the breast support plate with a screen-film as the detector. For the latter test, the Bucky (grid) cassette holder was employed; whereas, for the tests with no attenuator, the gridless magnification cassette holder was employed. For 1.8× magnification geometry, the line-pair pattern was placed 4.5 cm above the magnification stand/breast support platform, and tests were performed using the no-attenuator with direct film combination and using the Lucite with screen-film combination. The gridless cassette holder was employed for all magnification techniques. Tests using the Lucite with direct film combination were not performed for either the contact or the magnification geometry cases because of the excessive exposure times that would have been required. Finally, for the no-attenuator with screen-film cases, we found it necessary to add a 0.1 mm aluminum filter to the beam in order to achieve the desired film optical density at minimal x-ray system mAs. This additional filtration was taped to the collimator to minimize the influence of the resulting x-ray scatter.

The same screen-film cassette was employed for all screen-film detector images, and each time the film was loaded, we waited at least 15 min before making the exposure in order to permit any entrapped air between the film and screen to escape.

The majority of the exposures were made at 26 kVp which is a typical x-ray tube potential used for imaging an average breast in our clinic. The ACR recommends the use of such a tube potential for the test. The mAs was adjusted to obtain films with background optical densities (in the region just outside the image of the line-pair pattern) in the 1.2–1.6 o.d. range suggested in the ACR manual.

Several additional comparison images were also obtained at tube potentials of 22 and 30 kVp to determine the influence of kVp on the measured resolution. Also a limited study was performed in which radiographs were produced without waiting 15 min between loading the film in the cassette and making the exposure to examine what effect this might have on the measured resolution.

In performing the tests, measurements were made with the bars of the line-pair pattern both parallel and perpendicular to the anode–cathode axis of the x-ray tube. In most cases, when the bars were perpendicular to the anode–cathode axis, the bar pattern was oriented such that the 20 lp/mm end was closest to the chest wall. To determine the influence of pattern position on spatial resolution, a limited series of tests were also performed in which, instead, the 5 lp/mm end was closest to the chest wall.

Three medical physicists (the authors of this paper) reviewed the images of the bar patterns with 7× and 30× magnifying lenses, and the resolutions were determined by consensus as follows. Each physicist examined the images independently and decided upon a resolution using the ACR criterion that the lines be distinctly visible throughout at least half the bar length. In most cases the first analyses were made with the 7× magnifier, which was easier to use. The physicists then discussed their assessments, and if there were differences, the images were reexamined with the 7× and 30× magnifiers. The results were discussed further and a resolution was decided upon that was agreeable to all. The maximum difference between the assessments of the individual readers was 1 lp/mm, and it was felt that our decision by consensus was as effective and valid as the ACR method of averaging the individual readings.

III. RESULTS

The radiograph produced with the pattern placed directly on top of the screen-film cassette displayed 20 lp/mm resolution. The resolutions measured in the contact mode (0.3

TABLE I. Measured resolution for contact geometry using nominal 0.3 mm focal spot and 26 kVp (a plus sign implies bars very clearly discerned and limiting resolution is greater by about 0.5 lp/mm or more).

Attenuator	None (air)	None (air)	Lucite
Detector	Direct film	Screen-film	Screen-film
Use of grid	No	No	Yes
mAs	160	4 (with 0.1 mm additional Al attenuation)	160
Limiting resolution with bars parallel to anode–cathode axis	20 lp/mm	17 lp/mm	16 lp/mm
Limiting resolution with bars perpendicular to the anode–cathode axis (20 lp/mm segment within 1 cm from the chest wall)	20+ lp/mm	18 lp/mm	18 lp/mm
Limiting resolution with bars perpendicular to the anode–cathode axis (5 lp/mm segment within 1 cm from the chest wall)	20+ lp/mm	18+ lp/mm	

TABLE II. Measured resolution for 1.8 times magnification geometry using nominal 0.1 mm focal spot and 26 kVp (a plus sign implies bars very clearly discerned and limiting resolution is greater by about 0.5 lp/mm or more).

Attenuator	None (air)	None (air)	Lucite
Detector	Direct film	Screen-film	Screen-film
Use of grid	No	No	No
mAs	200	7 (with 0.1 mm additional Al attenuation)	160
Limiting resolution with bars parallel to the anode–cathode axis	20+ lp/mm	20+ lp/mm	19 lp/mm
Limiting resolution with bars perpendicular to the anode–cathode axis (20 lp/mm segment within 1 cm from chest wall)	15 lp/mm	14 lp/mm	13 lp/mm
Limiting resolution with bars perpendicular to anode–cathode axis (5 lp/mm segment within 1 cm from chest wall)		16 lp/mm	

mm focal spot) at 26 kVp are listed in Table I and those measured in the 1.8× magnification mode (0.1 mm focal spot) are listed in Table II. The mAs factors are also included in the tables. In general, the spatial resolution is best for the no-attenuator direct-film detector *test method*. The resolution degrades by 1–3 lp/mm when screen-film is used as the detector. An additional degradation of about 0.5–1 lp/mm occurs when Lucite is employed as the attenuator between the line-pair pattern and the detector. Waiting 1–2 min instead of 15 min to permit entrapped air between the film and screen to escape resulted in reduced resolution by as much as 3 lp/mm.

The measured spatial resolutions at different kVp's are listed in Table III(a) for the contact geometry and Table III(b) for the 1.8× magnification geometry. In general, we observed that the spatial resolution improved as the kVp increased for the contact geometry, but it displayed the exact opposite trend for the magnification geometry.

IV. DISCUSSION

All of the measured spatial resolutions listed in Tables I–III for the various setups exceed the minimum performance standards suggested by the ACR. For contact geometry, the minimum acceptable values are as follows: 13 lp/mm with the bars parallel to the anode–cathode axis and 11 lp/mm with the bars perpendicular to the anode–cathode axis. For magnification mode, the ACR states that the minimum resolution should be no lower than the values specified for contact geometry. It is interesting to note that for the GE DMR mammography unit in our facility, the resolution with the bars perpendicular to the anode–cathode axis is actually considerably worse in the magnification mode than in the contact geometry mode (see Tables I and II). The resolution is a function of focal spot shape, size, and central axis position and this property of lower resolution in the magnification mode may or may not be true for other manufacturer's mammography units.

Even though our measurements showed that the inherent resolution of the screen is slightly better than 20 lp/mm, the measured resolutions of the line-pair pattern in contact [magnification (M)=1.1] and magnification (M=1.8) geometries were 1–3 lp/mm worse with the screen-film than with the direct film detector. The reason can be explained in terms of the overall MTF's of the imaging systems. The overall MTF is the product of the MTFs of the individual components (e.g., the MTFs of the focal spot, film, and screen). The geometric magnification factors associated with both the contact and magnification techniques result in degradation of the MTF of the focal spot and improvement in the effective MTF of the screen. When the latter improvement is not great enough to compensate for the focal spot MTF degradation, the limiting resolution is reduced to a lower spatial frequency, as we observed.

When performing the resolution measurements with a screen-film detector, it is very important to allow enough time for the entrapped air between the film and screen to escape. The ACR recommends waiting 15 min in their protocol for screen-film contact verification, but does not include this recommendation in the protocol for the focal spot

TABLE III. Resolution as a function of kVp for (a) contact geometry using a 0.3 mm focal spot and (b) 1.8 times magnification geometry using a 0.1 mm focal spot (a plus sign implies bars very clearly discerned and limiting resolution is greater by about 0.5 lp/mm or more).

(a) Attenuator	None (air)			Lucite	
Detector	Direct film			Screen-film	
Use of grid	No			Yes	
X-ray tube potential	22 kVp	26 kVp	30 kVp	26 kVp	30 kVp
Limiting resolution with bars parallel to the anode–cathode axis	18 lp/mm	20 lp/mm	20 lp/mm	16 lp/mm	17 lp/mm
Limiting resolution with bars perpendicular to the anode–cathode axis (20 lp/mm segment within 1 cm from chest wall)	20+ lp/mm	20+ lp/mm	20+ lp/mm	18 lp/mm	18 lp/mm

(b) Attenuator	None (air)		
Detector	Direct film		
Use of grid	No		
X-ray tube potential	22 kVp	26 kVp	30 kVp
Limiting resolution with bars parallel to the anode–cathode axis	20+ lp/mm	20+ lp/mm	20 lp/mm
Limiting resolution with bars perpendicular to anode–cathode axis (20 lp/mm segment within 1 cm from chest wall)	16 lp/mm	15 lp/mm	14 lp/mm

evaluation. Our tests revealed that too short a waiting time can reduce resolution by as much as 3 lp/mm. We believe that the ACR should include a reminder concerning the 15 min waiting time in their "Precautions and Caveats" statements for any tests dealing with spatial resolution, in particular the high contrast resolution test and the phantom image quality test.

When the Lucite attenuator is placed in the beam, the resulting increase in x-ray scatter at the detector causes a reduction in measured spatial resolution of about 1 lp/mm relative to the no-attenuator situation. (Compare columns 2 and 3 of Tables I and II.) This trend is expected since the scatter reduces the imaged contrast of the line-pair pattern. It is more difficult to analyze the images produced with the Lucite attenuator because of the reduced contrast; however, the imaging situation is closer to that for patients.

When examining images of the line-pair pattern, care must be taken to read from low line pairs to high line pairs so that spurious resolution is avoided. This effect is the same as that observed in the star pattern focal spot evaluation test. Resolution is apparent up to a certain lp/mm, after which it is lost, and then it seems to return with phase reversal (the black and white bars are reversed) at even higher lp/mm. The limiting resolution is the line pair of the segment that precedes the first one that cannot be resolved. The patterns that are employed for this test must contain fairly fine lp/mm increments; otherwise, the true limiting resolution may not be detected.

The ACR protocol stipulates that the line-pair pattern be placed "within 1 cm of the chest wall edge of the image receptor." [1] These protocol directions are somewhat ambiguous for the case when the bars of the pattern are perpendicular to the anode–cathode axis, since one does not know which lp/mm segments of the pattern should be within the 1 cm distance. The effective focal spot size and the resultant spatial resolution varies rapidly along the anode–cathode direction. The distance between the lowest (5 lp/mm) and the highest (20 lp/mm) spatial resolution segments of our particular pattern was 1.8 cm. As seen in Table I, the results were about the same for contact geometry when the pattern

was oriented with either the 5 or 20 lp/mm segment closest to the chest wall. However, for magnification geometry (Table II) there was a 2 lp/mm difference. To ensure consistent and comparable results, we believe that the ACR should recommend a specific design for the line-pair pattern (including dimensions) and should specify the position of a particular segment of the pattern. For example, they could specify that the 20 lp/mm segment be placed 0.5 cm from the chest wall edge of the image receptor, with lower resolution segments directed toward the nipple position. The ACR should also provide a more detailed description of where to place the pattern when performing the test in magnification mode. It is not clear whether the pattern or the projected image of the pattern should be within 1 cm of the chest wall edge of the detector. We placed the pattern within 1 cm of the top chest wall edge of the magnification stand when we performed our tests.

The x-ray tube potential (Table III) had a noticeable influence on the focal spot performance. For contact geometry, [Table III(a)] the resolution improved as the kVp increased. This was especially apparent when the bars of the pattern were oriented parallel to the anode–cathode axis. It is an expected result since the effective focusing of the electron beam in the x-ray tube is known to improve as the kVp is increased. For the magnification geometry, however, the resolution degraded as the kVp increased. This seemingly aberrant result can be explained by the fact that focal spot size is both a function of kVp and mA—the size decreases as the kVp increases and increases as the mA increases. On the GE DMR mammography unit, the mA changes as the kVp is varied. There is greater mA at high kVp and lower mA at low kVp. This change is much greater for the small focal spot than for the large (e.g., in going from 25 to 30 kVp on the large focal spot, there is a 14% increase in mA; whereas, the corresponding increase in mA for the small focal spot is 45%). For the small focal spot case, the mA is more important in determining focal spot size and resolution than the kVp. Accordingly, the lowest mA at 22 kVp in our tests results in the best resolution; whereas, the highest mA at 30 kVp results in the poorest resolution.

V. CONCLUSION

The new line-pair method for evaluating focal spot performance is convenient and easy to perform.

As shown in Tables I–III, the results of the line-pair resolution test depend upon the setup employed. Of the three possible setups, we prefer the one using no attenuator and direct film, because it does not require a 15 min waiting time between loading the cassette and making the exposure, and it results in a truly quick measure of focal spot performance. If, instead, one is interested in measuring the resolution of the entire imaging chain in a cliniclike situation, one should use the Lucite attenuator with screen-film detector setup. The third alternative—use of no attenuator with screen-film is not recommended.

In many instances, we were able to clearly discern the 20 lp/mm segment of the test pattern and expected to resolve greater line pairs. A pattern that ranges from 9 to 25 lp/mm in 1 lp/mm increments might be useful for more accurately determining the limiting resolution of a mammography system. Of course use of such a pattern is not absolutely necessary, as 20 lp/mm resolution should be more than adequate in most imaging situations.

The previous edition of the ACR manual[5] included the description of a focal spot test using a star pattern test tool. Because the spokes in the star pattern essentially produce a continuous rather than discrete spatial frequency scale, this test may yield a more accurate assessment of focal spot size than the line-pair resolution test. Furthermore, the star pattern test is easy to perform, especially when a star pattern positioner/holder is provided by the manufacturer. We hope that the ACR will endorse both the star pattern test with the focal spot test stand[5] and the star pattern test with manufacturer provided positioner/holder as additional acceptable focal spot evaluation methods in the next mammography QC manual. Finally, if the positioner/holder method is endorsed, the ACR should provide manufacturers with guidelines for the proper position of the star pattern (e.g., the projected center should be 4 cm from the chest wall).

ACKNOWLEDGMENTS

The authors wish to thank Bill Drury of CIRS, Inc. for providing us with the prototype phantom that was used in our study. We also thank John Sandrik, Ph.D. of General Electric for enlightening discussions concerning focal spot size as a function of kVp and mA. This work was supported in part by Grant No. DAMD 17-94-J-4292 from the USAMRMC.

[a]Electronic mail: goodsitt@umich.edu

[1]*American College of Radiology Mammography Quality Control Manual: Medical Physicist's Section Revised Edition, 1994* (American College of Radiology, Reston, VA, 1994).

[2]E. L. Nickoloff, E. Donnelly, L. Eve, J. V. Atherton, and T. Asch, "Mammographic resolution: Influence of focal spot intensity distribution and geometry," Med. Phys. **17**, 436–447 (1990).

[3]G. T. Barnes, "Tube potential, focal spot, radiation output and HVL measurements on screen mammography units," in *Screen Film Mammography: Imaging Considerations and Medical Physics Responsibilities*, edited by G. T. Barnes and G. D. Frey (Medical Physics, Madison, WI, 1991), pp. 67–113.

[4]C. Kimme-Smith, L. W. Bassett, and R. H. Gold, "Focal spot size measurements with pinhole and slit for microfocus mammography units," Med. Phys. **15**, 289–303 (1988).

[5]*American College of Radiology Mammography Quality Control Medical Physicist's Manual* (American College of Radiology, Reston, VA, 1990).

Bob Liu, PhD • Mitchell Goodsitt, PhD • Heang-Ping Chan, PhD

Normalized Average Glandular Dose in Magnification Mammography[1]

PURPOSE: **To evaluate the normalized average glandular dose (the average glandular dose per unit entrance skin exposure) in magnification mammography.**

MATERIALS AND METHODS: **Photon transport in the breast was simulated by using Monte Carlo methods. A semielliptical cylinder containing glandular and adipose tissue was used to simulate the breast. Measured mammography spectra for a molybdenum target–molybdenum filter unit were utilized. The normalized average glandular dose was calculated as a function of half-value layer, tube voltage, breast thickness, and breast composition for typical magnification geometries.**

RESULTS: **The normalized average glandular dose in magnification mammography is 7%–25% lower than that with the contact (nonmagnification) technique because of the effects of partial irradiation, smaller field size, and greater percentage depth dose gradient at the reduced source-to-skin distance.**

CONCLUSION: **The normalized average glandular dose in magnification mammography is lower than that in contact mammography. The average glandular dose in magnification mammography, however, is still substantially greater due to the two to three times greater entrance skin exposure.**

Index terms: Breast radiography, radiation dose, 00.11 • Radiations, exposure to patients and personnel • Radiations, measurement

Radiology 1995; 197:27–32

MAGNIFICATION mammography has several advantages over conventional contact (nonmagnification) mammography. These include improved spatial resolution, increased contrast, and reduced effective noise (1,2). To our knowledge, however, the relative carcinogenic risk for this procedure has not been discussed in depth in the literature. It is well known that the glandular tissue in the breast is the most vulnerable to radiation and that the average glandular dose is directly related to the risk.

The average glandular dose D_g can be estimated with the equation $D_g = D_{gN} \cdot X_{ESE}$, where D_{gN} is the normalized average glandular dose (ie, average glandular tissue dose for 1 R entrance skin exposure) and X_{ESE} the free-in-air entrance skin exposure that can be easily measured. Methods for calculating D_{gN} for contact mammography are well established (3–5), and the published results are routinely used by medical physicists in their quality control tests of mammography equipment (6). For a given target-filter combination, D_{gN} for contact mammography is basically a function of tube voltage, half-value layer (HVL), breast thickness, and breast composition. The dependence of D_{gN} on source-to-skin distance (SSD) and breast area in contact mammography is negligible (3).

However, in magnification mammography, a shorter SSD (as short as 27 cm) and a smaller field size (as small as 81 cm^2 at the image plane) are often used. It is not clear whether the effects of SSD and field size are still minimal. In addition, only a part of the breast is exposed in magnification mammography (Fig 1). To our knowledge, the effect of this partial irradiation has not been investigated. Because tables of D_{gN} for the magnification technique do not exist, some physicists simply assume in their dose calculation that the D_{gN} to the irradiated volume in magnification mammography is the same as that in contact mammography (7,8).

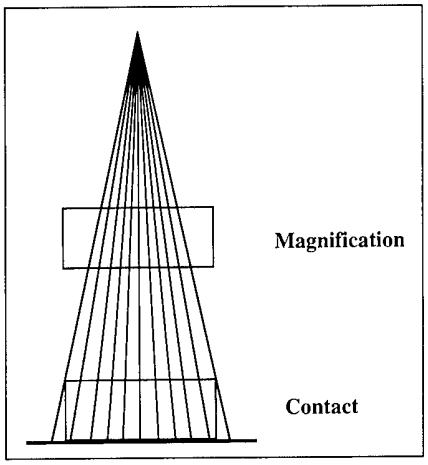

Figure 1. Irradiation geometry in mammography. The entire breast is exposed in contact mammography, and only part of the breast is exposed in magnification mammography.

In contact mammography, D_{gN} is defined as the total energy absorbed per unit entrance skin exposure by the glandular tissue in the breast divided by the total mass of glandular tissue. Because the entire breast is in the direct beam in this case, the D_{gN} is actually the total energy absorbed per unit entrance skin exposure by the glandular tissue in the direct beam divided by the total mass of glandular tissue in the direct beam. Similarly, we define D_{gN} in magnification mammography as the ratio of the total energy absorbed per entrance skin expo-

[1] From the Department of Radiology, University of Michigan, 1500 E Medical Center Dr, Ann Arbor, MI 48105. Received October 31, 1994; revision requested December 16; revision received May 1, 1995; accepted June 6. Supported in part by grant DAMD17-94-J-4292 from the U.S. Army Medical Research and Development Command and U.S. Public Health Service grant CA 48129. **Address reprint requests to** B.L.

Abbreviations: D_{gN} = normalized average glandular dose, HVL = half-value layer, SSD = source-to-skin distance.

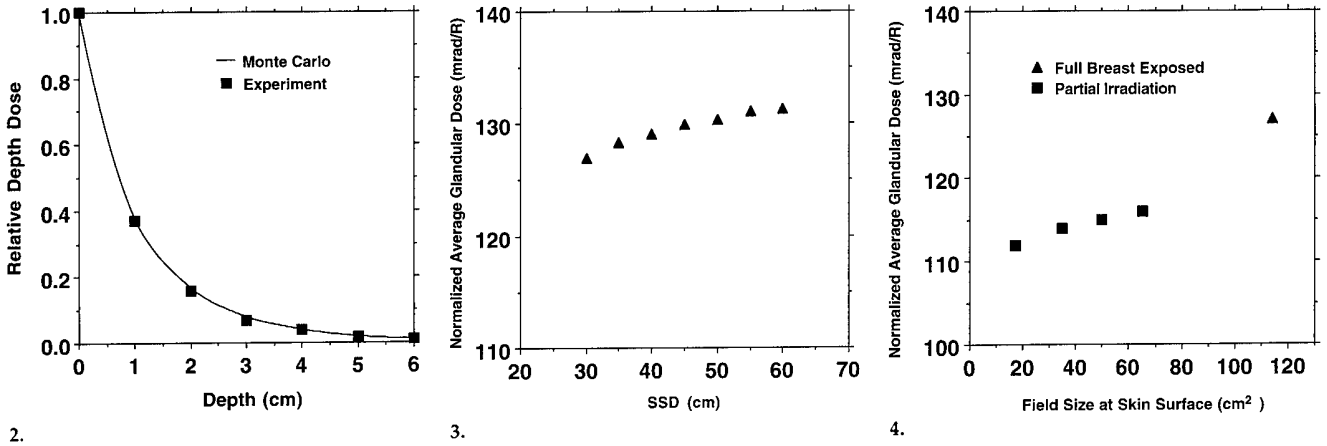

2. 3. 4.

Figures 2–4. **(2)** Comparison of relative depth dose in a BR-12 phantom simulating a breast thickness of 6 cm with experimental data from reference 15. Calculations were performed with an SSD of 45 cm, 28 kVp, and an HVL of 0.31 mm aluminum. **(3)** Dependence of D_{gN} on SSD in mammography. The entire breast was irradiated. The breast phantom thickness was 5 cm. Calculations were performed with 28 kVp and an HVL of 0.31 mm aluminum. **(4)** Dependence of D_{gN} on field size and the effect of partial irradiation in magnification mammography. For a 5-cm breast phantom, the typical field sizes at the skin surface are 17 cm^2 (9 × 9 cm at the image plane) for spot magnification and 66 cm^2 (14 × 22 cm at the image plane) for regular magnification. Calculations were performed with a source-to-image distance of 65 cm, an SSD of 30 cm, 28 kVp, and an HVL of 0.31 mm aluminum.

sure by the glandular tissue in the direct beam to the total mass of glandular tissue in the direct beam.

In this study, we investigated the effects of SSD, field size, and partial irradiation on D_{gN} in magnification mammography. We calculated D_{gN} as a function of tube voltage, HVL, breast thickness, and breast composition by using Monte Carlo simulation (9,10). Herein, we present several D_{gN} tables for typical geometries employed in magnification mammography and estimate the errors involved if the contact mammography tables are used for the magnification technique. We also discuss the factors that should be taken into account when the risk is estimated.

MATERIALS AND METHODS

Monte Carlo Simulation

A Monte Carlo code (MCNP4A) developed at Los Alamos National Laboratory, Los Alamos, New Mexico (11), was used to simulate the transport of x-ray photons in the breast. Command files were designed so that photoelectric effect, Compton scattering, coherent (Thomson) scattering, fluorescent photons after photoelectric absorption, and electron binding effects were taken into account. The electron binding effect was included by using the appropriate tissue atomic form factors that modify the Compton and Thomson scattering cross sections. A stop criteria was set to ensure that the relative error of the calculated D_{gN} was less than 0.5%.

For a given breast thickness and composition, the normalized average dose to the irradiated breast volume D_{gN} was first calculated for monoenergetic incident photons. This was accomplished by dividing the total energy deposited in the irradiated breast volume (which is the entire breast for the contact technique and part of the breast for the magnification technique as shown in Fig 1) by the total mass of the irradiated breast volume. The mass of the skin layer, the energy deposited in the skin layer, and (in the case of the magnification technique) the energy deposited in the breast tissue outside the primary beam path were excluded. The D_{gN} at a given energy E_i was obtained by multiplying D_{gN} by a conversion factor that is the ratio of the x-ray mass energy absorption coefficient $\mu_{en}(E_i)/\rho$ of the glandular tissue to that of the breast tissue, as follows:

$$D_{gN}(i) = D_{iN}(i) \times \frac{\left[\frac{\mu_{en}(E_i)}{\rho}\right]_g}{\omega_g\left[\frac{\mu_{en}(E_i)}{\rho}\right]_g + \omega_a\left[\frac{\mu_{en}(E_i)}{\rho}\right]_a},$$

where g and a denote glandular tissue and adipose tissue, respectively, and ω_g and ω_a are their fractions by weight. For a polyenergetic x-ray spectrum, D_{gN} was calculated as a sum of the D_{gN}s for monoenergetic incident photons calculated at 1-keV energy increments weighted by the spectral intensities.

Mammography Spectra

We employed the measured x-ray spectra from a TransContinental (formerly Transworld) mammography system (Charlotte, NC) (12,13). This system had an x-ray tube (RAD-71 insert; Eureka, Arlington Hts, Ill) with a molybdenum anode. The tube was powered by a high-frequency generator. The anode angle was 16°. When the spectra were measured, there was no filtration beyond that provided by the 0.8-mm beryllium window of the x-ray tube. For our Monte Carlo simulation, we attenuated the spectra with a 30-μm molybdenum filter. For a given tube voltage, spectra with different HVLs were obtained by varying the thickness of a simulated compression paddle made of 1- to 5-mm-thick Lexan (GE Plastics, Pittsfield, Mass) (3).

Breast Phantom

Following the work of Rosenstein et al (5), we simulated the breast by using a semielliptical cylinder consisting of a uniform mixture of glandular and adipose tissue contained within a 0.4-cm-thick skin layer. The cross section of the breast was a half ellipse with a long axis of 18 cm and a short axis of 16 cm. The area of the cross section was 113.1 cm^2 (9 cm × 8 cm × π/2). The simulated breast thicknesses were varied between 3 and 8 cm. The glandular and adipose tissue compositions were taken from the measured results of Hammerstein et al (14). As recommended by Rosenstein et al (5), the skin layer was assumed to have the same x-ray absorption properties as the glandular tissue. However, the energy absorbed in the skin and the mass of the skin are not included in the calculation of D_{gN} because the carcinogenic risk in the skin is considered minimal. Four breast compositions were considered. The contents of glandular tissue ranged from 25% to 100%.

Geometry

For dedicated mammography systems, source-to-image distances range from 50 to 75 cm, with 60–65 cm being the most common. The source-to–breast stand distances for magnification usually range from 35 to 45 cm. The magnification fac-

Table 1

D_{gN} (millirad per roentgen) in Magnification Mammography for 25% Glandular Tissue, 75% Adipose Tissue Breast (Field Size at the Image Plane = 14 × 22 cm)

X-ray Tube Voltage (kVp)	HVL (mm Al)	Breast Thickness (cm)					
		3	4	5	6	7	8
24	0.27	189	141	109	87	70	59
	0.28	195	146	113	90	73	61
	0.29	201	151	117	94	76	63
	0.30	207	156	121	97	79	65
	0.31	213	160	125	100	81	67
	0.32	219	165	129	103	84	69
	0.33	225	170	133	106	87	71
	0.34	231	175	136	109	89	73
	0.35	237	180	140	112	91	75
	0.36	243	184	143	115	93	77
26	0.29	205	154	120	96	78	65
	0.30	211	159	124	99	81	67
	0.31	216	164	128	102	83	69
	0.32	223	169	132	105	86	71
	0.33	229	173	135	108	88	73
	0.34	234	178	139	111	91	75
	0.35	240	182	143	114	93	77
	0.36	245	187	146	117	96	79
	0.37	251	192	150	120	99	81
	0.38	256	197	153	123	102	83
28	0.31	220	167	131	105	86	71
	0.32	225	171	134	107	88	73
	0.33	231	176	138	110	90	75
	0.34	236	180	141	113	93	77
	0.35	242	184	145	116	95	79
	0.36	247	189	148	119	97	81
	0.37	253	193	152	122	100	83
	0.38	258	198	156	125	102	85
	0.39	263	203	160	128	105	87
	0.40	268	207	164	131	107	89
30	0.33	233	178	140	112	92	76
	0.34	238	182	143	115	94	78
	0.35	243	186	146	118	97	80
	0.36	249	191	150	121	99	82
	0.37	254	195	153	124	101	84
	0.38	259	199	157	126	104	86
	0.39	265	203	161	129	106	88
	0.40	271	208	164	133	109	91
	0.41	276	213	167	136	112	93
	0.42	281	218	170	139	115	95

Note.—Doses are in conventional, not SI, units. Conversion factor: 1 mrad/R = 38.8 mGy/(C/kg).

Table 2

D_{gN} (millirad per roentgen) in Magnification Mammography for 50% Glandular Tissue, 50% Adipose Tissue Breast (Field Size at the Image Plane = 14 × 22 cm)

X-ray Tube Voltage (kVp)	HVL (mm Al)	Breast Thickness (cm)					
		3	4	5	6	7	8
24	0.27	172	126	97	76	62	51
	0.28	177	130	100	79	64	53
	0.29	183	135	104	81	66	54
	0.30	188	139	107	84	68	56
	0.31	193	143	110	87	71	58
	0.32	199	147	113	90	73	60
	0.33	205	152	117	92	75	62
	0.34	210	156	120	95	77	64
	0.35	216	161	124	98	79	66
	0.36	221	165	127	100	81	68
26	0.29	186	138	106	84	68	56
	0.30	192	142	109	87	70	58
	0.31	197	146	113	89	72	60
	0.32	203	151	116	92	75	62
	0.33	208	155	119	95	77	64
	0.34	213	159	123	97	79	65
	0.35	219	163	126	100	81	67
	0.36	224	167	129	103	83	69
	0.37	229	171	132	106	85	71
	0.38	234	175	135	109	87	73
28	0.31	201	150	116	92	75	62
	0.32	205	153	118	94	76	63
	0.33	211	157	122	97	79	65
	0.34	216	161	125	99	81	67
	0.35	221	165	128	102	83	69
	0.36	226	169	131	104	85	70
	0.37	232	174	135	107	87	72
	0.38	237	178	138	110	89	74
	0.39	242	182	141	113	91	76
	0.40	247	186	144	116	93	78
30	0.33	213	160	124	99	80	66
	0.34	218	163	127	101	82	68
	0.35	223	167	130	103	84	70
	0.36	228	172	133	106	87	72
	0.37	233	175	136	109	88	73
	0.38	238	179	139	111	91	75
	0.39	243	183	142	114	93	77
	0.40	248	187	146	117	95	79
	0.41	253	191	149	120	97	81
	0.42	258	195	152	123	99	83

Note.—Doses are in conventional, not SI, units. Conversion factor: 1 mrad/R = 38.8 mGy/(C/kg).

Table 3

D_{gN} (millirad per roentgen) in Magnification Mammography for 75% Glandular Tissue, 25% Adipose Tissue Breast (Field Size at the Image Plane = 14 × 22 cm)

X-ray Tube Voltage (kVp)	HVP (mm Al)	Breast Thickness (cm)					
		3	4	5	6	7	8
24	0.27	156	112	85	66	53	44
	0.28	161	116	88	69	56	46
	0.29	166	120	91	71	58	47
	0.30	171	124	94	74	60	49
	0.31	177	128	97	77	62	50
	0.32	182	132	100	79	64	52
	0.33	187	136	103	81	66	54
	0.34	192	140	106	84	68	56
	0.35	197	144	109	87	70	57
	0.36	202	148	112	90	72	59
26	0.29	170	123	94	74	60	49
	0.30	175	127	97	76	62	51
	0.31	180	131	100	79	64	52
	0.32	185	135	103	81	66	54
	0.33	190	139	106	84	68	56
	0.34	195	143	109	86	69	57
	0.35	200	146	112	88	71	59
	0.36	205	150	115	91	73	60
	0.37	210	154	118	94	75	61
	0.38	214	158	121	97	77	63
28	0.31	183	134	103	81	66	54
	0.32	188	138	105	83	67	55
	0.33	193	141	108	85	69	57
	0.34	197	145	111	88	71	58
	0.35	202	149	114	90	73	60
	0.36	207	152	117	92	75	62
	0.37	212	156	120	95	77	63
	0.38	217	160	123	97	79	65
	0.39	222	164	126	99	81	67
	0.40	227	168	129	102	83	69
30	0.33	195	144	110	87	71	58
	0.34	199	147	113	89	72	60
	0.35	204	150	116	91	74	61
	0.36	209	154	119	94	76	63
	0.37	213	158	121	96	78	64
	0.38	218	161	124	98	80	66
	0.39	223	165	127	101	82	68
	0.40	228	169	130	103	84	69
	0.41	233	173	133	105	86	71
	0.42	238	177	136	107	88	73

Note.—Doses are in conventional, not SI, units. Conversion factor: 1 mrad/R = 38.8 mGy/(C/kg).

Table 4

D_{gN} (millirad per roentgen) in Magnification Mammography for 100% Glandular Tissue Breast (Field Size at the Image Plane = 14 × 22 cm)

X-ray Tube Voltage (kVp)	HVL (mm Al)	Breast Thickness (cm)					
		3	4	5	6	7	8
24	0.27	141	100	75	59	47	39
	0.28	146	104	78	61	49	40
	0.29	151	108	81	63	51	41
	0.30	156	112	84	66	53	43
	0.31	161	115	87	68	54	45
	0.32	166	119	89	70	56	46
	0.33	171	123	92	72	58	47
	0.34	175	126	95	74	60	49
	0.35	180	129	98	76	62	50
	0.36	185	132	101	78	64	51
26	0.29	155	111	84	66	53	43
	0.30	160	115	86	68	54	45
	0.31	164	118	89	70	56	46
	0.32	169	122	92	72	58	48
	0.33	174	125	95	74	60	49
	0.34	178	128	97	76	61	50
	0.35	183	132	100	78	63	52
	0.36	188	135	102	80	65	53
	0.37	193	138	105	82	67	54
	0.38	198	141	107	84	69	55
28	0.31	168	121	92	72	58	48
	0.32	172	124	94	74	60	49
	0.33	177	127	97	76	61	50
	0.34	181	131	99	78	63	52
	0.35	185	134	102	80	65	53
	0.36	190	137	104	82	66	55
	0.37	195	141	107	84	68	56
	0.38	199	144	110	86	70	57
	0.39	204	147	113	88	72	58
	0.40	209	150	116	90	74	59
30	0.33	179	130	99	78	63	52
	0.34	183	133	101	79	64	53
	0.35	187	136	103	81	66	54
	0.36	192	140	106	84	68	56
	0.37	196	143	109	86	69	57
	0.38	200	146	111	88	71	58
	0.39	205	149	114	90	73	60
	0.40	210	153	117	92	75	61
	0.41	215	156	119	94	77	63
	0.42	220	159	122	96	79	64

Note.—Doses are in conventional, not SI, units. Conversion factor: 1 mrad/R = 38.8 mGy/(C/kg).

Table 5
D_{gN} (millirad per roentgen) in Spot Magnification Mammography for 50% Glandular Tissue, 50% Adipose Tissue Breast (Field Size at the Image Plane = 9 × 9 cm)

X-ray Tube Voltage (kVp)	HVL (mm Al)	Breast Thickness (cm)					
		3	4	5	6	7	8
24	0.27	166	121	93	74	59	50
	0.28	172	126	97	77	62	52
	0.29	178	131	100	79	65	53
	0.30	183	135	104	82	67	55
	0.31	188	189	107	85	69	57
	0.32	193	143	110	87	71	59
	0.33	198	147	113	90	73	60
	0.34	204	151	116	92	75	62
	0.35	209	155	119	94	77	64
	0.36	215	159	122	96	79	65
26	0.29	181	134	103	82	66	55
	0.30	186	138	106	84	69	57
	0.31	191	142	109	87	71	58
	0.32	196	146	112	89	73	60
	0.33	202	150	116	92	75	62
	0.34	206	153	119	94	77	64
	0.35	212	157	122	97	79	65
	0.36	216	161	125	99	81	67
	0.37	221	165	128	101	83	68
	0.38	226	169	131	103	85	70
28	0.31	194	145	112	89	72	60
	0.32	199	148	114	91	74	62
	0.33	204	152	117	94	76	63
	0.34	208	155	120	96	78	65
	0.35	213	159	123	98	80	67
	0.36	218	163	126	101	82	68
	0.37	223	167	130	103	84	70
	0.38	228	171	133	106	86	71
	0.39	233	175	136	109	88	73
	0.40	238	179	139	112	90	74
30	0.33	206	154	119	95	78	64
	0.34	210	157	122	97	79	66
	0.35	215	161	125	100	81	67
	0.36	220	165	128	102	83	69
	0.37	224	168	131	104	85	71
	0.38	229	172	134	107	87	72
	0.39	234	176	137	109	89	74
	0.40	239	180	140	112	91	76
	0.41	244	184	143	115	93	77
	0.42	249	188	146	118	95	79

Note.—Doses are in conventional, not SI, units. Conversion factor: 1 mrad/R = 38.8 mGy/(C/kg).

Table 6
Comparison of D_{gN} (millirad per roentgen) in Contact and Magnification Mammography for 50% Glandular Tissue, 50% Adipose Tissue Breast

Breast Thickness (cm)	D_{gN}*		Magnification-Contact Ratio
	Magnification Mammography	Contact Mammography	
3	201	216	0.93
4	150	166	0.90
5	116	133	0.87
6	92	109	0.84
7	75	92	0.81
8	62	79	0.78

* Doses are in conventional, not SI, units. Conversion factor: 1 mrad/R = 38.8 mGy/(C/kg). The field size at the image plane for magnification mammography was 14 × 22 cm.

tors range from 1.5 to 2.1. The typical field size at the image plane is 81 cm^2 (9 × 9 cm) for spot magnification and 308 cm^2 (14 × 22 cm) for regular magnification. We calculated the D_{gN} for these typical field sizes. Because the breast is midway between the focal spot and the image plane, the field sizes at the breast skin surface are about 25% of those at the image plane. In this study, we used a source-to-image distance of 65 cm and a source-to–breast stand distance of 35 cm.

Validation of the Calculation Procedure

To verify our computation procedure, we calculated the depth dose by Monte Carlo simulation in a BR-12 phantom (RMI, Middleton, Wis) for a 28-kVp beam with an HVL of 0.31 mm aluminum and compared the results to experimental data (15). We also calculated the D_{gN} for a phantom simulating a breast thickness of 5 cm at 26, 28, 30, and 34 kVp with various HVLs for the contact technique and compared the results with those from the study by Wu et al (3).

RESULTS

The relative depth dose in a 6-cm BR-12 phantom for a 28-kVp beam with an HVL of 0.31 mm aluminum is shown in Figure 2. The Monte Carlo predictions are in good agreement with the experimental data.

Our D_{gN}s for the contact technique agree with those of Wu et al (3) to within 2%. The small differences in D_{gN} can be attributed to differences in x-ray spectra. When the same spectra are used, the differences between our results and those of Wu et al are less than 0.6%.

The dependence of the D_{gN} on SSD when the entire breast is irradiated is shown in Figure 3. The typical SSD for contact mammography is about 60 cm and that for magnification mammography is about 30 cm. For a 5-cm-thick breast and a 28-kVp beam with a HVL of 0.31 mm aluminum, changing the SSD from 60 to 30 cm decreases the D_{gN} by 3.4%.

The effect of field size is shown in Figure 4 for a 5-cm breast and a 28-kVp beam with an HVL of 0.31 mm aluminum. If the breast is partially irradiated, changing the field size at the skin surface from 65.6 cm^2 (regular magnification) to 17 cm^2 (spot magnification) decreases the D_{gN} by 3.6%. This decrease is caused by decreased scattered radiation.

The effect of partial irradiation is also shown in Figure 4. When the entire breast is irradiated with a field size of 113 cm^2 at the skin surface, the D_{gN} is 127 mrad/R. If we reduce the field size at the skin surface to 66 cm^2 so that only part of the breast is exposed, the D_{gN} becomes 10% lower. This decrease cannot be attributed entirely to the reduced scatter radiation because it only accounts for, at most, a 4% reduction. The D_{gN} as a function of tube voltage, HVL, breast thickness, and breast composition in magnification mammography was calculated for typical regular (field size at the image plane, 14 × 22 cm) and spot (field size at the image plane, 9 × 9 cm) magnification geometries.

The results are listed in Tables 1–5. For a given breast thickness and composition, we found that the ratio of the D_{gN} for magnification mammography to that for contact mammography is almost independent of tube voltage and HVL. Table 6 shows this ratio for different breast thicknesses for breasts of 50% glandular and 50% adipose tissue. The ratio varies from 0.78 to 0.93.

DISCUSSION

The D_{gN} in magnification mammography is about 7%–25% lower than that in contact mammography. Three factors contribute to this reduction: the smaller SSD, the smaller field size, and partial irradiation.

The decrease in SSD usually results in a small (typically $\approx 3\%$) decrease in D_{gN} because the relative depth dose decreases more rapidly as a function of depth at short SSDs (16). This is the effect of the inverse-square law.

In general, the D_{gN} decreases as the field size decreases because of the reduced scattered radiation for the smaller irradiated tissue volume. In contact mammography, the field sizes at the skin surface are relatively large and the dependence of D_{gN} on field size at the skin surface (breast area in this case) is negligible (3). In magnification mammography, the field sizes at the breast skin surface can be very small and can vary over a wide range. The dependence of D_{gN} on field size may need to be taken into account when average glandular dose is estimated. Most magnification procedures can be classified into two categories: spot magnification and regular magnification. Spot magnification is used to examine a very small region in the breast. The typical field size at the image plane for this procedure is about 81 cm^2 (9 × 9 cm). For regular magnification, a larger portion of the breast is irradiated. The typical field size at the image plane is about 308 cm^2 (14 × 22 cm). The difference in D_{gN} between the two geometries ranged from 2% to 5%, depending on breast thickness and beam quality. The approximate D_{gN} for other field sizes can be obtained with interpolation or extrapolation.

Partial irradiation plays an important role in D_{gN} reduction in magnification mammography. This is illustrated in Figure 1. Notice that in contact mammography, a part of the x-ray beam traverses only a small thickness near the peripheral region. As indicated in Figure 2, the percentage depth dose in this peripheral region (small depth) is very high relative to that in deeper regions in the breast. Because this particular high-dose region is not in the direct beam in magnification mammography, the D_{gN} is lower. Depending on the breast thickness, the D_{gN} in magnification mammography is about 4%–16% lower than that for contact mammography as a result of this effect. One may wonder if this is the result of our breast model. We performed dose calculation for a breast phantom with an elliptical cross section (instead of the rectangular cross section shown in Fig 1) in the peripheral region and observed the same result.

It is clear that use of the tables for contact mammography to calculate the average glandular dose in magnification mammography will result in overestimations up to 25%.

When assessing the actual glandular dose in magnification mammography, several factors must be considered. The SSD for the magnification technique is about 30 cm, whereas it is about 60 cm for the contact technique. Thus, milliroentgen per milliampere second at the breast skin surface for the magnification technique is about four times that for the contact technique. However, there is an air gap between the breast and the screen-film cassette, which reduces the detection of scattered x rays. Consequently, a scatter-rejection grid is no longer needed in magnification mammography in most cases. Grids absorb both primary and scattered x rays, and elimination of the grid results in a reduction in the required milliampere second by a factor of about two. Use of a reduced source-to-object distance without using a grid for the magnification technique results in a twofold increase in entrance exposure. Experimental measurements indicate that the entrance skin exposure for the magnification technique is about 1.8–3.2 times that for the contact technique. Because D_{gN} in magnification mammography is 75%–93% of that with the contact technique, the average glandular dose in magnification mammography ($D_{gN} \cdot X_{ese}$) performed without a grid is about 30%–200% greater for the same breast thickness and beam quality. The average glandular dose in magnification mammography will be even higher if the grid is not removed.

Smaller compression paddles are frequently employed in magnification mammography to better isolate the tissues of interest. Under such circumstance, the compressed breast thickness is typically 1–2 cm less than the thickness of the same breast for the contact technique. This difference must be accounted for in the dose calculation (8).

It must be pointed out that although it is appropriate to use the average glandular dose to compare doses delivered to an average breast with different radiographic techniques, it is the total energy absorbed by the glandular tissue that determines the risk (14). For the same average glandular dose, breast thickness, and composition, the larger the breast area in the x-ray beam, the higher the risk. In principle, the dose to the glandular tissue outside the irradiated volume due to the scattered x-ray photons adds to the risk. We have calculated the average glandular dose in that region and found that it is about two orders of magnitude lower than that in the irradiated region. Therefore, for all practical purposes, the risk contribution from this scattered radiation can be ignored. It may also be noted that inclusion of the energy absorbed in the glandular tissue and the mass of the glandular tissue outside the direct beam in the calculation of average glandular dose for a partially irradiated breast will unrealistically underestimate the dose. ■

Acknowledgments: We are grateful to Robert J. Jennings, PhD, and Thomas Fewell, MS, of the Center for Devices and Radiological Health for providing the mammography x-ray spectra for this work. Bob Liu, PhD, thanks X. Z. Wu, PhD, for interesting discussion and for providing several of his mammography spectra for our comparison study. We thank Pamela Boyd, RTRM, for providing information on typical field sizes for magnification mammography.

References

1. Doi K. Advantages of magnification radiology. In: Logan WW, ed. Breast carcinoma. New York, NY: Wiley, 1977; 83–92.
2. Sickles EA. Magnification mammography. In: Logan WW, ed. Breast carcinoma. New York, NY: Wiley, 1977; 177–183.
3. Wu X, Barnes GT, Tucker DM. Spectral dependence of glandular tissue dose in screen-film mammography. Radiology 1991; 179:143–148.
4. Andersen LW, Rosenstein M. Computer program for absorbed dose to the breast in mammography. HHS (FDA) Publication no. 85–8243. Washington, DC: U.S. Government Printing Office, 1985.
5. Rosenstein M, Andersen LW, Warner G. Handbook of glandular tissue doses in mammography. HHS (FDA) Publication no. 85–8239. Washington, DC: U.S. Government Printing Office, 1985.
6. American College of Radiology. Mammography quality control: medical physicist's manual. Reston, Va: American College of Radiology, 1990.
7. Barnes GT, Frey GD. Mammography acceptance testing and quality control: documentation and reports. In: Barnes GT, Frey GD, eds. Screen-film mammography: Proceedings of SEAAPM Spring Symposium. Madison, Wis: Medical Physics Publishing, 1991; 219–220.
8. Kimme-Smith C, Bassett LW, Gold RH. Workbook for quality mammography. Baltimore, Md: Williams & Wilkins, 1992; 161–177.
9. Morin RL. Monte Carlo simulation in the radiological sciences. Boca Raton, Fla: CRC, 1988.
10. Chan HP, Doi K. The validity of Monte Carlo simulation in studies of scattered radiation in diagnostic radiology. Phys Med Biol 1983; 28: 109–129.
11. Briesmeister J. MCNP 4A: Monte Carlo N-particle transport code system. Los Alamos, NM: Los Alamos National Laboratory, 1993.
12. Jennings RJ, Quinn PW, Gagne RM, Fewell TR. Evaluation of x-ray sources for mammography. Proc SPIE 1993; 1896:259–268.
13. Quinn PW, Fewell TR, Jennings RJ. Measured x-ray spectra from current mammography systems (abstr). Med Phys 1994; 21:918.
14. Hammerstein GR, Miller DW, White DR, et al. Absorbed radiation dose in mammography. Radiology 1979; 130:485–491.
15. National Council on Radiation Protection and Measurements. Mammography: a user's guide. NCRP Report no. 85. Bethesda, Md: National Council on Radiation Protection and Measurements, 1986; 40–48.
16. Khan FM. The physics of radiation therapy. Baltimore, Md: Williams & Wilkins, 1984; 168–169.